# STRUCTURAL DEFECTS AND PROPERTIES OF MULTICOMPONENT MATERIALS

By

AIKATERINI BELLOU

A dissertation submitted in partial fulfillment of the requirements for the degree of

DOCTOR OF PHILOSOPHY

WASHINGTON STATE UNIVERSITY
College of Engineering and Architecture

DECEMBER 2009

To the Faculty of Washington State University

The members of the Committee appointed to examine the dissertation of AIKATERINI BELLOU find it satisfactory and recommend that it be accepted.

_____

David F. Bahr, Ph. D., Chair

_____

David P. Field, Ph. D.

_____

M. Grant Norton, Ph. D.

# ACKNOWLEDGEMENT

I would like to thank my advisor Dr David Bahr for his support and guidance. I appreciate his help and encouragement. I would also like to thank Dr David Field and Dr M. Grant Norton for serving in my committee and for their useful remarks. I would like to thank Dr. Louis Scudiero for his help with the X-ray Photoelectron Spectroscopy and Scotty Cornelius and Dr. Nick Foit for their help with X-ray diffraction and Wavelength Dispersive Spectroscopy.

I would also like to thank all the graduate students and staff members with whom I have worked over the years. My thanks go especially to Nicole Overman for her help with the bulge tester. I would also like to thank Joshah Jennings for his help in the clean room. I am also grateful to Bob Ames, Jan Danforth and Gayle Landeen for their help in all the administrative issues.

Finally my biggest thanks go to my husband Yanni whose understanding and support helped me through this process. I could not have done this without him.

# STRUCTURAL DEFECTS AND PROPERTIES OF MULTICOMPONENT MATERIALS

## Abstract

by Aikaterini Bellou, Ph.D.
Washington State University
December 2009

Chair: David F. Bahr

The relationship between the structure and properties of materials determine the behavior and performance of devices ranging from microelectromechanical systems (MEMS) to solid state lasers. This thesis focuses on two classes of materials used in high performance applications; metallic multilayer films and materials for optical applications. In the first case Mo/Pt multilayers are investigated as an alternative to Pt thin film electrodes for piezoelectric MEMS, whose strength is a limiting factor in improving the performance of the device. In the second case ceramic YAG, a common lasing medium for solid state lasers whose optical properties determine the beam quality, is investigated. In both cases material properties, mechanical in the first case and optical in the second, depend on microstructure hence improving device performance involves a better understanding of this relationship.

Mo/Pt multilayers with layer thicknesses ranging from 20 to 100 nm were sputtered. The mechanical properties of the nanocomposites were evaluated using both

nanoindentation and bulge testing. It was shown that the hardness of the multilayers increased as the layer thickness decreased with the behavior of the films deviating from a Hall Petch type of dependency for the smaller layer thicknesses used in this study. Aging of the films in air further improved their hardness indicating an additional strengthening mechanism. X-ray photoelectron spectroscopy revealed the presence of oxides in the aged samples pointing to precipitate hardening as the reason for the additional strengthening of the films. MEMS processing involves high temperatures in oxidizing environments hence the thermal stability of the nanolayers was also investigated. It was shown that structures with thicker layers maintained a substantial fraction of their strength and integrity.

Ceramic YAG is produced with the use of silica as a sintering aid. Improving the optical properties of ceramic YAG involves elimination of the scattering sources in the final products. Investigation of precipitate formation as a function of stoichiometry and processing conditions, using primarily Scanning Electron Microscopy and X-ray Dispersive Spectroscopy, showed that staying on stoichiometry and reducing the amount of silica in the sintering process will effectively decrease or even eliminate the presence of precipitates.

# TABLE OF CONTENTS

# TABLE OF FIGURES

# LIST OF TABLES

## Dedication

This dissertation is dedicated to my parents Maria and Dimitri

# Chapter One: Introduction

## 1.1 Background

Materials whose dimensions range from the nano to the macro scale are used in a number of applications. The common factor in all cases is that the properties of the material will affect the overall behavior and performance of the corresponding device. Since properties and structure are closely related, a better understanding of this relationship is necessary in order to improve materials used in technological applications and solve problems that may arise.

Thin films are used in a wide range of applications which include microsensors, actuators, flexible electronics, fuel cells and solar technology. The use of multilayered thin films where the thickness of the individual layers can be in the nanometer range offers the possibility of tailoring the properties of the composite. This can be done by a number of ways such as choosing the individual constituents of the composite, which will subsequently determine the structure of the interfaces, or vary the thickness of the individual layers. Hence a better understanding of the relationship between structure and properties is necessary in order to develop nanocomposites which will improve the performance of the different devices. In this work the mechanical properties of Mo/Pt multilayered films, which could be used as the bottom electrode in MEMS devices, were studied. A correlation between the observed mechanical behavior and changes in microstructure, which involve different layer thicknesses or phase changes upon annealing, was possible by combining the results of different characterization techniques.

$Y_3Al_5O_{12}$ ceramics have properties which make them attractive as the active medium in high power lasers [1]. However, the quality of the laser beam is greatly impacted by the presence of precipitates and second phases along the grain boundaries, which act as scattering centers. Study of the microstructure using different characterization techniques helps to identify these problems and suggest ways to reduce or even eliminate them.

In the following sections some of the characterization techniques used in the study of the different materials presented here will be briefly discussed.

## 1.2 Mechanical testing

### 1.2.1 Nanoindentation

Nanoindentation is one of the techniques commonly used to measure mechanical properties of thin films and multilayered structures. Tensile testing has also being used for mechanical testing of multilayered structures [2-5]. Nanoindentation is easier than tensile testing where the validity of strain measurements and the effects of flaws than were present or introduced during specimen preparation become sources of concern [3, 5]. In the case of nanoindentation possible sources of errors are related to the correct determination of the contact area and the effect of surface roughness [6]; however these errors can be more easily controlled or even eliminated. Mechanical testing using nanoindentation can be done in two different modes; quasistatic and continuous stiffness measurements. In both cases a sharp tip is used to probe the material.

In the case of quasistatic indentation the displacement $h$ relative to the undeformed surface as a function of the applied load $P$ is monitored. A typical load displacement curve is shown in Figure 1.1. The curve includes both a loading and an unloading part. The elastic properties of the sample are determined from the unloading portion of the curve which is considered purely elastic in contrast to the loading portion which describes both elastic and plastic behavior [6]. The stiffness $S$ ($dP/dh$) found from the unloading portion of the curve can be used to calculate the elastic modulus of the sample according to the following equation:

$$S = 2\beta\sqrt{\frac{A_c}{\pi}}E_r \tag{1.1}$$

where $\beta$ is a parameter that depends on the geometry of the indenter, $A_c$ is the contact area and $E_r$ is the reduced elastic modulus of the contact, which takes into account the elastic deformation of both the sample and the indenter. The elastic modulus of the sample is then found by:

$$\frac{1}{E_r} = \frac{1-\nu^2}{E} + \frac{1-\nu_i^2}{E_i} \tag{1.2}$$

where $E$, $\nu$ are the elastic modulus and Poisson ratio of the sample and $E_i$, $\nu_i$ are the corresponding parameters for the indenter.

The hardness $H$ of the sample can be found using the maximum load and area of contact $A_c$ according to the equation:

$$H = \frac{P_{max}}{A_c} \tag{1.3}$$

The calculation of both the elastic modulus and the hardness of the sample involve the indenter's area function. The area function is determined by indenting a standard material of known elastic modulus at different contact depths and then fitting the experimental data using an equation of the form:

$$A = C_0 h^2 + C_1 h + C_2 h^{1/2} + .... + C_8 h^{1/128} \tag{1.4}$$

This way the area function of the indenter as a function of contact depth is found and can be used to measure the mechanical properties of the sample.

When the continuous stiffness mode is used, measurements are recorded during the loading portion of the indentation load-displacement curve. In this case a harmonic force of known frequency and amplitude is superimposed to the applied load that continually increases. In Figure 1.2 a schematic of the loading cycle is presented which shows the superposition of the AC load on the DC load. Using a lock-in amplifier the displacement response to this harmonic force and the phase difference between the two signals as a function of contact depth is recorded. The contact stiffness $S$ of the material can then be calculated using the following equation:

$$\left|\frac{P_{OS}}{h(\omega)}\right| = \sqrt{\left\{(S^{-1} + K_f^{-1})^{-1} + K_S - m\omega^2\right\}^2 + \omega^2 C^2} \tag{1.5}$$

where $P_{os}$ is the force amplitude, $h(\omega)$ is the resulting displacement amplitude, $\omega$ is the frequency of the oscillation, $m$ is the mass of the indenter, $K_s$ is the spring constant, $K_f$ is the stiffness of the indenter frame and C is the damping coefficient of the sensor [7]. An air indent is used to determine the parameters $m$, $K_s$, and $C$ prior to indenting the sample. Once the contact stiffness is calculated the elastic modulus of the sample at all the different

contact depths can be found using (1.1). The hardness of the sample can be determined using equation (1.3) where $P_{max}$ is the DC load at each contact depth and $A_c$ is the corresponding contact area (1.4) [6-8].

The flow stress of the films can be estimated from hardness measurements as *H/2.7* where *H* is the hardness measured using nanoindentation [9]. The flow stress determined from hardness measurements doesn't correspond to the yield point but rather to a representative strain $\varepsilon_T$ that depends on the geometry of the indenter tip and is described by [10,11]:

$$\varepsilon_T = 0.2 \tan\beta = 0.2 \cot\theta \qquad (1.6)$$

where $\beta$ is the attack angle of the indenter [10] and $\theta$ is the included angle for conical indenters. For a Berkovich tip $\beta$ is equal to $19.7^o$ [12], giving a representative strain of ~7% whereas for a cube corner tip the same angle is equal to $47.7^o$ [12] corresponding to a strain of ~22 %. Therefore flow stress estimates describe both the yielding of the films and their strain hardening behavior and this should be taken into consideration when analyzing these estimates. For materials that strain harden the use of different indenter tips, which correspond to different strains, offers a way of studying their strain hardening behavior.

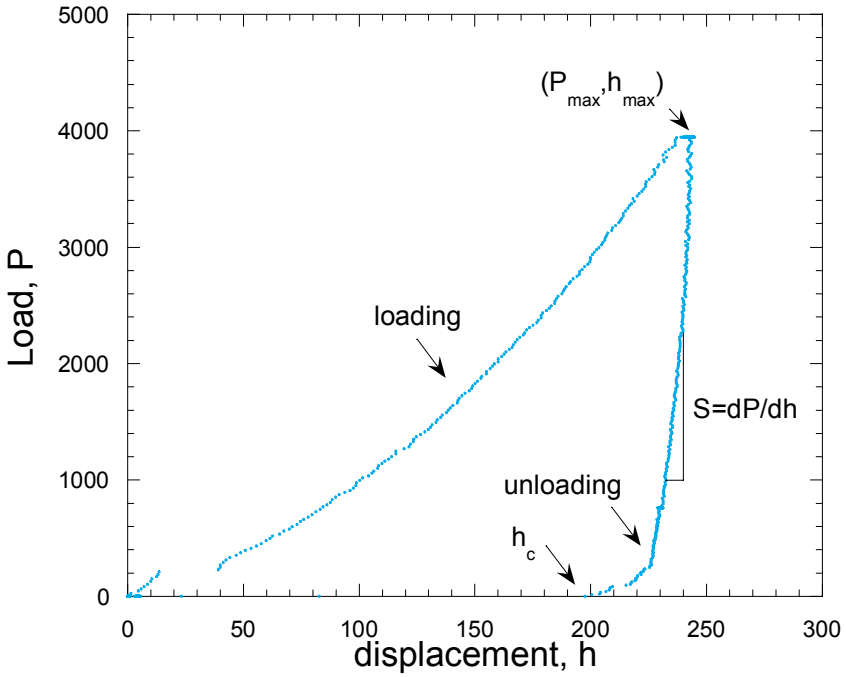


**Figure 1.1** Schematic of an indentation load displacement curve [6]

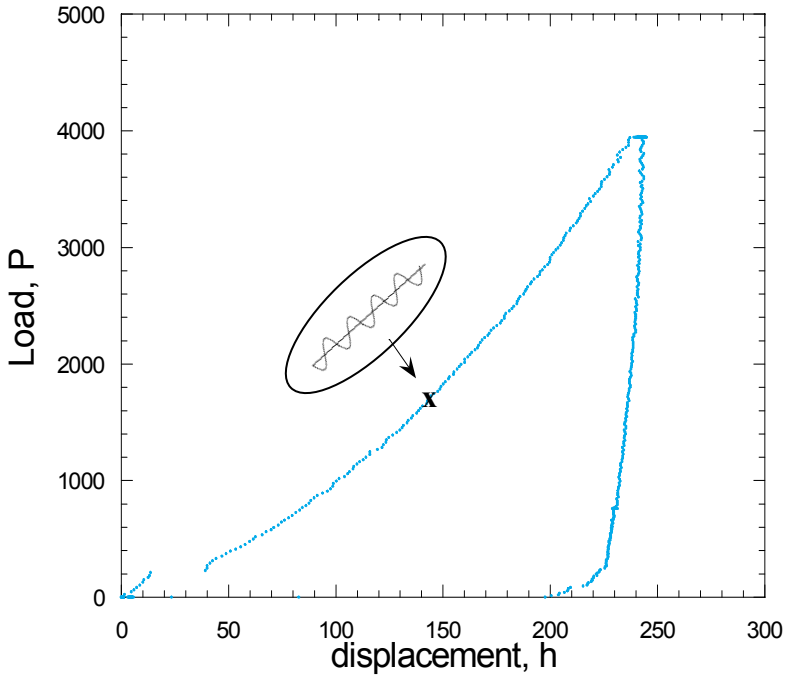


**Figure 1.2** Schematic of the continuous stiffness measurements loading cycle. The contact stiffness is measured during the loading portion of the test by imposing an AC load to the DC applied load [7]

### 1.2.2 Bulge Testing

#### 1.2.2.1 The Bulge testing technique

Another technique that is used to determine the mechanical properties of thin films and multilayers is the bulge testing technique. In this case the films are made into membranes using standard photolithograph techniques. The membranes are then glued using crystal bond 555 wax on aluminum pucks which have an opening in the center and are sealed to the end of a tube which is connected to a pressure variator. Pressure is applied on the membrane and its deflection is monitored as a function of the applied pressure using a laser vibrometer. A complete description of the testing apparatus can be found in [13]. A typical pressure deflection curve for the films tested in this study can be seen in Figure 1.3.

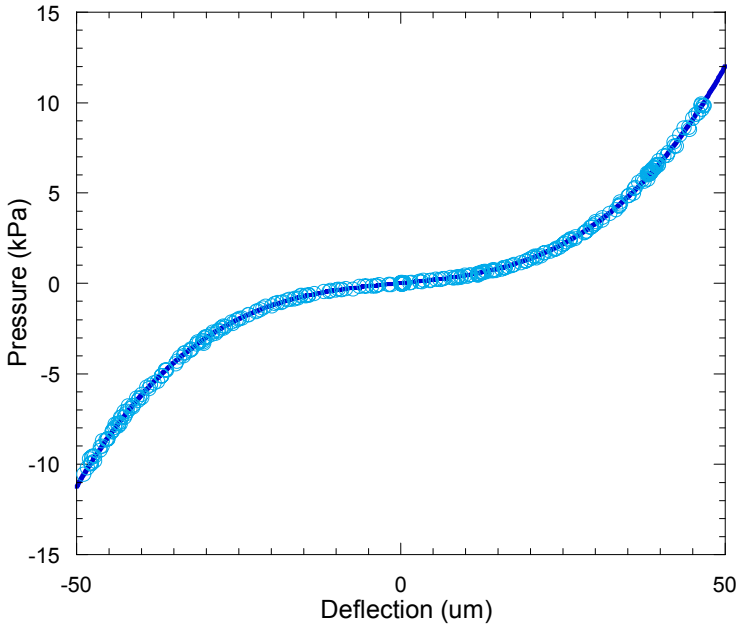


**Figure 1.3** Typical pressure deflection-curve for the films used in this study. The solid line over the data is the result of curve fitting using the general equation $P=ah+bh^3$

The pressure deflection data follow a relationship of the form [14-17]:

$$P = Ah + Bh^3 \tag{1.7}$$

where $P$ is the pressure and $h$ the deflection of the membrane. Curve fitting of the data acquired during testing allows the determination of the parameters $A$ and $B$. These fitting parameters can then be used to find the modulus and residual stress of the specimen. A variation of equation (1.7) is also used where $h$ is substituted with $h+h_o$ to account for initial offsets in deflection [18]. In order to calculate the mechanical properties of the film from the fitting parameters $A$ and $B$, the geometry of the membrane has to be taken into account. Three different geometries have been commonly used during bulge testing square, rectangular and circular and the relationship between pressure and deflection has been determined in each case. In this study only square and rectangular geometries have been used.

For square membranes the corresponding relationship has been determined using both finite elements analysis [19] and an energy minimization technique [19, 20]. For rectangular membranes with a large aspect ratio, larger than 4, the assumption of a plane strain stress state simplifies the determination of the pressure deflection relationship. The relationships for each geometry are described by the following equations [18, 20-22]:

$$P_{circular} = \frac{C_1 \sigma_o t}{\alpha^2} h + \frac{C_2 E t}{a^4 (1-\nu)} h^3 \tag{1.8}$$

$$P_{square} = \frac{C_1 \sigma_o t}{\alpha^2} h + \frac{C_2 M t}{\alpha^4} h^3 \tag{1.9}$$

$$P_{rectangular} = \frac{C_1 \sigma_o t}{\alpha^2} h + \frac{C_2 E t}{\alpha^4 (1-\nu^2)} h^3 \tag{1.10}$$

where $C_1$ and $C_2$ are geometric constants, $t$ is the thickness of the membrane, $\alpha$ is half the side length or radius of the window (circular membrane), $v$ is the Poisson's ratio, $E$ is the modulus and $\sigma_o$ is the residual stress of the film. In Table 1.1 the values for $C_1$ and $C_2$ for the three geometries are shown. Using the fitting parameters $A$ and $B$ and equating them to the corresponding terms in these equations allows the determination of the modulus and residual stress of the films.

**Table 1.1** Values for the geometric parameters $C_1$ and $C_2$

| **geometry** | $C_1$ | $C_2$ |
|---|---|---|
| Circular | 4 | 8/3 |
| Square | 3.4 | 1.83 |
| Rectangular | 2 | 4/3 |

It should be noted here that for the square geometry the membrane is under a biaxial stress state and the factor of the cubic term relates to the biaxial modulus and not the Young's modulus. However the Young's modulus $E$ is easily found by substituting $M$ with $E/1\text{-}v$ in equation (1.9) with $v$ being the Poisson's ratio of the film.

## 1.3 Scanning Electron Microscopy

The microstructures presented in this dissertation both for the laser crystals and the nanocomposites were investigated primarily using Scanning Electron Microscopy (SEM). In a Scanning Electron Microscope a beam of electrons is generated by an electron gun and

is directed on the surface of a sample through a system of electro magnetic lenses. Upon hitting the surface the electrons of the beam interact with the sample generating a number of different signals. These signals include secondary electrons (SE), back scattered electrons (BSE) and characteristic X-rays. Collection of the different signals with the appropriate detector gives information about the surface topography, the composition and the orientation of the sample.

The advantages of Scanning Electron Microscopy over optical microscopy include its high resolution and large depth of field [23].

## 1.4 X-ray Photoelectron Spectroscopy

X-ray Photoelectron Spectroscopy is a technique that allows the determination of elements present in a sample as well as the type of their chemical bonding [24]. Testing involves irradiation of the sample with soft X-rays and collection of core electrons that escape the sample by the photoelectric effect. It is a surface technique because only electrons originating from 1 to 10 nm below the sample surface can escape without significant energy loss. The electrons leaving the sample are detected by an electron spectrometer and their kinetic energies are measured. The binding energy BE of the atomic orbital from which each electron originates is calculated using the following equation:

$$KE=hv-BE-\varphi_s \tag{1.11}$$

where $KE$ is the kinetic energy measured by the analyzer, $hv$ is the energy of the soft X-rays and $\varphi_s$ is the work function of the spectrometer which is known. When a change occurs in the local chemical environment of the atom, a shift in the binding energy of the

core electrons is observed. These shifts are recorded and can give information about the chemical bonding of the elements present in a sample.

Since X-ray Photoelectron Spectroscopy is a surface technique depth profiling of a sample can only be done by using a sputtering gun which will gradually remove material from the specimen allowing the collection of XPS spectra at different depths.

## 1.5 References


**[1]** "Progress in Ceramic Lasers" A. Ikesue, Y. L. Aung, T. Taira, T. Kamimura, K. Yoshida, G. L. Messing, Annu. Rev. Mater. Res. **36** 397 (2006)

**[2]** "Tensile testing of free-standing Cu, Ag and Al thin films and Ag/Cu multilayers" H. Huang, F. Spaepen, Acta Mater. **48** 3261 (2000)

**[3]** "Tensile testing low density multilayers: Aluminum/titanium" D. Josell, D. van Heerden, D. Read, J. Bonevich and D. Shechtman, J. Mater. Res. **13** 2902 (1998)

**[4]** "The effects of decreasing layer thickness on the high temperature mechanical behavior of Cu/Nb nanoscale multilayers" N.A. Mara, T. Tamayo, A.V. Sergueeva, X. Zhang, A. Misra and A.K. Mukherjee, Thin Solid Films **515** 3241 (2007)

**[5]** "Structure and high temperature mechanical behavior relationship in nano-scaled multilayered materials" N.A. Mara, A.V. Sergueeva, A. Misra and A.K. Mukherjee, Scripta Mater. **50** 803 (2004)

**[6]** "Measurement of hardness and elastic modulus by instrumented indentation: Advances in understanding and refinements to methodology" W.C. Oliver and G.M. Pharr, J. Mater. Res. **19** 3 (2004)

**[7]** "A review of nanoindentation continuous stiffness measurement technique and its applications" X. Li and B. Bhushan, Mater. Charact. **48** 11 (2002)

**[8]** " Development of continuous stiffness measurement technique for composite magnetic tapes" X. Li and B. Bhushan, Scripta Mater. **42** 929 (2000)

**[9]** Tabor D. The hardness of metals. Oxford: Clarendon Press, 1951

**[10]** **"**Determination of plastic properties of metals by instrumented indentation using different sharp indenters" J.L. Bucaille, S. Stauss, E. Felder , J. Michler , Acta Mater. **51** 1663 (2003)

**[11]** " The correlation of indentation experiments" K. L. Johnson, J. Mech. Phys. Solids **18** 115 (1970)

**[12]** **"**Extraction of stress-strain curves of elastic-viscoplastic solids using conical/pyramidal indentation testing with application to polymers" G. Kermouche, J.L Loubet, J.M. Bergheau, Mech. Mater. **40** 271 (2008)

**[13]** "Yielding and Fracture in Nanolayered Metallic Composites" N. R. Overman, MSc Thesis, Washington State University, USA (2009)

**[14]** "Thin Film Mechanics Bulging and Stretching" W. Sauter, PhD Thesis, University of Vermont, USA (2002)

**[15]** "Analysis of the accuracy of the bulge test in determining the mechanical properties of thin films" M.K Small, W.D.Nix, J. Mater. Res. **7**(6) 1553 (1992)

**[16]** "Mechanical properties measurement of silicon nitride thin films using the bulge test" H.K. Lee, S.H. Ko, J.S. Han, H.C. Park, Microelectronics **6798** (1C) 67981C.1 (2007)

**[17]** "Plane strain bulge test for thin films" Y. Xiang, X. Chen, J.J. Vlassak, J. Mater. Res. **20**(9) 2360 (2005)

**[18]** "Bulge and Blister Testing of Thin Films and Their Interfaces," R.J. Hohlfelder, Ph.D., Stanford University, USA (1999)

**[19]** " Mechanical Behavior of Thin Films" R. P. Vinci, J.J. Vlassak, Annu. Rev. Mater. Sci. **26** 431 (1996)

**[20]** "A new bulge test technique for the determination of Young's modulus and Poisson's ratio of thin films" J.J. Vlassak, W.D. Nix., Mat. Res.Soc. **7**(12) 3242 (1992)

**[21]** "A novel bulge-testing setup for rectangular free standing thin films" A.J. Kalkman, A.H. Verbrugger, G.C.A.M. Janssen, F.H. Groen, American Institute of Physics **70** (10) 4026 (1999)

**[22]** "The elastic biaxial modulus of Ag-Pd multilayered thin films measured using the bulge test" M.K. Small, B.J. Daniels, B.M. Clemens, W.D. Nix, J.Mater.Res. **9**(1) 25 (1994)

**[23]** Electron Microscopy and Analysis ($3^{rd}$ edition), P.J. Goodhew, F.J. Humphreys, R. Beanland, Taylor and Francis (2001)

**[24]** Handbook of X-ray Photoelectron Spectroscopy, Perkin-Elmer Corporation, USA (1979)

# Chapter Two: Strengthening of Mo/Pt multilayers

## 2.1 Introduction

Since 1970 when Koehler [1] proposed that a composite material of alternating layers of two metals had the potential to exhibit higher strength than either of the individual constituents, a considerable amount of research has focused on multilayered structures. It has been shown that the strength of multilayered structures increases as the layer thickness decreases from the submicrometer to the nanometer scale [2-5]. In [4] Misra and Kung reported strength values equal to one half or one third of the theoretical strength, for layer thicknesses of a few nanometers. However the dependency of strength on the layer thickness is not monotonic but shows regions with distinct behavior [2, 5]. This implies that different mechanisms are responsible for the observed mechanical behavior at different length scales.

In [2] the hardness data for Cu based multilayered structures are presented. For large layer thicknesses $h$ (> 100 nm), the strength of the composite is proportional to $h^{-1/2}$. The dependency of yield strength on layer thickness for this length scale is the same as the dependency of yield strength on grain size for polycrystalline aggregates described by the Hall-Petch model [6-8]:

$$\sigma_{ys} = \sigma_o + kL^{-1/2} \tag{2.1}$$

where $L$ is the distance between a dislocation source and an obstacle. In the case of multilayered structures $L$ is assumed equal to the layer thickness. The Hall-Petch

dependency can be explained using a dislocation pile up model where dislocations pile up at the interface between the two layers [5].

As the layer thickness decreases a break down of the Hall-Petch regime is observed. Although the strength continues to increase as the layer thickness decreases, it becomes proportional to $h^{-a}$, with $a$ being different than 0.5. Misra et al. [2] have suggested that a single dislocation mechanism can account for this type of dependency. They based their assumption on previous work [9-11] which showed that a Hall- Petch type relationship between strength and layer thickness can still be expected and explained using a discrete dislocation pile up model [4], with the number of dislocations in the pile up being just larger than one.

A number of different effects can influence the glide of a single dislocation on a plane, such as coherency stresses, misfit dislocations at the interface, Koehler image forces and Orowan bowing and all these strengthening mechanisms were incorporated in their model. It is worth noting that to a first order approximation only for the Orowan bowing mechanism does the strength depend on layer thickness. The nanocomposite system that Misra et al. [2] used for their dislocation model was semicoherent, where the coherency stresses at the interface were relieved by a grid of misfit dislocations. At the first stages of plastic deformation, dislocations can only glide in the soft layer. The single dislocations on the glide planes cannot cross the interface; they get pinned there and glide parallel to the interface. As they glide parallel to the interface they deposit misfit-type dislocations. At higher loads however slip can be transferred across the interface and the other layer will yield as well. The total yield stress of the composite can be therefore calculated by adding

the stress needed to initiate glide in the soft layer (Orowan stress) to the stress needed for dislocation transmission across the interface and glide in the hard layer. The Orowan stress can be found by summing the energy necessary to create the extra length of the dislocation line during bowing and the work done as the glide dislocation moves against the stress field of the misfit dislocations already present at the interface [12]. The value acquired using this approach is an upper bound estimate. If the effect of misfit dislocations is ignored a lower bound estimate can be found, which seemed to better approximate the available experimental data for small layer thicknesses. In this case the coherency stresses are not completely relieved by the grid of misfit dislocations and the spacing of the misfit dislocations present is larger than the equilibrium value. In a paper that followed from the same group [5] systems with incoherent interfaces were studied and the proposed model was used to fit the available experimental data. Since no grid of misfit dislocations is present at the interface the lower bound estimate of their previous work was utilized to estimate the Orowan stress. However, while their results qualitatively agreed with the observed behavior, the model did not fit very well to the available experimental data and some refinements were done to achieve a better fit. Simulations using molecular dynamics (MD) of dislocations [13] have shown that incoherent interfaces can shear due to the stress field of a glide dislocation, causing a spread of the dislocation core and this effect was taken into account. Also although no misfit dislocations are initially present at the interface, misfit-type dislocations are deposited as the loops glide parallel to the interface and their stress field was included in the calculations. The final refinement of the model considered

the presence of elastic stress at the interface [14] which can oppose or assist the applied stress in the confined slip of single dislocations.

For thicknesses varying from a few nanometers to a couple of nanometers, the composite strength shows a maximum value and further decrease of thickness causes a decrease in the measured strength. This behavior cannot be described by the single dislocation model which predicts increase in strength with further decrease of the layer thickness. It is suggested that the maximum in strength is observed when the stress necessary for the glide of a dislocation in the soft layer becomes higher than the stress needed for dislocation transmission across the interface [2]. When this happens the dislocation loops can glide simultaneously in more than one layers and yield occurs. In this case the stress necessary for dislocation transmission determines the yield strength of the composite. Determination of the stress necessary for dislocation transmission across the interface takes into consideration a number of factors. These factors include the coherency stresses, the misfit dislocation spacing, the difference in elastic constants between the layers, the difference in the stacking fault energy and the misorientation of slip systems across the interface [2]. Hoagland et al. [15] using MD simulations showed that the transmission stress and therefore the yield strength for very small layer thicknesses, is to a first approximation independent of the layer thickness, something that agrees with the experimentally observed plateau of strength for small values of thickness.

Although the softening observed for very small layer thicknesses is not well understood, some possible explanations have appeared in literature. In [16] the thickness where the softening appears is considered to be just smaller than the thickness where loss

of coherency occurs. The resistance of the interface to dislocation transmission is assumed lower in the absence of misfit dislocations and hence the decrease in strength. Another explanation presented in [4] relates the sharpness of the interface or rather the lack of it to the observed behavior. This has been supported by some experimental data which showed that miscible systems, like Cu-Ni showed softening [17, 18] whereas immiscible systems like Cu-Ag did not [19]. However this may not be true for all systems as softening has been reported for Ag-Cr, an immiscible system [20]. The authors in [4] suggested that this didn't necessarily indicate a different softening mechanism but was rather the result of intermixing at the interface which occurred during the sputtering process. In [21] Chu and Barnett proposed a model to account for the observed mechanical behavior of multilayered structures. They modeled systems with miscible components which had the same slip systems. Their approach was that two mechanisms are operating, with one being more important at small layer thicknesses and the other more important at larger layer thicknesses. According to their model for very small thicknesses instead of having two layers with distinct composition separated by an interface of mixed composition, the composition continually changes across the bilayer period. The strength in this case is calculated using image forces [7, 22] which arise from the modulus differences due to the compositional variations between adjacent domains. The contributions from all the different domains are then summed to calculate the yield strength of the multilayer. The stress experienced by a dislocation in this case was found to decrease as the layer thickness decreases and this could explain the observed softening. For larger thicknesses the glide of dislocations within individual layers is possible and the second mechanism predicted

increase in yield strength with decreasing layer thickness. Although the proposed mechanism for very small layer thicknesses can offer a possible explanation to the mechanical behavior of multilayers, our current knowledge is still very limited at this length scale.

In the discussion so far it has been assumed that the only length scale of interest which determines the hardening behavior of the multilayered structures is the layer thickness. However as it was pointed out in [4, 8] in the case of polycrystalline multilayers both the in plane grain size $d$ and the layer thickness $h$ are length scales of interest. When the in plane grain size is much smaller than the layer thickness both grain boundaries and interfaces play a role in the observed mechanical behavior. In the same work Misra and Kung discuss a 'deformation mechanism map" for metallic layers with a 2.5% interface misfit strain which indicated which deformation mechanism is operating for various combinations of layer thicknesses and grain sizes.

## 2.2 Motivation

The above discussion has demonstrated the potential that multilayered structures have in improving the mechanical behavior of thin films which are used in numerous applications. It is also apparent that the mechanisms which are operating at the nanoscale and control the mechanical properties of the multilayers are not fully understood, resulting in the increased research interest. Two reasons led to the choice of Mo/Pt multilayers as the system used in this study. The first was a practical one; the need to improve the mechanical properties of Pt thin films that are extensively used in Microelectromechanical systems

(MEMS). The second was the opportunity to study a system different from the Cu based systems that are mainly presented in literature.

MEMS are small integrated devices that can be used as sensors or actuators and are made possible using fabrication techniques originally developed for the semiconductor industry [23]. The piezoelectric effect is utilized in these applications [24]. In sensors the mechanical response of a piezoelectric thin film to an applied electric field is used. In an actuator the piezoelectric thin film is subjected to mechanical deformation in order to generate electrical power (inverse piezoelectric effect). The basic part of the system is the piezoelectric thin film which is deposited on a support layer, commonly Si. The membrane is connected to the secondary parts of the device that are either used for the sensing process or to transfer the generated power, by metal contacts. Pt is one of the metals typically used for these contacts. The piezoelectric membranes exhibit better performance when they are operated at high strains [25]. At these high strains the support layer doesn't add to the efficiency of the device hence the interest in removing it from the structure. In this case the bottom electrode, which is commonly a Pt thin film, would assume a dual role as the electrical component and the support layer of the piezoelectric actuator. However, Pt thin films have high residual tensile stresses after deposition and subsequent MEMS processing, and are not suitable as free standing films for membranes with a thickness on the order of 1 μm and lateral dimensions on the order of mm's.

Layering of Pt with another metal was the approach used here to improve the mechanical properties of the film and allow fabrication of free standing membranes. The metal chosen as the second constituent in the layering sequence was Mo which as a bcc

metal forms an incoherent interface with the fcc Pt. The formation of the incoherent interface was expected to result in high strength multilayered films.

The binary phase diagram of Pt- Mo [26] shows that the two metals are miscible and can also form a number of different intermetallics. This makes the Pt-Mo system more complicated than the incoherent systems that have already been investigated and presented in literature, which showed no appreciable solubility. If the processing conditions of the multilayers allow the formation of a Pt - Mo solid solution or that of an intermetallic the effect of additional strengthening mechanisms to the hardening behavior of multilayers could be investigated. In [27] the authors showed that solid solution strengthening in thin Pt- Ru films showed similar dependency on the Ru solute concentration as would be expected for bulk materials.

## 2.3 Experimental details

The nanolayered films used in this study were deposited by sequential DC magnetron sputtering at nominally room temperature. Films with 4, 10 and 20 layers were sputtered on thermally oxidized Si wafers, which were rotated over the sputtering targets for improved uniformity. The thickness of the $SiO_2$ layer was approximately 120 nm. Mo was directly sputtered on the oxide layer for all structures. The nominal thicknesses of the individual layers for each nanocomposite used in this study are shown in Table 2.1. Samples with nominal thicknesses of 25 nm/ 30 nm and 100 nm/ 100 nm were also sputtered on $Si/SiO_2$ windows. Standard photolithography techniques were utilized to create these windows and both square and rectangular geometries were fabricated with

nominal lateral dimensions of 4mm x 4 mm and 1.5 mm x 10 mm correspondingly. The background pressure in the chamber prior to sputtering was $1\cdot 10^{-6}$ Torr. All Mo layers were sputtered at a regulated power of 200 W and an Ar pressure of 3.8 mTorr while the Pt layers were sputtered at a regulated power of 60 W and an Ar pressure of 11 mTorr. The use of the same sputtering conditions for all the nanostructures ensured that the deposition rates in each case were kept constant and different layer thicknesses were obtained by accordingly varying the deposition time. In addition to the Mo/Pt multilayers that were deposited on Si wafers and Si/ $SiO_2$ windows, films with the bilayer periods 25 nm / 30 nm and 100 nm/ 100 nm were also sputtered on glass substrates which were used to collect X-ray diffraction patterns. The use of glass substrates ensured that only peaks originating from the films were collected. A Siemens D-500 X-ray powder diffractometer with a Cu X-ray tube was used to collect the diffraction data.

The top view and cross sections of the nanocomposites, which were acquired by cleavage, were examined using a FEI Sirion 200 Scanning Electron Microscope. The actual layer thicknesses and total thicknesses of the multilayers were measured from the SEM micrographs and are also presented in Table 2.1 along with the nominal thicknesses.

The mechanical properties of the films were measured using a Hysitron Triboscope with the nanoDMA$^{TM}$ attachment which allowed the recording of contact stiffness at various points during loading, allowing modulus and hardness to be measured as a function of penetration depth for a given indentation. A calibrated Berkovich tip was used for the indentations. All hardness values reported in this chapter refer to values measured at contact depths that correspond to approximately 10 % of the total film thickness. This

choice minimizes the influence from the substrate on the measured values and at the same time is deep enough to minimize any effects from surface roughness. Each sample was indented for at least 5 times and 80 measurements per indent were collected. The values of hardness and modulus reported here are averages of the indentations at a contact depth equal to 10% of the film thickness.

A bulge testing apparatus was also used to measure the modulus and residual stress of the films that were fabricated into membranes. A Polytec OFV 511 scanning laser vibrometer recorded the displacement of the center of the membrane as a function of pressure. The pressure was applied using a Meriam Pressure/Vacuum variator. For all the films that were used at least 20 tests were performed and the residual stress and modulus reported in each case are averages of these measurements.

XPS spectra were also collected from the 100 nm/100 nm and 25 nm/ 30 nm Mo/Pt films with an AXIS-165 manufactured by Kratos Analytical Inc using an achromatic MgK$\alpha$ (1254 eV) X-ray radiation with a power of 210 W. The spectrometer was calibrated using the Au 4f $_{7/2}$ peak at 84.2 eV and the Ag $3d_{5/2}$ peak at 368.5 eV. In order to investigate the chemistry of the nanolayered films depth profiles were collected. The first two layers of each nanostructure were probed by using $Ar^+$ sputtering at 4keV and collecting XPS spectra at regular sputtering time intervals. Mo and Pt films deposited at the same sputtering conditions as the individual layers of the nanocomposite were used as reference samples for the XPS analysis.

## 2.4 Results and discussion

### 2.4.1 Strength enhancements with decreasing layer thickness

A typical view from the surface of the nanocomposites can be seen in Figure 2.1. The in plane grain size is small, ranging from 10 to 30 nm, with the grains appearing faceted. Some voiding along the grain boundaries is also observed, indicative of Zone I film growth. These characteristics are common for all films used in this study irrespective of layer thickness. Typical cross sections, acquired using cleavage, are presented in Figure 2.2. The columnar structure of the Pt grains can be clearly seen for the structures with the thicker layers.

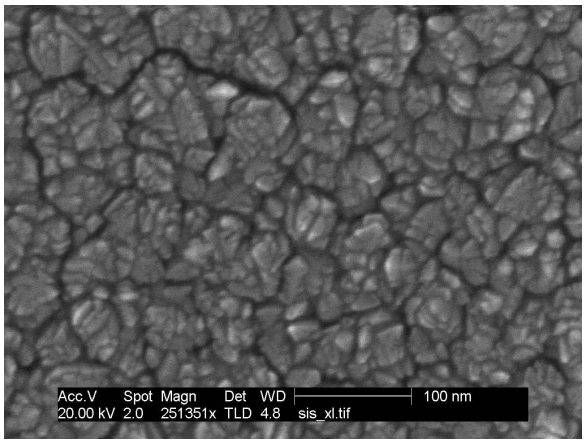


**Figure 2.1.** Top view of the 35 nm/100 nm Mo/Pt film. The grains appear faceted and some voiding along the grain boundaries is present

The hardness and modulus as a function of contact depth for all films was determined using nanoindentation and the corresponding graphs are presented in Figures 2.3 and 2.4. The values of modulus and hardness at a contact depth corresponding to approximately 10% of the total film thickness are reported in Table 2.1. In the same table

the hardness and modulus for the reference Mo and Pt films with a thickness of 500 nm are reported. The Pt film with the 500 nm thickness had a considerable amount of surface roughness making it difficult to accurately report the values for modulus and hardness.

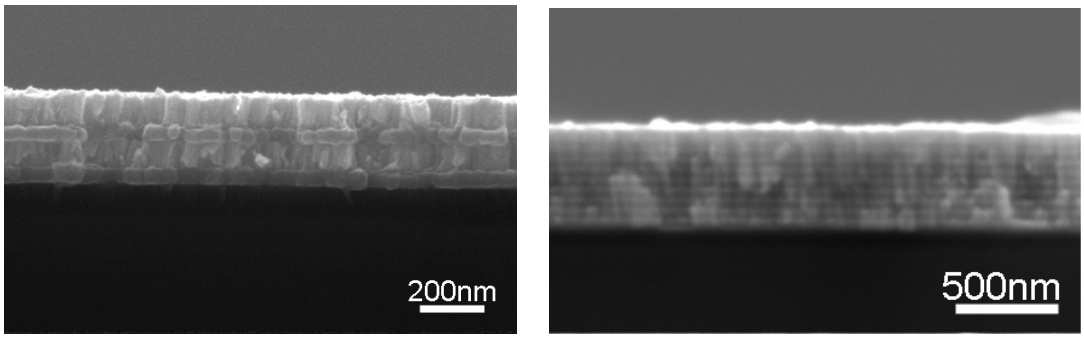


**Figure 2.2** Typical cross sections for 4 layered and 20 layered composites

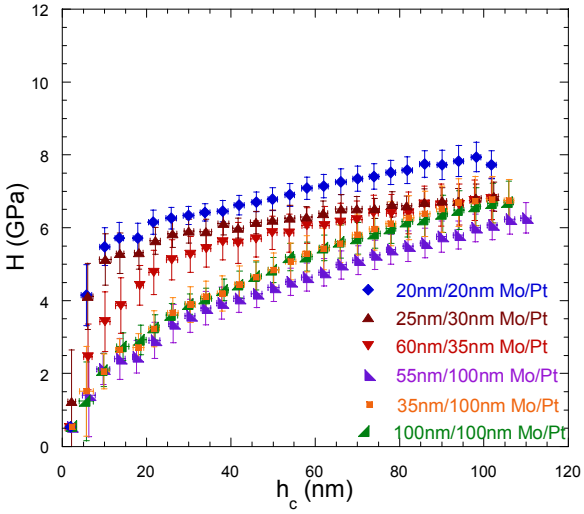


**Figure 2.3** Hardness as a function of contact depth for all the multilayers used in this study. The smaller the thickness of the Pt layer the harder the films appear

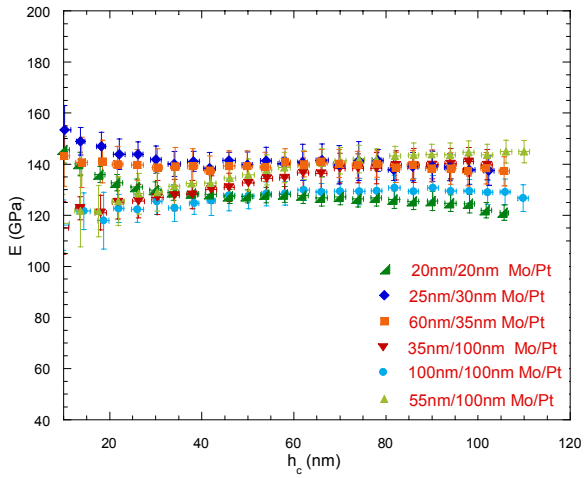


**Figure 2.4** Elastic modulus of all multilayers as a function of contact depth

The moduli for the as deposited Mo/Pt films are considerably lower than what would be expected from a simple rule of mixtures from their bulk constituents. However the fact that the modulus value for the Mo film is also considerably lower than the one for bulk Mo (Table 2.1) indicates that this behavior is not a result of the multilayered structure but rather of the specific thin film system. Modulus values for Mo thin films that are lower than the bulk value have been reported in literature before [28]. In [29] Spaepen and co-workers found lower modulus values for free standing FCC films and attributed this behavior to the high grain boundary area which can provide a possible source for defects thus lowering the elastic properties of the film. In [30] the density of Mo films was correlated to the Ar pressure and it was shown that higher Ar pressures result in lower film densities, voided grain boundaries and oxygen incorporation. The formation of oxides along the grain boundaries could account for the decrease in the elastic modulus of the Mo thin films when compared to that of the bulk material. The slightly voided grain boundaries

of the Pt layer could act as fast diffusion paths for oxygen which could subsequently form Mo oxides impacting the elastic properties of the films.

The low modulus values for the multilayers and the Mo reference film were further confirmed using the bulge testing technique. Pressure deflection data for both the 500 nm Mo film and the 100 nm/ 100 nm Mo/Pt multilayer deposited on 2.5 μm $Si/SiO_2$ square windows were collected. The biaxial modulus of the membranes (film and substrate) was determined by curve fitting the pressure deflection data and a weighted average with thickness for the Poisson's ratio was subsequently used to find the Young's modulus of the membranes. Poisson's ratios of 0.17, 0.22 [31], 0.31 and 0.38 were used for the $SiO_2$, Si, Mo and Pt layers respectively to determine the average ratio value. Finally the Young's modulus of the film alone was calculated using the following relationship:

$$E_{tot} = \frac{t_{subs}}{t_{tot}} \cdot E_{subs} + \frac{t_{film}}{t_{tot}} \cdot E_{film} \qquad (2.2)$$

where $t_{subs}$, $t_{film}$, $t_{tot}$ are the thicknesses of the substrate, the film and the membrane and $E_{subs}$, $E_{films}$, $E_{tot}$ are the corresponding values of the Young's modulus.

The moduli measured using nanoindentation and those determined using the bulge testing technique for the two films (Table 2.2) are statistically similar indicating that the low values are a true property of this particular structure and system. The small variation in the elastic modulus of the multilayer as determined using both methods is the result of small differences in the thickness of the Mo layer.

**Table 2.1** Modulus and hardness values for all multilayered Mo/Pt films used in this study

| Mo/Pt film | H (GPa) | E (GPa) |
|---|---|---|
| 20 nm/20 nm (18 nm/21 nm) | 6.62 ± 0.26 | 128.19 ± 3.21 |
| 25 nm/30 nm (25 nm/29 nm) | 6.29 ± 0.29 | 140.17 ± 2.59 |
| 60 nm/35 nm (60 nm/34 nm) | 5.85 ± 0.52 | 138.96 ± 5.77 |
| 35 nm/100 nm (33 nm/94 nm) | 3.67 ± 0.41 | 125.52 ± 6.53 |
| 55 nm/100 nm (55 nm/107 nm) | 3.8 ± 0.45 | 131.36 ± 7.12 |
| 100 nm/100 nm (93 nm/102 nm) | 4.29 ± 0.30 | 124.69 ± 4.26 |
| Mo film (500 nm) | 5.86 ± 0.56 (~50 nm contact depth) | 130.88 ± 7.43 |
| Pt film (500 nm) | 1.12 ± 0.2 (~ 100 nm contact depth Large surface roughness) | 86.62 ± 6.13 |

**Table 2.2** Comparison of Young's modulus measured with nanoindentation and bulge testing

| Film | E (GPa), nanoindentation | E (GPa), bulge testing |
|---|---|---|
| Mo (500 nm) | 130.88 ± 7.43 | 144.48 ± 8.54 ($\nu$ = 0.2338) |
| Mo/ Pt 100 nm/ 100 nm | 124.69 ± 4.26 ( true layer thickness 93 nm/ 102 nm) | 133.98 ± 11.98 ($\nu$ = 0.2353) ( true layer thickness 110 nm/ 100 nm) |

The results presented in Table 2.1 show that when the thickness of the Pt layers is kept constant at approximately a 100 nm for the composites with 4 layers, the hardness values were similar despite the different Mo layer thickness. This indicates that, for the bilayer periods used in this study, the soft layer primarily determines the strengthening behavior of the multilayers, in accordance with previous models [2]. In [2] the yield strength of the multilayer is described as the sum of two terms; the stress necessary to cause dislocation glide in the soft layer and the stress necessary for dislocation transmission and yield of the hard layer. The stress for dislocation glide in the soft layer depends on the thickness of the layer whereas the stress for dislocation transmission does not change assuming that the structure of the interface does not depend on the bilayer period. This implies that nanostructures with the same Pt thicknesses, but different hard layer thicknesses would have similar hardness, as was observed here.

The hardness data presented in Table 2.1 were converted to flow stress by dividing them by 2.7 [32] and were plotted as a function of the Pt layer thickness (Figure 2.5). The bilayer periods used in this study correspond to lengths where the CLS model has been used to describe the strengthening behavior of other incoherent systems [2, 5]. In [5] a modified CLS model has been used to describe the hardening behavior of the composite with the strength given by:

$$\sigma_{cls} = M\frac{\mu b}{8\pi h'}\left(\frac{4-\nu}{1-\nu}\right)\left[\ln\frac{\alpha h'}{b}\right] - \frac{f}{h} + \frac{C}{\lambda} \qquad (2.3)$$

where $M$ is the Taylor factor, $\mu$ is the shear stress, $b$ is the Burgers vector of the glide dislocation, $h'$ is the layer thickness $h$ projected on the glide plane, $\nu$ is the Poisson' ratio, $\alpha$ represents the core cutoff parameter, $f$ is the interface stress, C is equal to $\mu b/(1-\nu)$ and $\lambda$ is

the equilibrium spacing of the misfit dislocations array at the interface. The first term of the equation corresponds to the stress necessary to initiate dislocation glide in a layer of thickness $h$ whereas the second term accounts for the stress present at the interface due to elastic deformation. The third term describes the stress opposing the glide of dislocation loops due to misfit dislocations already present at the interface. Since the system is incoherent these dislocations are deposited as the confined dislocation loops glide parallel to the interface. Equation (2.3) was used here to curve fit the strength as a function of layer thickness data for the Mo/Pt system. The values of $\mu$= 61 GPa, $b$= 0.28 nm and $\nu$ = 0.38 used in (2.3) correspond to the Pt layer. A value of 3.1 was assumed for the Taylor factor and $f$ was set equal to 2 J/m$^2$, a typical value for interfacial energies, since this value was not available from atomistic simulations for the Mo/Pt system. The core cut-off parameter $\alpha$ was set equal to 0.2; a value that has been used for the Cu/Nb incoherent system [5]. The equilibrium spacing of the misfit dislocations at the interface, $\lambda$, was kept as a fitting parameter and it was found equal to 26 nm, a reasonable value for the spacing of misfit dislocations. The curve fitted to the experimental data is represented by the solid line in Figure 2.5. The good agreement between the modified CLS model and the data for the Mo/Pt system shows that the single dislocation strengthening mechanism can describe the observed mechanical behavior in this case.

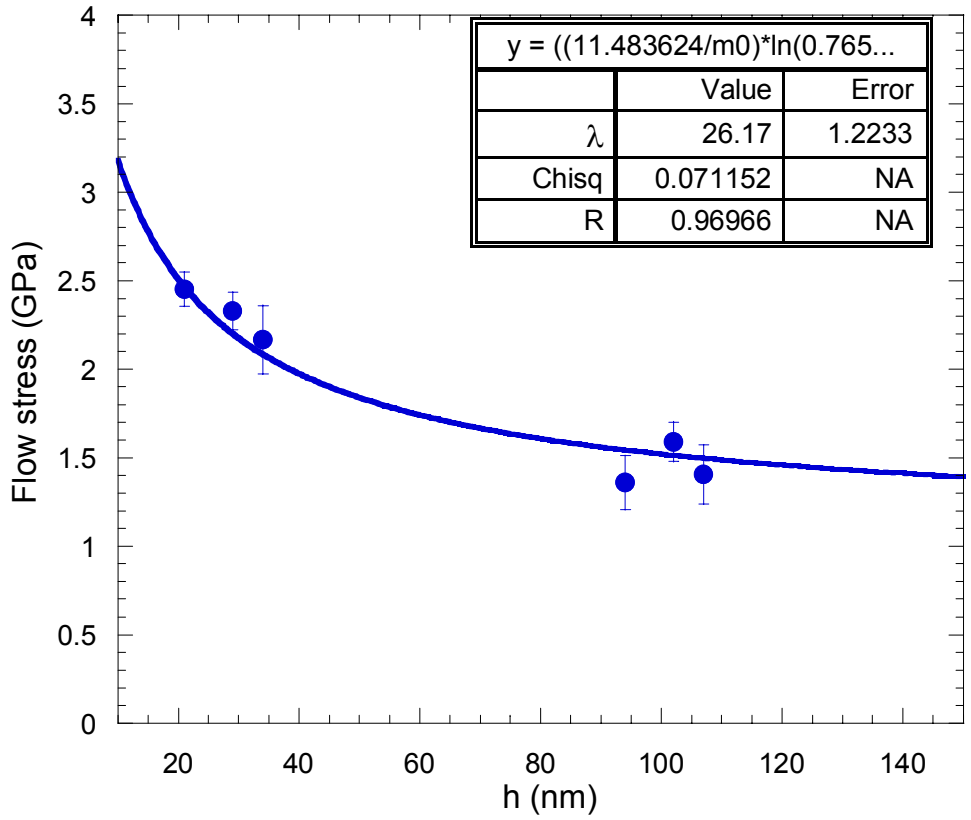


**Figure 2.5** Fitting of the experimental data for the Mo/Pt system using the modified CLS model [5]

If the nanocomposite film does not show significant strain hardening it is expected that the flow stress described by equation (2.3) will show good agreement with the flow stress calculated from hardness data which corresponds to a plastic strain of about 7 % [5]. The good agreement between the two stresses for the Mo/Pt nanocomposites, suggests that the system under investigation shows little strain hardening. This was confirmed by indenting the 100 nm/100 nm Mo/Pt film with both a Berkovich and a cube corner tip and finding in each case the hardness. Different tip geometries correspond to different

representative strains; approximately 7% for a Berkovich tip and 22% for a cube corner tip [33], hence if strain hardening does occur the hardness values will be considerably different for the two tips. However, as it can be seen in Figure 2.6 the hardness of the films didn't change significantly for the different strains indicating that the Mo/Pt nanocomposites have a low strain hardening coefficient.

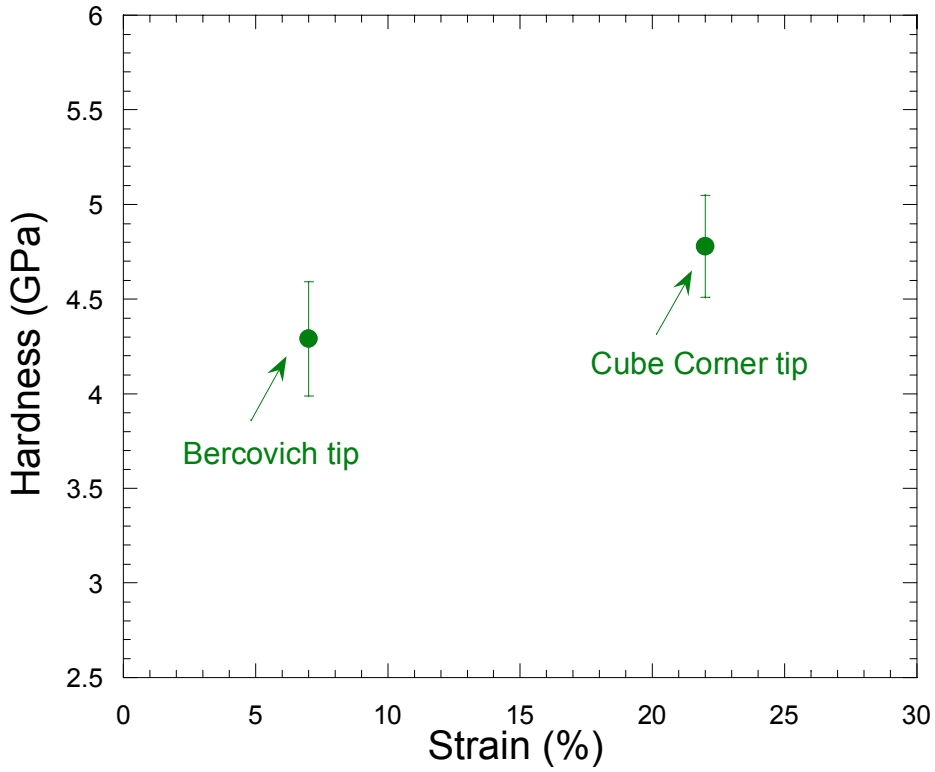


**Figure 2.6** Hardness of Mo/Pt films as measured with nanoindentation for different representative strains.

### 2.4.2 Aging of multilayered films

The nanoindentation data presented in Figures 2.3 and 2.4 were collected soon after the multilayers were sputtered. These measurements were repeated after 3 months to investigate whether aging of the films in ambient conditions affected their mechanical properties. Comparison of the hardness values for the as deposited and aged films indicated that the hardness of the nanocomposites has increased over time, as shown in Figure 2.7 for the 60 nm/35 nm and 25 nm/ 30 nm Mo/Pt case. However no change in the modulus of the same films occurred over time (Figure 2.8). Micrographs taken from the top and cross sections of the aged samples revealed no significant changes in microstructure that could account for the apparent change in strength. X-ray photoelectron spectroscopy was subsequently used to examine the composition and chemical bonding of the films.

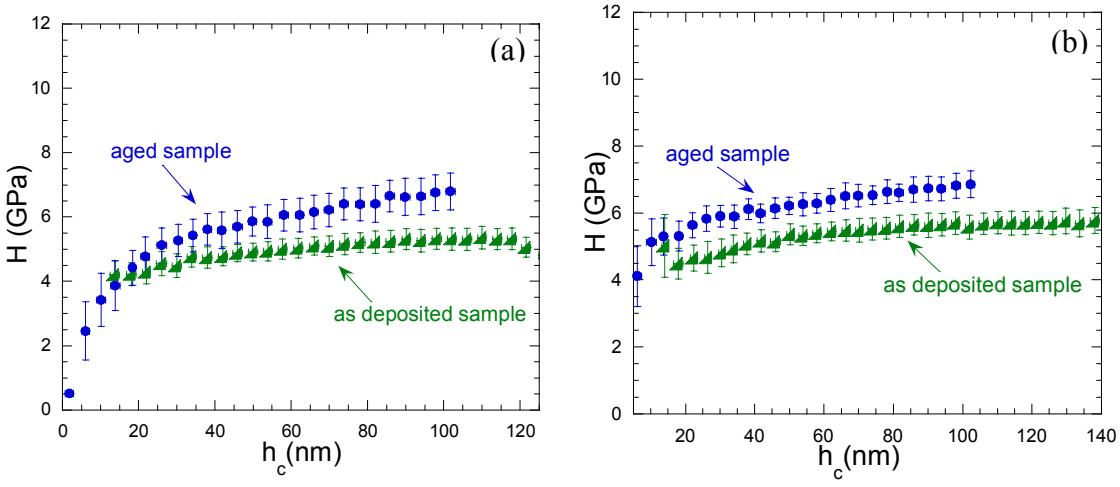


**Figure 2.7** Changes in the hardness of the **(a)** 60 nm/ 35 nm and **(b)** 25 nm/ 30 nm Mo/Pt films over time. Aging of the films in ambient conditions (for 3 months) has improved their strength

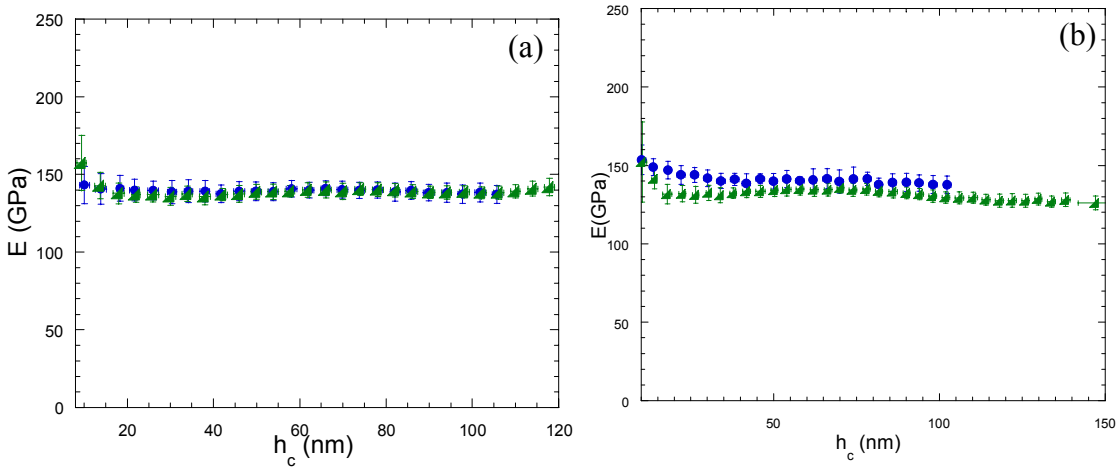


**Figure 2.8** Despite the changes in the hardness of the **(a)** 60 nm/ 35 nm and **(b)** 25 nm/ 30 nm Mo/Pt film with aging, the modulus of the films remained unchanged

Depth profiling of the aged 100 nm/ 100 nm and 25 nm/ 30 nm Mo/Pt films, using XPS, indicated the presence of Mo oxides in the Mo layer. The samples were $Ar^+$ sputtered for predetermined amounts of time and XPS spectra were collected at the end of each sputtering cycle. The depth profile for the two top layers of the 4 layer structure is presented in Figure 2.9. In addition to the presence of Mo and Pt, O was also detected in the film and its concentration tracked with the concentration of Mo. Peak deconvolution of the Mo 3d spectra (Figure 2.10) collected from well within the Mo layer, at a sputtering time of 11400 s, indicated that in addition to elemental $Mo^0$, at a binding energy of 228.1 eV in good agreement with literature values [34,35] , a weak peak at 229.4 eV was also present (discussed in more detail in Chapter 3). This peak was associated to $Mo^{+4}$ species due to the formation of $MoO_2$ and was also found in the reference Mo film. Similar results were obtained for the first two layers of the 25 nm/ 30 nm Mo/Pt nanocomposite with a total of 20 layers (Figure 2.11). These results point to oxygen incorporation in the

multilayer structure, possibly along the Pt voided grain boundaries and the formation of oxides. The Pt 4f spectrum (Figure 2.12) acquired after 3400 s of Ar sputtering, well within the Pt layer, showed no peak shift. Pt in the aged samples appears in its elemental metallic form, $Pt^0$.

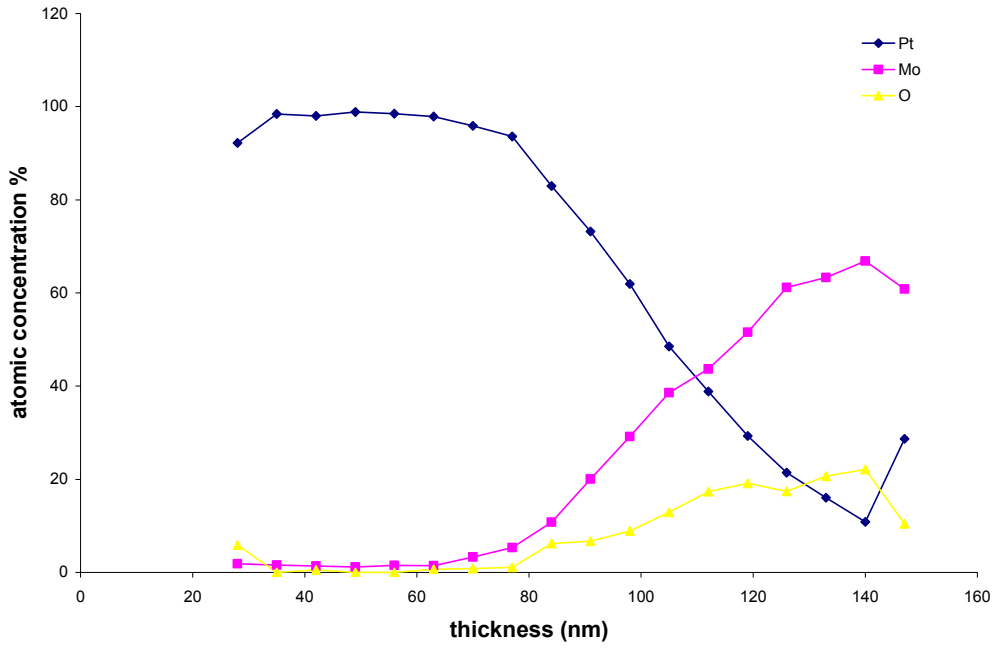


**Figure 2.9** Depth profiling of the 100 nm/ 100 nm Mo/Pt film. The presence of O is detected in the multilayer and its concentration tracks with that of Mo

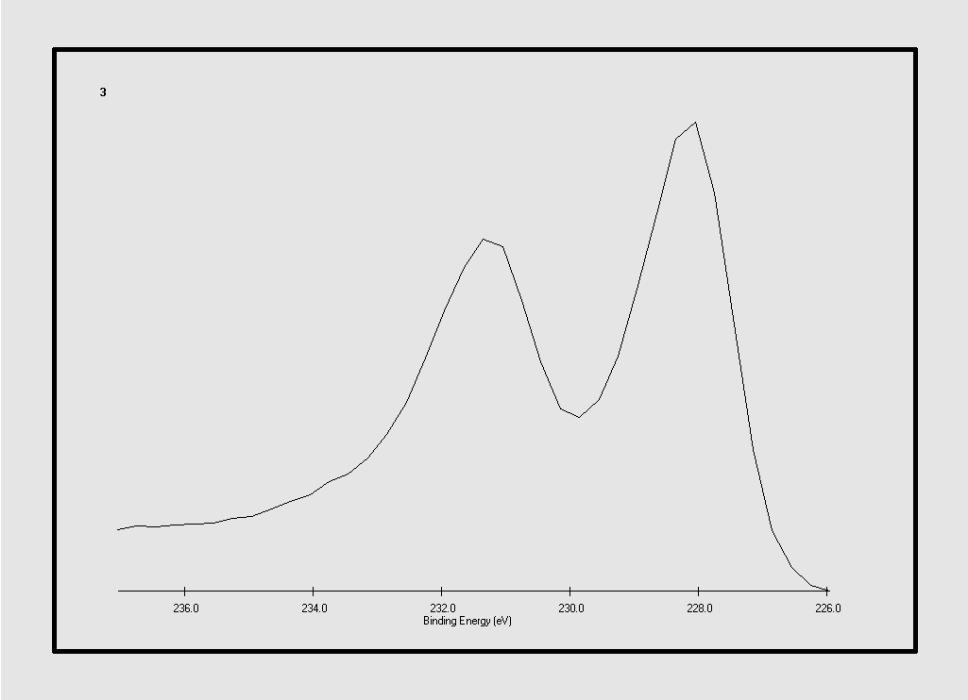


**Figure 2.10** Mo 3d XPS spectrum. The position of the peaks appears shifted compared to the binding energy of elemental Mo. This shift is attributed to the presence of oxygen in the lattice

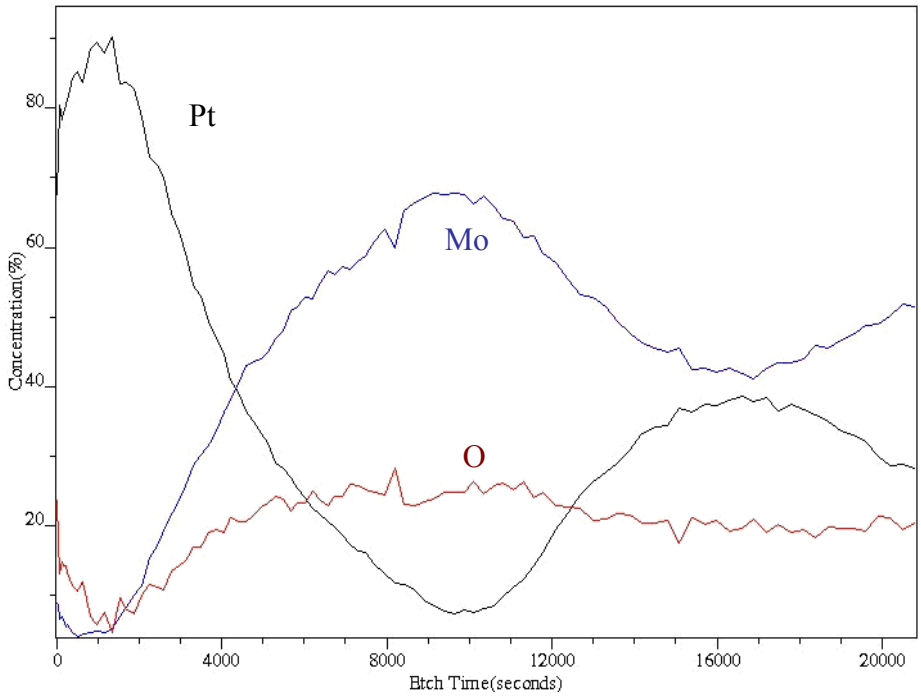


**Figure 2.11** Depth profiling of the aged 25 nm/ 30 nm Mo/Pt film reveals the presence of O in the sample.

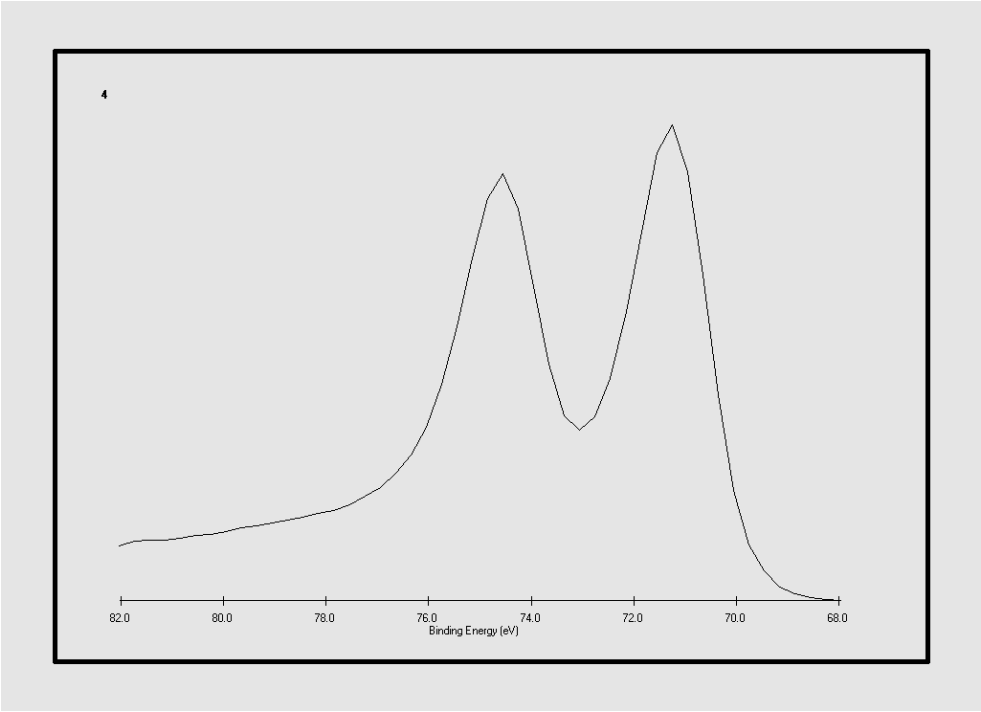


**Figure 2.12** Pt 4f XPS spectrum. No shift of the peak is observed indicating that Pt is in its metallic form and no intermetallics with Mo have formed

The oxidation of Mo can occur in the deposition chamber during sputtering or by post-deposition exposure of the films in air. In [30] the presence of O in sputtered Mo films was attributed to post deposition oxidation and the oxygen content was larger in less dense structures, with Ar pressure during sputtering controlling the density of the films. Oxygen incorporation in Mo causes lattice expansion and can make the stress of the film more compressive [36]. In [37] the oxidation of tungsten films exposed to air at ambient temperature was studied. In this case it was shown that for porous (zone I) films oxygen incorporation at the voids was possible, causing the films to become more compressive with time. The authors did not observe a similar stress evolution when the films were kept under vacuum. These studies indicate that the introduction of oxygen in the Mo layer is

possible, especially considering the columnar structure and slightly voided boundaries of the Pt layers. If oxidation does indeed occur with post deposition exposure of the films in air it could account for the observed increase in hardness assuming that the Mo oxides are harder or that precipitate hardening occurs.

Since oxygen incorporation in Mo films has been associated with stress changes, more specifically an increase in compressive stresses, one would expect the residual stresses of the Mo layers to change with aging time if the oxygen content increases. This change of stress in the Mo layers would not affect the stress in the Pt layers although the net stress of the nanocomposite would change according to the following equation [38]:

$$\sigma h = \sigma_A h_A + \sigma_B h_B \tag{2.4}$$

where $h$ is the period of the structure , $\sigma_A$, $\sigma_B$ are the stresses of the individual layers A and B and $h_A$ and $h_B$ are the corresponding layer thicknesses. Equation (2.4) ignores any interfacial stresses that could be present in the nanolayered film. This correlation between the oxygen present in the Mo layers and the changes in residual stress offered an indirect way to check whether post deposition oxidation of the Mo layers did indeed occur.

Changes in the residual stress of thin films with increase in the oxygen content have been reported in literature for other material systems [39, 40]. In [39] the oxidation of TiN thin films at room temperature was studied and the increase of the compressive stresses in the films with time was correlated to the different stages of the oxidation process and the increase of O in the films. A similar evolution of the compressive stress after exposure in air was reported for Ta films in [40].

In order to check whether any changes in the net residual stress, associated with changes in the O content of Mo, occur with aging, Mo and Mo/Pt films with two different bilayer periods were deposited on $Si/SiO_2$ windows approximately 2.5 μm thick. The mechnanical properties of these membranes were monitored using the bulge testing technique. Pressure deflection curves were recorded and fitting parameters from these curves were used to calculate the modulus and residual stress of the films.

The Mo films were first tested as soon as they were removed from the sputtering chamber and their elastic modulus was measured equal to 144.48 ± 8.54 GPa whereas the residual stress of the structure was 19.52 ± 1.07 MPa. The membranes were left in ambient conditions and although no buckling was present on the day of sputtering, which allowed measurements using the bulge testing technique, buckles appeared on the film surface the next day (Figure 2.13). The buckling of the Mo films prevented further measurements of the residual stress. This buckling however, indicated an increase in the compressive stress of the films consistent with an increase in oxygen content. X-ray diffraction data collected on days 1 and day 20 after sputtering didn't detect a phase change in the films and only Mo peaks were present in both patterns (Figure 2.14). Since the presence of oxygen in the Mo films and the formation of $MoO_2$ has been verified by XPS from the shift of the elemental peak (Figure 2.15), the XRD results point to very small dimensions of the forming oxides. The observed increase in the compressive stress combined with the presence of oxides in the Mo film supports the assumption that post deposition oxidation was responsible for the changes in residual stress.

After verifying that a change in the residual stress of the Mo films indeed occurs upon exposure in air, the stress evolution for the Mo/Pt nanocomposites was investigated. Two different multilayers were sputtered on the 2.5 μm thick $Si/SiO_2$ windows; one with bilayer thickness of 25 nm / 30 nm and a total of 20 layers and one with bilayer thickness of a 100 nm/100 nm for a total of 4 layers. Both square and rectangular window geometries were used. In the case of the 25 nm/ 30 nm Mo/Pt films all membranes, both square and rectangular, buckled immediately after deposition hence no further testing was possible (Figure 2.16). For the rectangular geometry some permanent deformation could be seen immediately after deposition however the regular pattern of buckles (Figure 2.16 (b)) did not appear until several days after sputtering, implying that the compressive stresses in the film increased with time.

The 100 nm/ 100 nm Mo/Pt films did not buckle, allowing us to study the evolution of mechanical properties with aging in ambient conditions. The first set of data was collected on the day of sputtering and then measurements were repeated over an extended period of time. In Figure 2.17 the evolution of the net residual stresses with time is presented. It is apparent that for the first days after sputtering the stress became more compressive, with the highest change occurring within the first 24 hours. Analysis of the residual stress data showed that the difference between the values for the first and second day were statistically significant with a t probability of less than 0.0001. As more days elapsed a plateau in residual stress was observed. This change in residual stress where a rapid increase is followed by a plateau in stress values, correlates with what would be expected for the amount of oxygen incorporated in the film during a diffusion controlled

process. The oxygen content would increase rapidly upon initial exposure of the film in air before practically reaching a plateau for longer times. In this case however, 15 days after sputtering partial relaxation of the residual stress was observed. This relaxation of the residual stress with time hasn't been reported for other thin film systems where changes in stress were attributed to O incorporation [39, 40]. The difference between those systems and the one studied here is the presence of interfaces with a large surface area compared to the volume of the nanostructure. These interfaces probably played a role in the partial relaxation of the residual stress which could involve local rearrangement along the interface boundaries to accommodate some of the stress. Despite the change in residual stress no change was observed for the elastic modulus of the films (Figure 2.18) which stays constant over time in agreement with the results of nanoindentation.

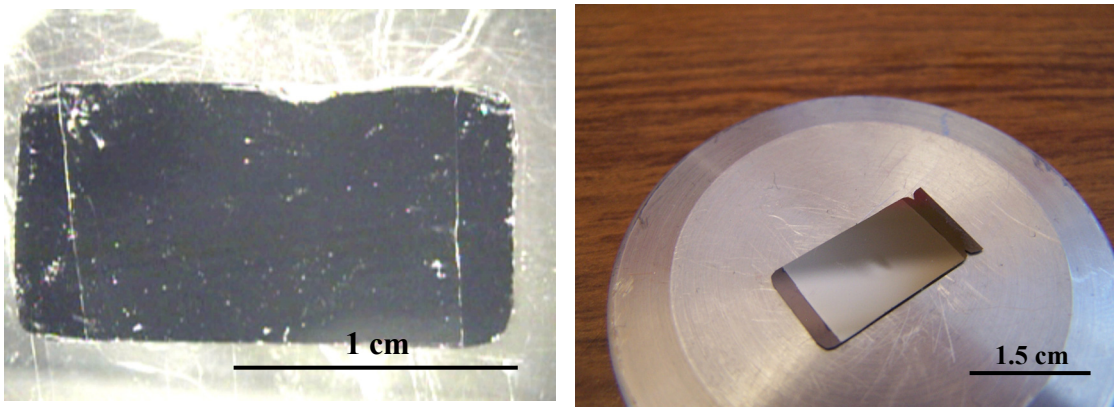


**Figure 2.13 (a)** Surface of the Mo membrane on the first day of testing. No buckles were present on the surface **(b)** Surface of the same Mo membrane the second day after sputtering when buckles could be seen on the surface

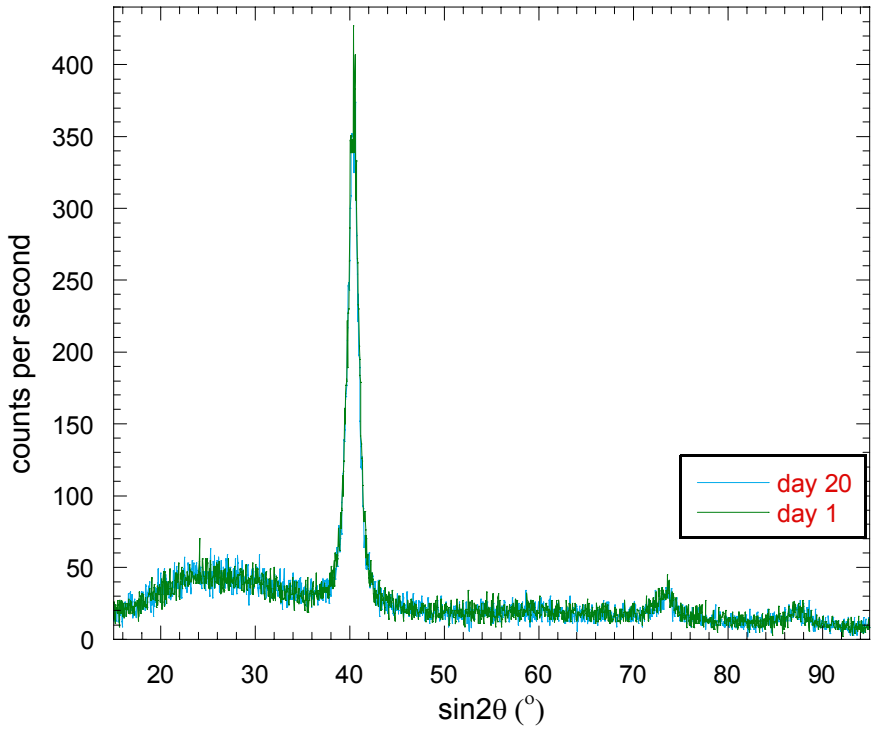


**Figure 2.14** X-ray diffraction patterns taken from the Mo film deposited on the glass substrate. No change in the phases present is detected over time

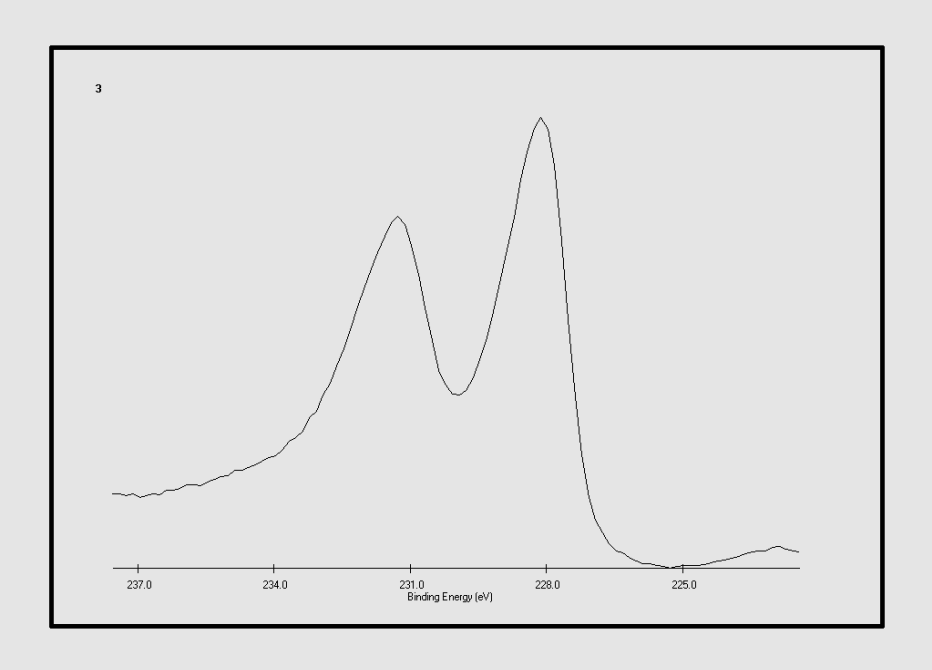


**Figure 2.15** Mo 3d XPS spectrum taken from the 500 nm thick Mo film deposited on the Si substrate. The peak shift from the binding energy corresponding to elemental Mo is attributed to the presence of oxygen in the lattice

X-ray diffraction patterns collected from the Mo/Pt films over a period of time following sputtering and exposure in air, again did not capture the formation of Mo oxides (Figure 2.19).

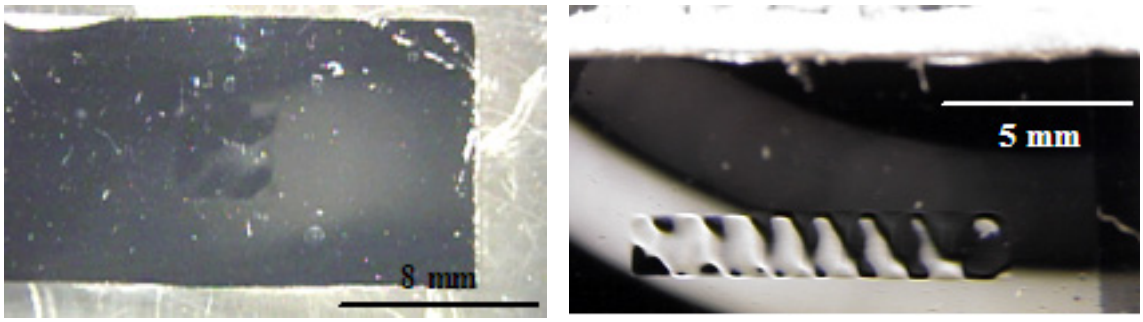


**Figure 2.16 (a)** Buckling of the 30 nm/ 25 nm Mo/ Pt film deposited on a square window which was observed directly after the membranes were removed from the sputtering chamber. **(b)** Although buckling of the 30 nm/ 25 nm Mo / Pt rectangular membranes was apparent as soon as the sputtering of the multilayers was complete, the regular pattern of buckles presented in this photograph formed several days afterwards

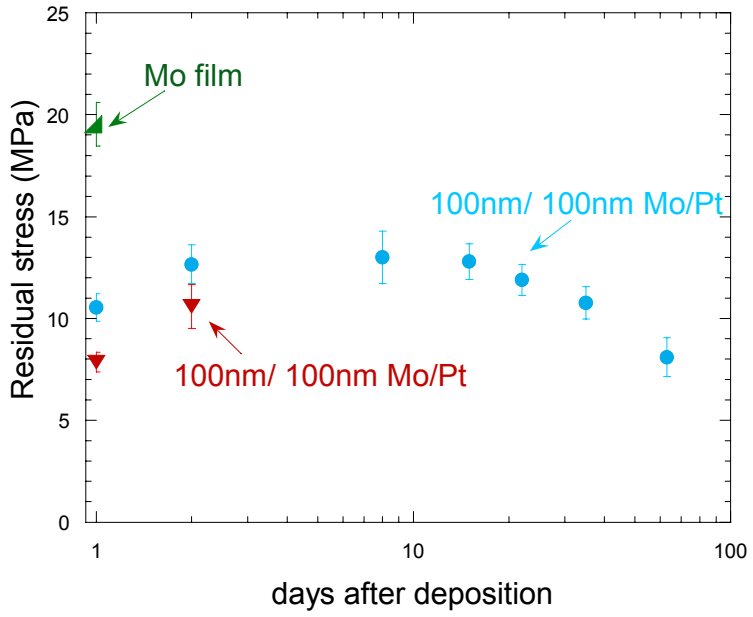


**Figure 2.17** Evolution of the residual stress for the 100 nm/ 100 nm Mo/Pt case (2 samples were used). The stress of the Mo film on the sputtering day (day 1) is also shown in this graph for comparison

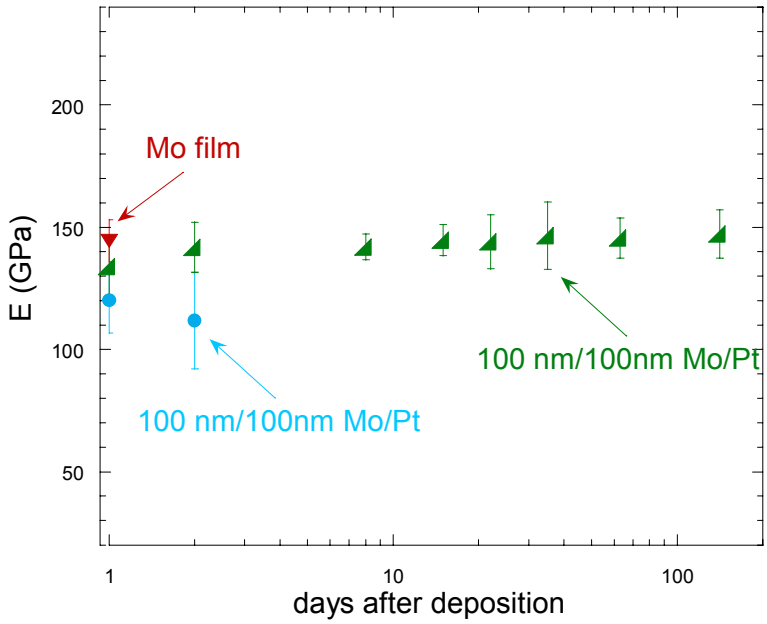


**Figure 2.18** Evolution of the elastic modulus of the 100 nm/ 100 nm Mo/Pt film with time (two samples were used). The modulus of the Mo film is also shown here for comparison. No change was detected over time

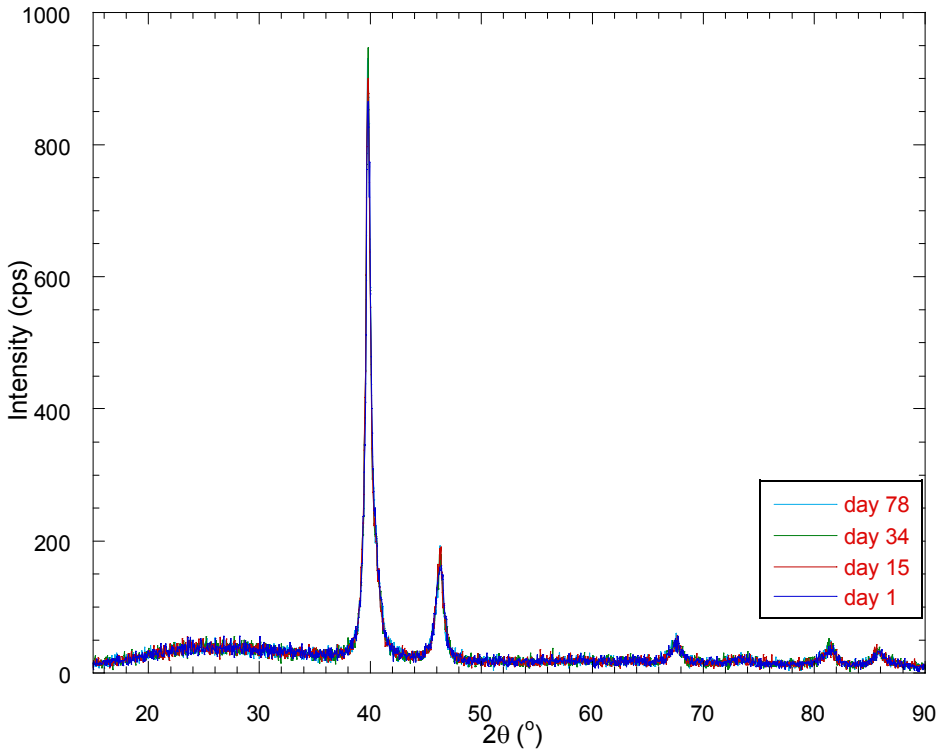


**Figure 2.19** Phase evolution of the 100 nm/ 100 nm Mo/Pt film deposited on a glass substrate with time. No molybdenum oxides were detected

The measurements of residual stress using bulge testing indirectly confirm the assumption that the oxygen content of the Mo/Pt films, and more specifically that of the Mo layers, changes with time when the films are exposed to air in ambient temperature. No other change is detected and the elastic modulus of the films as determined using both nanoindentation and bulge testing stays constant over time. Hence this post sputtering oxidation is thought to be responsible for the age hardening behavior. This conclusion is further supported by the fact that the aging of multilayers that were already annealed at 475 $^{o}$C, which caused complete oxidation of all the Mo layers (and will be discussed in more detail in Chapter 3), yields no changes in strength. The comparison between the initial hardness of the annealed samples and their hardness after 3 months of aging in ambient conditions is presented in Figure 2.20. In [2] the plastic deformation of nanoscale multilayers is considered a two step process. The first step involves the plastic deformation of the softer layers, with single dislocation loops gliding parallel to the interface (CLS model), while the second describes the slip transfer across the interface and the yielding of the hard layer. Hence the total yield strength of the composite is determined by the stress necessary to cause dislocation glide within the soft layer, which depends on layer thickness, and the additional stress needed for dislocation transmission in the hard layer. For the Pt-based nanocomposites studied here, Pt is the soft layer where dislocations initially glide and get pinned by the Mo/Pt incoherent interface. The increase in strength after aging in ambient conditions can be explained by the formation of Mo oxides at the Mo/Pt interface. The precipitates at the interface can act as obstacles to dislocation motion and inhibit dislocation transmission across the interface, in the manner described by the Orowan type

strengthening mechanism. In this case the third term in equation (2.3) becomes more general to describe the effect that both misfit dislocations and precipitates, present at the interface, have on dislocation glide within the soft layer. This term then represents the stress opposing dislocation glide originating from obstacles at the interface, where λ now is the separation distance of these obstacles.

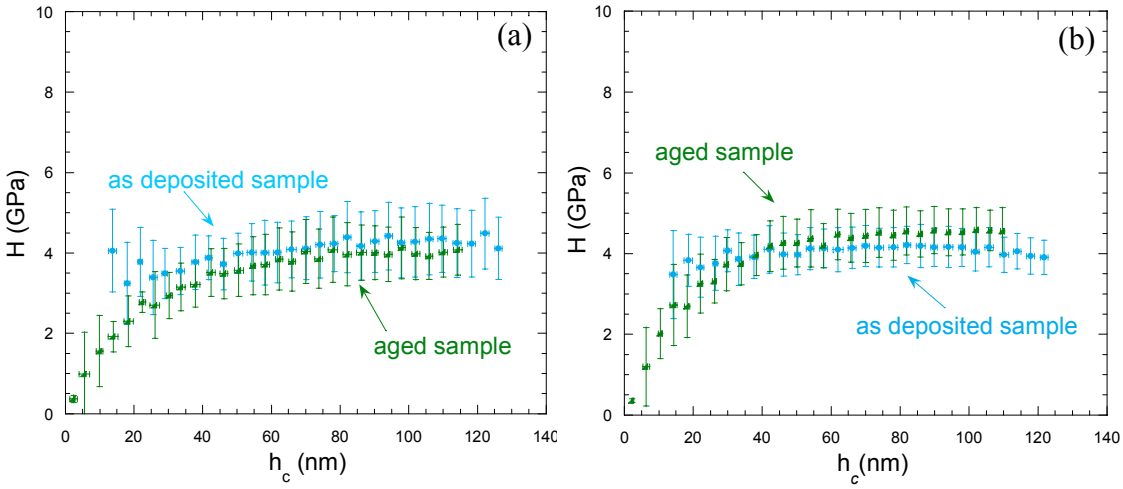


**Figure 2.20** No changes in the hardness of annealed Mo/Pt films is detected with aging time. **(a)** 25 nm/ 30 nm annealed film **(b)** 60 nm/ 35 nm annealed film

It should be noted here that attempts to make the 100 nm/100 nm membranes free standing by removing the $Si/SiO_2$ backing substrate by reactive ion etching were unsuccessful. After the ion etching cycle was complete no film was left over the window. In order to verify that the destruction of the film was the result of the residual stress in the film and not of the etching process, a Mo/Pt membrane was covered by photoresist before RIE. The idea was that this film would act as a protective layer. Once the etching was complete and the backing substrate was removed the effect of compressive stresses on the film was apparent (Figure 2.21 (a)). Upon removal of the photoresist by floating the film in

acetone the free standing membrane was completely destroyed (Figure 2.21 (b)). Using this procedure it was once more confirmed that compressive residual stresses are present in the as deposited multilayers and it was shown that these stresses prevent the fabrication of free standing membranes.

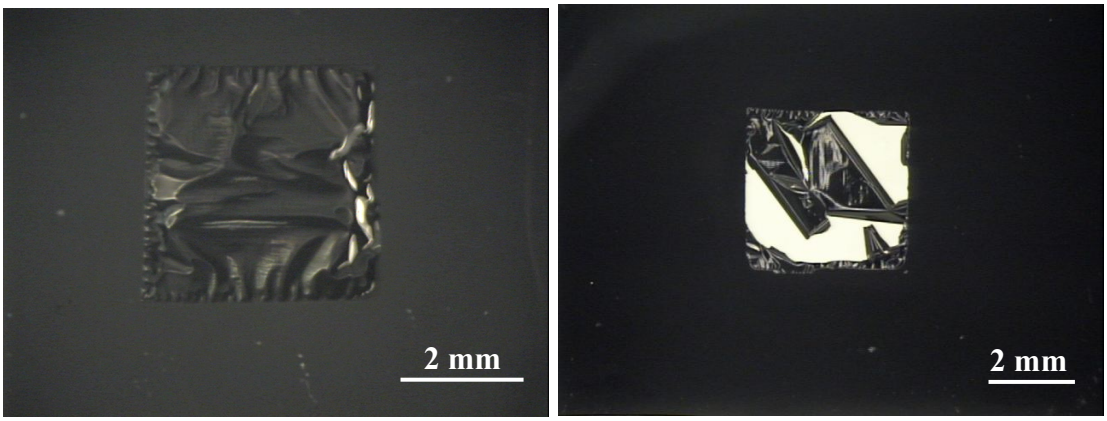


**Figure 2.21 (a)** The 100 nm/ 100 nm Mo/Pt film was made free standing by using reactive ion etching to remove the 2.5 μm of $Si/SiO_2$ substrate. The surface of the sample was covered with photoresist (total thickness of 1 μm) to protect the film during the etching process. The buckles present indicate that the film is under compressive residual stresses **(b)** After removing the photoresist from the surface the free standing membrane failed

## 2.5 Summary

The mechanical properties of the Mo/Pt multilayered system were studied using two techniques, nanoindentation and bulge testing. Multilayers with different bilayer periods were studied and the hardening behavior was similar to that reported for other fcc-bcc systems which form incoherent interfaces. For the layer thicknesses used in this study the confined layer slip model (CLS) seems to describe well the strengthening behavior of the

nanocomposites. It was also shown that when the thickness of the Pt layer, the soft layer for this system, was kept the same (at approximately 100 nm) the hardness did not change significantly despite the different thicknesses of the Mo layer. This result indicates the importance of the soft layer, at the length scales investigated here, in determining the overall strengthening behavior of the nanostructure. Another observation of this study was the increase in the hardness of the films after aging in ambient conditions. The combination of the results of X-ray Photoelectron Spectroscopy with the evolution of residual stresses in the nanolayered films, acquired using the bulge testing technique, pointed to O incorporation as responsible for the aging behavior. Mo oxides that form at the Mo/Pt interface act as obstacles to dislocation glide, in the manner described by the Orowan strengthening mechanism, increasing the strength of the aged samples. The fact that no increase in strength was observed after the aging of annealed samples, where complete oxidation of all the Mo layers occurred upon annealing, further verified the assumption that post sputtering deposition is responsible for the aging behavior.

## 2.6 References

**[1]** "Attempt to design a strong solid" J. S. Koehler, Phys. Rev. B **2** 547 (1970)

**[2]** "Single-dislocation-based strengthening mechanisms in nanoscale metallic multilayers" A. Misra, J. P. Hirth and H. Kung, Phil. Mag. A **82** 2935 (2002)

**[3]** "Deformation and fracture in microlaminates" G. S. Was and T. Foecke, Thin Solid Films **286** 1 (1996)

**[4]** "Deformation behavior of nanostructured metallic multilayers" A. Misra and H. Kung, Advd Engng Mater. **3** 217 (2001)

**[5]** "Length-scale-dependent deformation mechanisms in incoherent metallic multilayered composites" A. Misra, J. P. Hirth and R. G. Hoagland, Acta Mater. **53** 4817 (2005)

**[6]** "Introduction to Dislocations", D. Hull, D. J. Bacon, Butterworth-Heinemann (2001)

**[7] "**The cleavage strength of polycrystals" N. J. Petch, J. Iron Steel Inst. **174** 25 (1953)

**[8]** "Deformation mechanism maps for polycrystalline metallic multilayers" A. Misra, M. Verdier, H. Kung, J. D. Embury, J. P. Hirth, Scripta Mater. **41** 973 (1999)

**[9]** "Dislocation Analysis of Crack Lamellae" M. J. Marcinkowski, R. W. Armstrong, J. Appl. Phys. **43** 2548 (1972)

**[10]** "The Limiting Grain Size Dependence of the Strength of a Polycrystalline Aggregate," R. W. Armstrong, Y. T. Chou, R. M. Fisher, N. Louat, Phil. Mag. **14** 943 (1966)

**[11]** " Circular dislocation pile-ups" J. C. M. Li, G. C. T. Liu, Phil. Mag. **15** 1059 (1967)

**[12]** "Critical layer thickness for misfit dislocation stability in multilayer structures" J. P. Hirth, X. Feng, J. Appl. Phys. **67** 3343 (1990)

**[13]** "Slip resistance of interfaces and the strength of metallic multilayer composites" R. G. Hoagland. R. J. Kurtz, C. H. Henager, Sripta Mater. **50** 775 (2004)

**[14]** "Simple model for interface stresses with application to misfit dislocation generation in epitaxial thin films" R.C. Cammarata, K. Sieradzki, F. Spaepen, J. Appl. Phys. **87** 1227 (2000)

**[15]** "On the strengthening effects of interfaces in multilayer fcc metallic composites" R. G. Hoagland, T. E. Mitchell, J. P. Hirth, H. Kung, Phil. Mag. A **82** 643 (2002)

**[16]** "Dislocation-based deformation mechanisms in metallic nanolaminates" P. M. Anderson, T. Foecke, P.M. Hazzledine, Mater. Res. Soc. Bull. **24** 27 (1999)

**[17]** "Structure and mechanical properties of Cu-X (X=Nd, Cr, Ni) nanolayered composites" A. Misra, M. Verdier, Y. C. Lu, H. Kung, T. E. Mitchell, M. Nastasi and J. D. Embury, Scripta Mater. **39** 555 (1998)

**[18]** "Tensile properties of nanostructured Ni-Cu multilayered materials prepared by electrodeposition" D. M. Tench, J. T. White, J. Electrochem. Soc. **138** 3757 (1991)

**[19]** "Microstructures and strength of nanoscale Cu-Ag multilayers" J. McKeown, A. Misra, H. Kung, R. G. Hoagland and M. Nastasi, Scripta Mater. **46** 593 (2002)

**[20]** "Structure and Strength of Multilayers" B. M. Clemens, H. Kung, S. A. Barnett, Mater. Res. Soc. Bull. **24** 20 (1999)

**[21]** " Model of superlattice yield stress and hardness enhancements" X. Chu and S. A. Barnett, J. Appl. Phys. **77** 4403 (1995)

**[22]** " The interaction of dislocations and boundaries" A.K. Head, Phil. Mag. **44** 92 (1953)

**[23]** "Materials issues in microelectromechanical systems (MEMS)" S.M. Spearing, Acta Mater. **48** 179 (2000)

**[24] "**Processing and characterization of piezoelectric materials and integration into microelectromechanical systems" D. L Polla, L. F. Francis, Annu. Rev. Mater. Sci**. 28** 563 (1998)

**[25]** " Displacement amplification in curved piezoelectric diaphragm transducers" D.J. Morris, D. F. Bahr, M.J. Anderson, Sens. Actuators A **141** 262 (2008)

**[26]** Massalski, TB (1986) Binary Alloy Phase Diagrams, American Society for Metals, Metals Park, OH

**[27]** "Mechanical behavior of Pt and Pt-Ru solid solution alloy thin films" S.Hyun, O. Kraft and R.P. Vinci, Acta Mater. **52** 4199 (2004)

**[28**] "Nanoindentation study on the mechanical properties of TiC/Mo multilayers" J. Wang, W.-Z. Li, H.-D. Li, B. Shi, J.-B. Luo, Thin Solid Films **366** 117 (2000)

**[29]** " Tensile testing on free- standing Cu, Ag, and Al thin films and Ag/Cu multilayers" H. Huang, F. Spaepen, Acta Mater. **48** 3261 (2000)

**[30]** " The influence of argon pressure on the structure of sputtered molybdenum: From porous amorphous to a new type of highly textured film" F. Klabunde, M. Lohmann, J. Blasing, T. Drusedau, J. Appl. Phys. **80** (11) 6266 (1996)

**[31]** "Effect of out-of-lane properties of a polyimide film on the stress fields in microelectronic structures" J. Dolbow, M. Gosz, Mech. Mater. **23** 311 (1996)

**[32]** D. Tabor, The Hardness of Metals, Oxford University Press (1950)

[**33**] **"**Extraction of stress-strain curves of elastic-viscoplastic soilds using conical/pyramidal indentation testing with application to polymers" G. Kermouche, J.L Loubet, J.M. Bergheau, Mech. Mater. **40** 272 (2008)

**[34] "**Photoemission study of the electronic structure of Mo and Mo oxides" F. Werfel, E. Minni, J Phys C: Solid State Phys **16** 6091 (1983)

**[35] "**An ESCA study of the termination of the passivation of elemental metals" T.L. Barr, J. Phys. Chem. **82** 1801 (1978)

**[36] "**The role of impurities and microstructure on residual stress in nanoscale Mo films" L.P. Kendig, U. Z.U. Rek, S.M. Yalisove, J.C. Bilello, Surface and Coatings Technology **132** 124 (2000)

**[37]** " Stress and microstructure in tungsten sputtered thin films" A. M. Haghiri-Gosnet, F. R. Ladan, C. Mayeux, H. Launois, M. C. Joncour, J. Vac. Sci. Technol. A **7**(4) 2663 (1989)

**[38] "**Stress, microstructure, and stability of Mo/Si, W/Si, and Mo/C multilayer films" David L. Windt, J. Vac. Sci. Technol. A **18** 980 (2000)

**[39]** " Room temperature oxidation behavior of TiN thin films" S.Logothetidis, E.I. Meletis, G. Stergioudis, A.A. Adjaottor, Thin Solid Films **338** 304 (1999)

**[40]** "Variation of internal stresses in sputtered Ta films" T. Yoshihara, K. Suzuki, J. Vac.Sci. Technol. B **11**(2) 301 (1993)

# Chapter Three: Thermal Stability of Mo/Pt multilayers

*The majority of the information in this chapter has been included in a paper accepted for publication in the Journal of Materials Science. The collection of the XPS data and the corresponding analysis were done in collaboration with Dr Louis Scudiero.*

## 3.1 Introduction

Composite structures that consist of two alternating thin metal layers have attracted a considerable amount of interest due to their improved mechanical properties when compared to those of their individual constituents. The layering of a soft metal with a harder one yields higher strength values than would be expected by a simple rule of mixtures, with the strength increasing as the thickness of the layers decreases [1-4]. The interface between the two metals can be either coherent or incoherent. In the first case (for example Cu-Ni) the strengthening is due in part to the elastic mismatch between the two films. In the second case (for example Cu-Nb) the interface acts as a substantial barrier to dislocation motion. For these multicomponent systems both layer thickness and interface type determine the overall mechanical behavior, with incoherent interfaces generally yielding at higher strength values than the coherent case.

The mechanical properties of multilayered structures have been primarily investigated at room temperature. However some potential applications involve high temperature or oxidizing environments and thermal excursions, which make the long term stability an important issue. The composite with improved mechanical properties must maintain its strength at high temperatures in order to be a viable candidate for these conditions. Studies of nanolayered systems have shown that stability at high temperatures can be a concern [5, 6]. For instance, annealing Ta/Cu films at temperatures ranging from 400 to 800 $^{o}$C showed complete disintegration of the layered structure at 800 $^{o}$C [5], with a final microstructure of equiaxed Cu and Ta grains. Experiments on the thermal stability of Cu/Nb films with layer thicknesses of 15, 35 and 75 nm at temperatures up to 800 $^{o}$C for times reaching 60 h, showed that the nanostructures with thicknesses of 35 and 75 nm were stabilized by the alignment of triple point junctions in a zig zag pattern [6]. This alignment seemed to protect the structure from layer pinch off and subsequent spheroidization. Hence the composites maintained most of their strength with the 75 nm thickness being stable even after 60 h at 700 $^{o}$C. Although realignment of the grain boundaries did occur in the 15 nm thick layers it didn't effectively stabilize the structure. In the thinnest films at 700 $^{o}$C even short annealing times (30 min) caused the loss of the layered structure which resulted in a significant decrease of the film hardness. This demonstrates that maintaining the layered structure at high temperatures is crucial in retaining the high strength of the nanocomposite.

While many multilayer studies have focused on Cu as the FCC metal [7-9], it is not the only FCC metal of interest in thin film applications. Pt is used in applications as an

electrode for high temperature oxidizing conditions. For instance, Pt electrodes are commonly used for fabricating piezoelectric $Pb(Zr_xTi_{1-x})O_3$ films [10]. Piezoelectric films in membrane form can be used as MEMS acoustic transducers, and they exhibit enhanced performance when operated at high strains [11]. Silicon (Si) is commonly added as a support layer which helps the membrane withstand high pressures. At high strains the support layer doesn't add to the efficiency of the device so there is interest in removing it from the structure. In this case the bottom electrode could act both as the electrical component and the support layer of the piezoelectric actuator. However, Pt develops high residual tensile stresses after deposition and subsequent MEMS processing, and is generally not a suitable free standing film for thin membranes. Layering of Pt with another metal could improve the mechanical properties of the film and allow fabrication of free standing membranes.

In the current study molybdenum (Mo) was chosen as the second metal to be used with Pt in multilayered structures. Mo forms an incoherent interface with the Pt layer, and thus should result in high strength films. Additionally, Mo has some solid solubility in Pt and does form intermetallic phases with Pt, and as such is representative of many of the bcc metals with Pt. Mo/Pt multilayers with a number of different thickness combinations were sputtered and their strength was evaluated using nanoindentation. In each case the strength of the composite was higher than that of the Pt film alone making these nanolayered structures attractive for MEMS applications. Since piezoelectric MEMS processing often involves high temperature annealing in air [10] the thermal stability and oxidation of these

composites is an important issue in addition to problems such as the pinching off of layers and grain coarsening already reported for other multilayered systems [5, 6].

In order to study the thermal stability of the Mo/Pt system and investigate the changes in the strength for films with different bilayer periods all structures were annealed at 475 $^{o}$C for 1 h. The strength of the composites was determined using nanoindentation and the resulting microstructures were studied by Scanning Electron Microscopy (SEM). Bulk and surface chemical compositions were investigated by X-ray Diffraction (XRD) and X-ray Photoelectron Spectroscopy (XPS). Chemical bonding information was obtained by XPS. The use of these complementary techniques allowed a correlation between the observed microstructure, chemical properties and the measured hardness of the annealed samples.

## 3.2 Experimental details

The nanolayered films used in this study were deposited by sequential DC magnetron sputtering at nominally room temperature. Films with 4, 10 and 20 layers were sputtered on Si wafers. The wafers were thermally oxidized forming a $SiO_2$ layer approximately 120 nm thick. The Mo layer was always the first layer in the sequence directly sputtered on the oxide, with Pt being the last layer of the nanocomposite. The thicknesses of the nanolayered structures used in this study are shown in Table 3.1. The background pressure in the chamber prior to sputtering was $1 \cdot 10^{-6}$ Torr. All Mo layers were sputtered at a regulated power of 200 W and an Ar pressure of 3.8 mTorr while the Pt layers were sputtered at a regulated power of 60 W and an Ar pressure of 11 mTorr. The

deposition rate for each metal was kept constant for all different composites and different layer thicknesses were obtained by accordingly varying the deposition time. In addition to the Mo/Pt multilayers that were deposited on Si wafers, films with the same bilayer period as samples 2 and 6 were also sputtered on glass substrates. The use of glass substrates allowed the acquisition of X-ray diffraction patterns from the films without the contribution of Si to the pattern. A Siemens D-500 X-ray powder diffractometer with a Cu X-ray tube was used to collect the diffraction data.

Films with the same bilayer period as samples 2 and 6 were also sputtered on $Si/SiO_2$ windows which were fabricated using standard photolithography techniques. The $Si/SiO_2$ backing substrate had a thickness of approximately 2.5 μm. These membranes were used to evaluate the residual stress in the as deposited and annealed case using the bulge testing technique [12, 13]. The presence of compressive residual stresses in the as deposited films caused sample 2 to buckle after deposition, so only results for the 100 nm/ 100 nm Mo/Pt film, as measured before and after annealing, are reported.

The thermal annealing of the various films was done in a Lindberg 1800 $^{o}$C box furnace in air. The samples were heated at a rate of 8 $^{o}$C/ min to 475 $^{o}$C and held at temperature for 1 h. The samples were then furnace cooled to room temperature. Both films deposited on Si wafers and glass substrates were thermally treated following this procedure.

Cross sections of the as deposited and annealed films obtained by cleavage were studied using a FEI Sirion 200 Scanning Electron Microscope. The individual layer and

total thicknesses of the multilayers were determined by the Scanning Electron Microscope micrographs.

The actual layer thicknesses are reported in Table 3.1 along with the nominal values. The mechanical properties of the as deposited and annealed films were measured using a Hysitron Triboscope with the nanoDMA$^{TM}$ attachment. Using this attachment the contact stiffness at various points during loading was recorded, which allowed the measurement of modulus and hardness as a function of penetration depth for any given indentation. A calibrated Berkovich tip was used for the indentation. The hardness values presented in this paper are averaged values which correspond to contact depths approximately equal to 10 % of the total film thickness. This choice of contact depth minimizes the influence of the substrate on the measured values, but at the same time is deep enough to minimize any effects from surface roughness. Each sample was indented at least 5 times and 80 measurements per indent were collected. The values of hardness and modulus presented in this study are averages of these nanoindentation measurements.

The XPS spectra of the 100 nm/100 nm Mo/Pt films were obtained with an AXIS-165 manufactured by Kratos Analytical Inc. using an achromatic MgKα (1254 eV) X-ray radiation with a power of 210 W. The spectrometer was calibrated against both the Au 4f $_{7/2}$ peak at 84.2 eV and the Ag $3d_{5/2}$ peak at 368.5 eV. Curve fitting of the XPS peaks was performed with the commercial CasaXPS software using Gaussian/Lorentzian line shape. The chemistry of the film was sampled by depth profiling. $Ar^+$ sputtering at 4keV combined with XPS provided a way to analyze the first two layers of the multilayer sample under two conditions (as deposited and annealed in air at 475 °C). In addition, XPS spectra

of clean Mo and Pt were acquired for films prepared under the same sputtering conditions as the corresponding layers of the multilayer films. These spectra were used as reference for the binding energies of Mo and Pt.

**Table 3.1** Specimens used in this study. Both nominal and actual layer thicknesses are reported

| Sample # | Nominal layer thickness (Mo/Pt) | Measured Layer thickness (Mo/Pt) | Total Film Thickness |
|---|---|---|---|
| 1 (20 layers) | 20 nm/20 nm | 18 nm/21 nm | 430 nm |
| 2 (20 layers) | 25 nm/30 nm | 25 nm/29 nm | 590 nm |
| 3 (10 layers) | 60 nm/ 35 nm | 61 nm/35 nm | 503 nm |
| 4 (4 layers) | 35 nm/ 100 nm | 33 nm/94 nm | 252 nm |
| 5 (4 layers) | 55 nm/100 nm | 55 nm/107 nm | 336 nm |
| 6 (4 layers) | 100 nm/100 nm | 93 nm/102 nm | 391 nm |

## 3.3 Results and Discussion

A typical micrograph from the surface of the as deposited films can be seen in Figure 3.1. The grains appear faceted and some voiding is present along the grain boundaries. The grain size ranged from 10 to 30 nm. The grain sizes for the as deposited films were similar in all cases regardless of layer or total thickness. Representative cross sections of the as deposited films can be seen in Figure 3.2 and 3.3. The growth residual

stress of the as deposited 100 nm/ 100 nm Mo/Pt film was a compressive stress of 10.5 ± 0.7 MPa measured using bulge testing.

The hardness values as determined using nanoindentation are presented in Table 3.2. These averages correspond to a contact depth approximately equal to 10% of the film thickness. It is apparent from these values that the thinner Pt layers provide higher strength composites, which is in accordance with results for other systems where the strength increases as the layer thickness decreases [1].

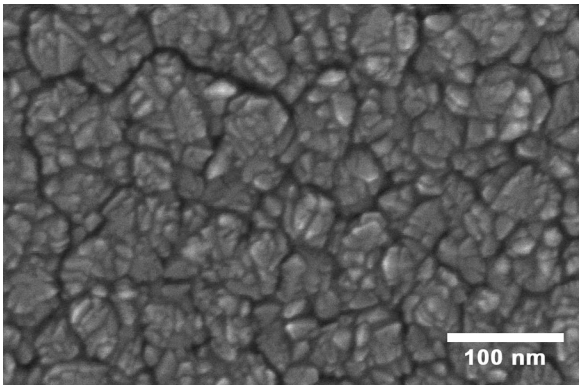


**Figure 3.1** Top view of the 35 nm/ 100 nm Mo/Pt film. The in plane grain size of Pt is very small and some voiding can be seen along the grain boundaries

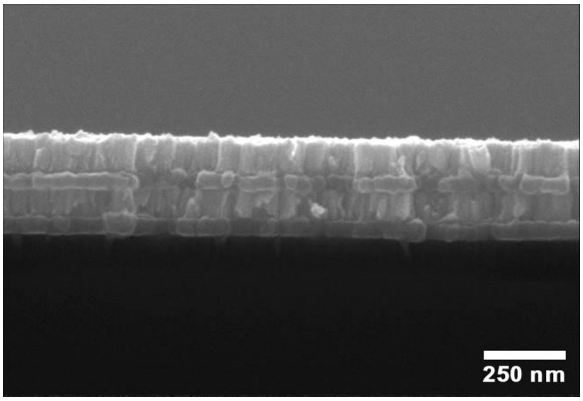


**Figure 3.2** Representative cross section of the 55 nm/ 100 nm Mo/Pt film. The lighter contrast layers with the distinct columnar structure of the grains are Pt layers

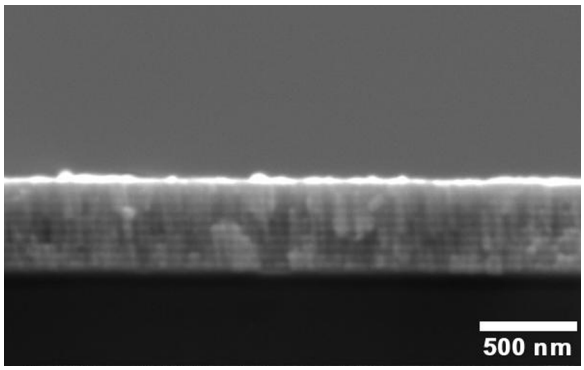


**Figure 3.3** Typical cross sectional area of structure with 20 layers. The nominal layer thickness is 25 nm/ 30 nm Mo/Pt

**Table 3.2** Comparison of hardness values for all films before and after annealing

| **Nominal Layered Film (Mo/Pt)** | **H (GPa)** | **H (GPa) annealed** | **% decrease in strength after annealing** |
|---|---|---|---|
| 20 nm/20 nm | $6.62 \pm 0.26$ | $4.17 \pm 0.19$ | 37 |
| 25 nm/30 nm | $6.29 \pm 0.29$ | $3.71 \pm 0.75$ | 41 |
| 60 nm/ 35 nm | $5.85 \pm 0.52$ | $4.37 \pm 0.71$ | 25 |
| 35 nm/ 100 nm | $3.67 \pm 0.41$ | $2.87 \pm 0.49$ | 22 |
| 55 nm/100 nm | $3.8 \pm 0.45$ | $3.36 \pm 0.52$ | 12 |
| 100 nm/100 nm | $4.29 \pm 0.30$ | $3.32 \pm 0.40$ | 23 |
| 200 nm Pt (single layer) | - | $2.63 \pm 0.45$ | - |

The phase diagram of Mo-Pt shows that there is solubility over a significant range of compositions and exhibits a number of different intermetallics [14]. The study of annealed samples was necessary in order to determine whether the layered structure of the nanocomposites is maintained, if any intermetallics formed during the thermal processing, and how these microstructural changes affected the strength of the resulting films. For this reason the as deposited films were annealed in air at 475 $^{o}$C for 1 h.

After annealing the residual stress of the 100 nm/ 100nm film became tensile and a value of 38.4 ± 1.6 MPa was measured using bulge testing. The relatively small difference in the values of the net residual stress for the same film before and after annealing indicates that the net stress of the multilayers may not be an important factor in the overall behavior of the films with the stresses in the individual layers possibly playing a more important part.

The modulus and hardness of the annealed films as a function of contact depth were again measured using nanoindentation and the corresponding values of hardness are presented in Table 3.2. In all cases the strength of the annealed films was lower than what was determined for the as deposited case; with the decrease being more significant for the thinner Pt layers. Despite this decrease the hardness of all annealed films was still higher than that of 200 nm Pt films annealed at the same temperature (2.63 GPa). Comparison between the hardness versus contact depth for the as deposited and annealed case can be seen in Figure 3.4 for two of the samples used in this study. In order to explain the strength loss and the difference in behavior between thinner and thicker layers the microstructure of the annealed films was studied using the SEM.

In Figure 3.5a and 5b the top view and cross section of the annealed 55 nm/100 nm Mo/Pt film are shown. After the heat treatment the slightly voided boundaries open significantly, forming cracks along the Pt grain boundaries. In Figure 3.6 an SEM micrograph from a tilted annealed sample is shown. From this image it can be seen that the cracks which formed after annealing extend in a significant depth of the film reaching at least up to the first interface between Mo and Pt. The in plane grain size is larger than what was observed for the as deposited films, ranging from 20 to 50 nm. This grain coarsening can be responsible for the observed decrease in strength. Comparing the cross section of the as deposited sample (Figure 3.2) to the one after annealing (Figure 3.5b) it is apparent that a significant change in the microstructure has occurred. Although after the heat treatment the layering of the composite was maintained, the thickness of all the Mo layers has significantly increased. This increase in the thickness of the Mo layers was typical for all structures with the thicker Pt layers namely samples 4, 5 and 6. A possible explanation for the increase in thickness is the oxidation of Mo. Mo oxides have lower densities than Mo, and hence a significant increase in volume is observed during oxidation [15]. This volume expansion likely causes the observed cracking along the grain boundaries. Although for these multilayered structure Pt as the top layer is directly in contact with air, diffusion of oxygen can occur along the Pt grain boundaries causing oxidation of the underlying Mo layers. It is probable that oxygen diffusion is further enhanced by the crack formation. X-ray Photoelectron Spectroscopy and X-ray Diffraction were used to verify that oxidation is responsible for the apparent changes in microstructure.

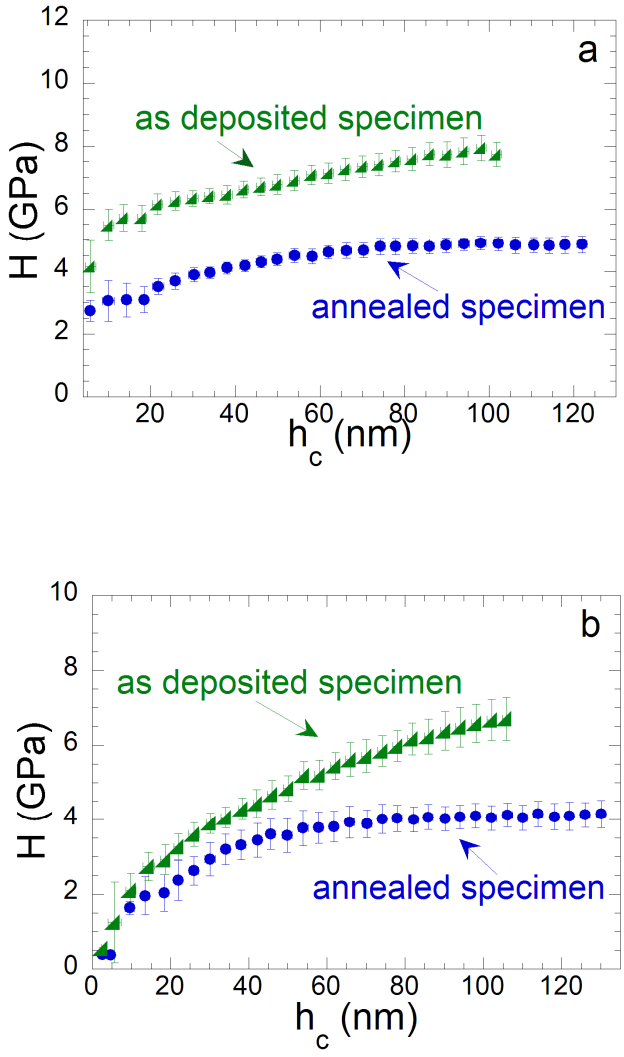


**Figure 3.4** Representative curves of hardness versus contact depth for as deposited and annealed samples. In both **(a)** ( 20 nm/ 20 nm Mo/Pt) and **(b)** (100 nm/100 nm MoPt film) the hardness values for the annealed composites are lower than the corresponding values in the as deposited case

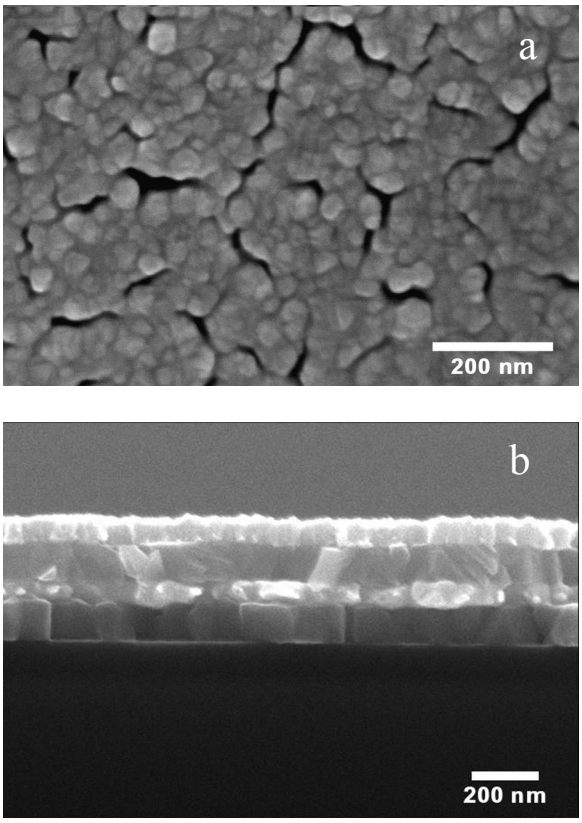


**Figure 3.5 (a)**Typical top view of the film surface for annealed samples with thicker layers. Cracking along the grain boundaries is present. **(b)** Cross section of the 55 nm/ 100 nm Mo/Pt film after annealing at 475 $^{o}$C for an hour. The thickness of the Mo layers (darker contrast) considerably increased during annealing compared to the initial thickness (Figure 3.2)

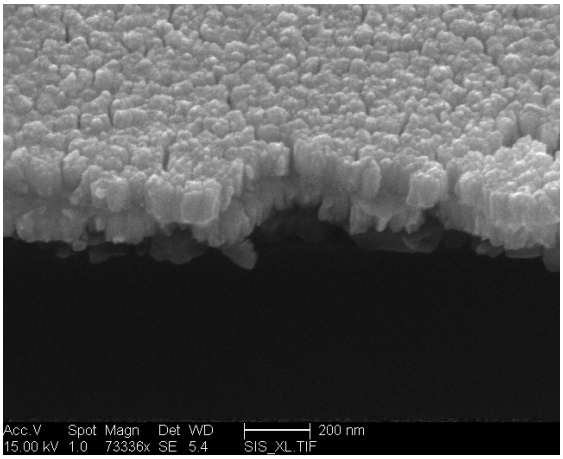


**Figure 3.6** SEM micrograph of the tilted 35 nm/ 100 nm Mo/Pt film. The voided boundaries seen on the top view see to extend up to the first interface between Pt and Mo

Figure 3.7 shows the Pt 4f and Mo 3d spectra. Both reference spectra of Pt 4f and Mo 3d and spectra obtained at sputtering times of about 3400s and 11400s from the annealed 100 nm/ 100 nm Mo/Pt film are shown for comparison. The Pt 4f spectrum (Figure 3.7a) acquired after 3400s of Ar sputtering (Pt layer) shows no peak shift. Pt appears in its elemental metallic form, $Pt^0$, which indicates that no Pt/Mo intermetallics formed during the annealing process. Figure 3.7b shows XPS spectra of Mo 3*d* from the reference Mo film, the as deposited and the annealed 100 nm/ 100 nm Mo/Pt multilayer after 11400s of Ar sputtering. The spectra for the reference film and the as deposited nanocomposite film exhibit similar Mo species. The main peak at a binding energy of (BE) = 228.1 ± 0.1 eV is assigned to elemental $Mo^0$, in good agreement with literature values [16, 17]. A weak peak at BE = 229.4 eV is assigned to $Mo^{4+}$ due to oxygen present in the film. This peak is associated with $MoO_2$. The XPS spectrum of Mo for the annealed sample after 11400s of Ar sputtering displays at least two Mo oxide species. Deconvolution of the 3d doublet reveals the existence of Mo dioxide ($Mo^{4+}$) and trioxide species ($Mo^{6+}$). No pure Mo peak is identified in the annealed sample. An XPS survey of the sample well within the Mo layer confirms the presence of a large amount of oxygen (~ 52 At%) in agreement with the findings of the peak deconvolution. The values for the binding energies and the oxides associated with each peak are presented in Table 3.3, and show that annealing the multilayered film led to the complete oxidation of Mo to form $MoO_2$, $Mo_x(OH)_y$ and $MoO_3$ while no Mo-Pt intermetallics formed. Using the amount of hydroxide obtained from the O 1s peak (not shown) the value of x and y were determined to be close to 1:1, respectively. Any intermetallics which formed during annealing would have resulted in a BE shift of 0.3

to 0.9 eV of the metallic main peak ($Mo^0$), as shown by Jaksic et al. in their work on Mo-Pt alloying [19]. No such energy shift was measured for our sample.

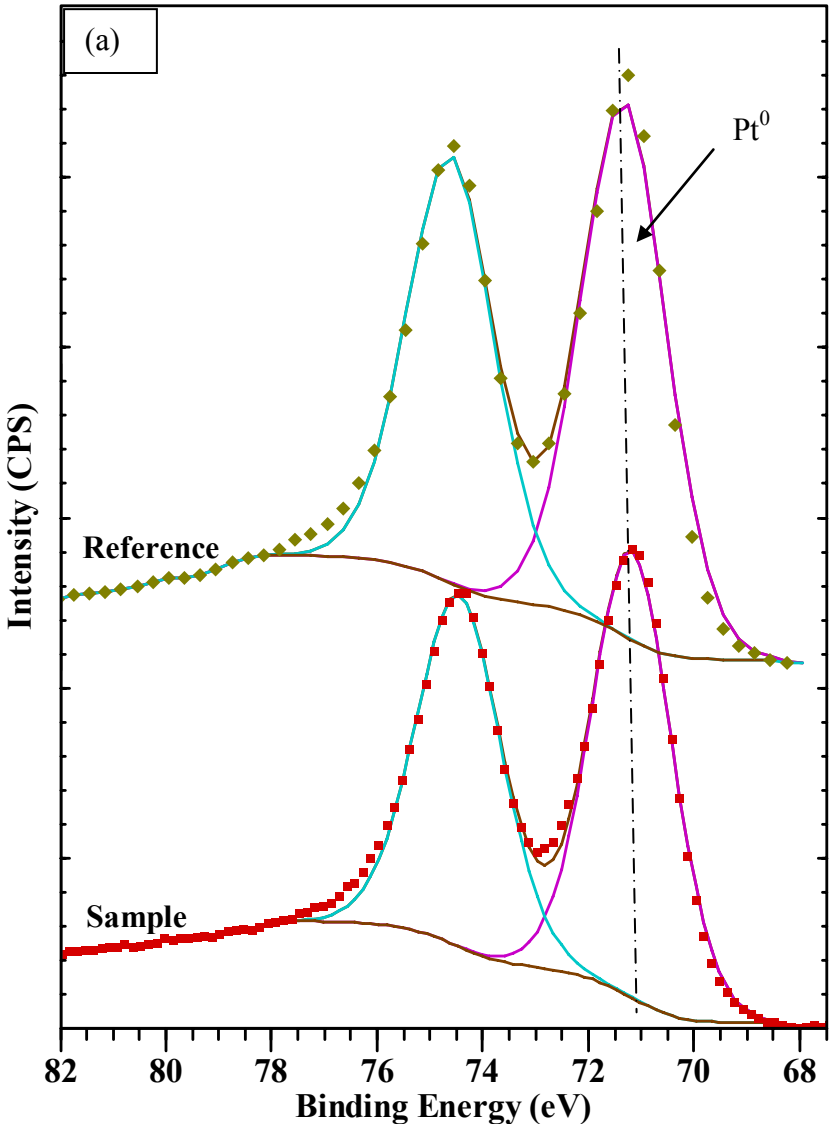

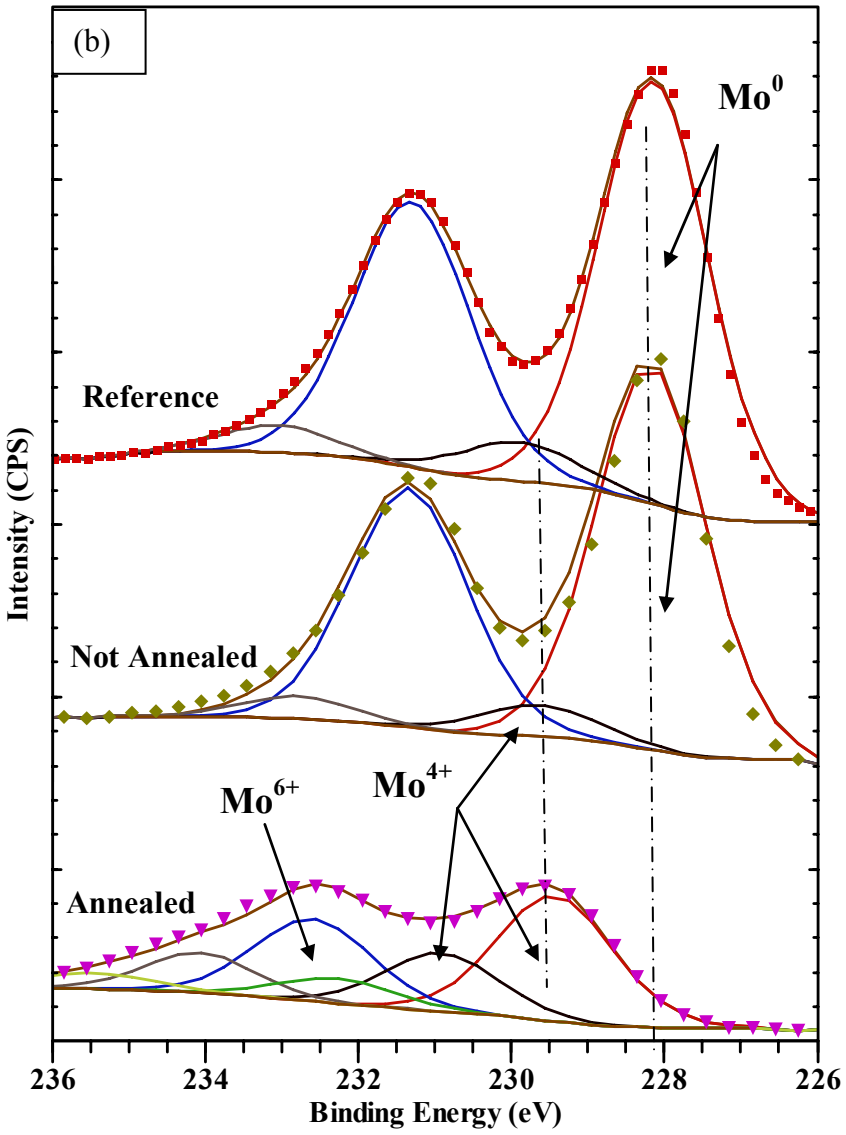


**Figure 3.7** Spectra obtained from XPS of the 100 nm/ 100 nm Mo/Pt film. **(a)** Pt 4f XPS spectra. No shift was observed between the reference (top spectrum) and the spectrum obtained after about 3400s of $Ar^+$ sputtering of the annealed film (Pt layer) . **(b)** Mo 3d spectrum from the reference film and peaks obtained before and after annealing of the composite at about 11400s of Ar sputtering (Mo layer)

**Table 3.3** Binding energies and most probable oxidation states of Mo in annealed Pt/Mo multilayers

| Peak | Binding Energy of the $3d_{5/2}$ peak (eV) | Oxidation state of Mo |
|---|---|---|
| 1 | 228.1 | $Mo^{0}$ [16, 17] |
| 2 | 229.4 | $Mo^{+4}$ [17] |
| 3 | 231.0 | $Mo^{+4}$ [18] due to OH |
| 4 | 232.3 | $Mo^{+6}$ [18] |

Since XPS was only used to probe the first Mo layer (second layer in the stacking sequence) and identify the different oxidation states of Mo, X-ray diffraction was further utilized to verify that complete oxidation of all the Mo layers has occurred. X-ray diffraction patterns collected from the annealed 100 nm/ 100 nm Mo/Pt film deposited on a glass substrate can be seen in Fig. 3.8. In addition to peaks corresponding to Pt, Mo oxide peaks were clearly identified, whereas no peaks corresponding to pure Mo were present. These results combined with the apparent increase in the thickness of all the Mo layers in the annealed structures suggest that complete oxidation of the Mo layers has occurred upon annealing.

Annealing structures with thinner Pt layers resulted in somewhat different microstructures than the ones described for those with the thickest Pt layers (100nm).Top view and cross sectional micrographs for the case of the 25 nm/30 nm Mo/Pt film are shown in Figure 3.9. The micrographs presented here are typical for all structures with Pt layers thinner than 35 nm layers (samples 1-3). As was previously observed for structures

with thicker layers (Figure 3.5b) the thickness of the Mo layers has significantly increased after annealing (Figure 3.9b) compared to the as deposited case (Figure 3.3). This behavior is again indicative of oxidation during the thermal treatment. However in this case the layered structure was not maintained, with Pt appearing in the form of isolated islands rather than layers. The loss of the continuous interface is likely responsible for the significant decrease in strength recorded for all structures with thinner layers and presented in Table 3.2.

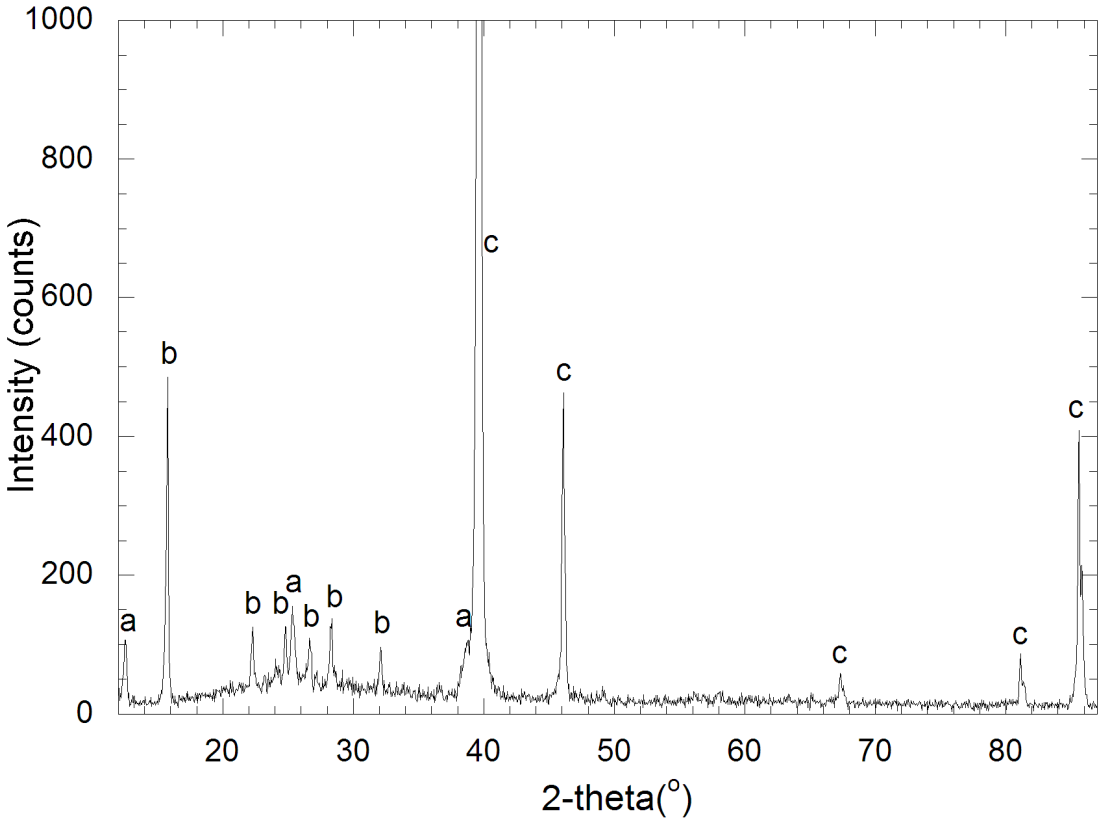


**Figure 3.8** X-ray diffraction pattern for the 100 nm/ 100 nm Mo/Pt film annealed at 475 °C for 1 h. a denotes the peaks assigned to $MoO_3$ (pdf #005-0508), b corresponds to the $Mo_{17}O_{47}$ peaks (pdf #013-0345) and c marks the positions of the Pt diffraction peaks (pdf #004-0802)

The top view of the annealed sample (Figure 3.9(a)) also demonstrates a feature that indicates the importance of oxidation in this system. In addition to cracking that was also observed for the 4 layer films, white faceted platelets are present on the sample surface. These faceted platelets have similar appearance to $MoO_3$ platelets that form during oxidation of Mo. A study of the oxidation of Mo silicides in air [20] showed that at 600 $^oC$ the sample surface was covered by white powder and XRD identified $MoO_3$ as the primary phase. In this work, annealing at 800 $^oC$ caused complete volatilization of the $MoO_3$ phase which was deposited on areas of lower temperature in the reaction chamber in the form of spikes. The volatile nature of molybdenum trioxide has been utilized in the synthesis of $MoO_3$ whiskers by oxidation of Mo in an oxygen atmosphere where the temperature in the furnace reached 900 $^oC$ [21]. Although in both these papers volatilization seems to occur at higher temperatures than the one used here, in [22] partial vaporization of the forming oxide was reported for temperatures between 550 $^oC$ to 700 $^oC$. These observations in literature over a wide range of oxygen pressures, combined with the fact that the formation of molybdenum trioxide is an exothermic reaction that releases significant amounts of heat [20, 22] make the volatilization of $MoO_3$ a mechanism that could operate even at the moderate annealing temperature of 475 $^oC$ used in this study. This could also explain how oxide platelets appeared on the surface of the film despite the fact that Pt is the layer in direct contact with air. Diffusion of oxygen along the Pt grain boundaries caused the formation of various Mo oxides and a significant increase in volume. The heat released by the oxidation process locally increased the temperature, allowing the vaporization of molybdenum trioxide. The cracking that occurred along the grain boundaries in the case of

thin Pt layers along with the loss of the continuous interface between the two metals exposed the Mo layers and allowed $MoO_3$ vapors to escape from the film. Condensation of the oxide vapors is expected on areas of lower temperatures (which can either be the surface of the sample or other areas inside the furnace). If this is the case, material loss from the film would be observed. This material loss was indeed observed for the 25 nm/ 30 nm Mo/Pt film deposited on the glass substrate. Before the thermal treatment at 475 $^{o}$C the surface of the film was reflective and no cracks could be seen macroscopically. However after annealing of the film macroscopic cracks which exposed the glass substrate were present indicative of significant material loss. The difference in the sample appearance between the multilayers with thicker (100 nm) and thinner (30 nm) Pt layers, after annealing at 475 $^{o}$C is apparent (Fig 3.10). Both films shown were deposited on glass substrates.

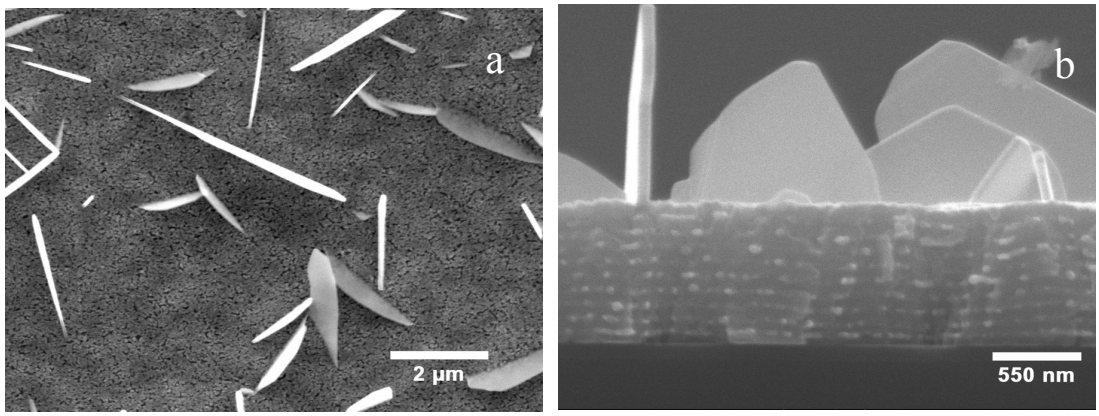


**Figure 3.9 (a)** Top view of the 25 nm/30 nm Mo/Pt film after it was annealed at 475 $^{o}$C for 1 hour. In addition to significant cracking other features are present on the surface, identified as $MoO_3$ platelets. **(b)** Cross section of the 25 nm/30 nm Mo/Pt annealed film where the disruption of the layered structure is apparent with Pt appearing in the form of islands (light contrast areas of the multilayer)

X-ray diffraction of the annealed 25 nm/30 nm Mo/Pt film that was deposited on the glass substrate, shown in Figure 3.11, confirmed the presence of Molybdenum oxides and the absence of pure Mo in the sample. Although peaks corresponding to $MoO_3$ are still present; they are not as well defined as the same peaks in the X-ray diffraction of the annealed samples with thicker Pt layers which did not undergo this platelet growth. This observation is in accordance with oxide volatilization during the annealing process once the Pt layer has lost continuity. Again the findings of the X-ray Diffraction, combined with the increase in the thickness of the Mo layers in the structures, suggest complete oxidation of all the Mo layers. The only difference from structures with thicker Pt layers is that here spheroidization of the Pt layers occurred which allowed partial volatilization of the forming oxide with subsequent growth of $MoO_3$ platelets on the surface.

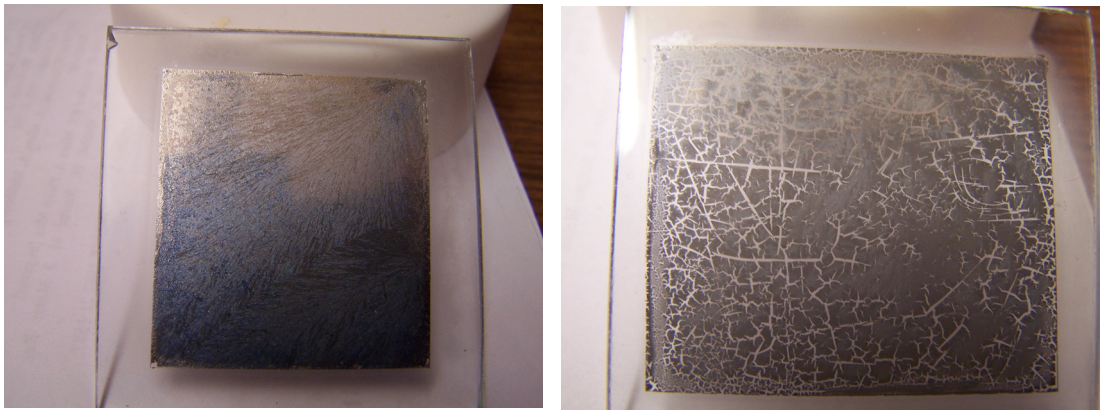

**Figure 3.10 (a)** The surface of the 100 nm/ 100 nm Mo/Pt film deposited on a glass substrate after annealing at 475 $^{o}$C for 1 h. **(b)** The surface of the 25 nm/ 30 nm Mo/Pt film were it is apparent that significant material loss has occurred. The difference from (a) is apparent

From these findings it is apparent that the annealing of the composites causes a change in microstructure which results in lower strength. The difference in the magnitude

of the strength decrease for structures with thinner and thicker Pt layers indicates that different length scales are responsible for the observed strengthening of the as deposited films. Strengthening of poycrystalline multilayers relies on two length scales of interest; layer thickness and grain size [23]. When the in plane grain size is much smaller than the layer thickness both grains and interfaces play a role in the observed behavior. The hardness in that case will show a Hall-Petch type of dependency and will be associated with pile ups at the grain boundaries and the interfaces between the two layers. In [7] it is reported that for Cu composites with layer thicknesses larger than 50 nm the Hall Petch model can explain the hardening behavior with both grain boundaries and interfaces acting as barriers to dislocation motion. However as the layer thickness becomes smaller the interfaces will dominate the mechanical behavior by confining the dislocation motion within the soft layers of the nanostructure. These mechanisms correlate well with the observed mechanical behavior of the Mo/Pt multilayers. For the composites with a Pt layer of 100 nm, both grain size and interfaces determine the overall strength. After annealing the interface is maintained, despite apparent changes in layer thickness due to oxidation, and the observed decrease in strength can be justified by grain coarsening that occurs during annealing. However for the multilayers with the smaller Pt thicknesses the interfaces dominate the strengthening behavior. The loss of the continuous interface between the Mo and the Pt layer is responsible for the large decreases in strength that cannot be justified by grain coarsening alone.

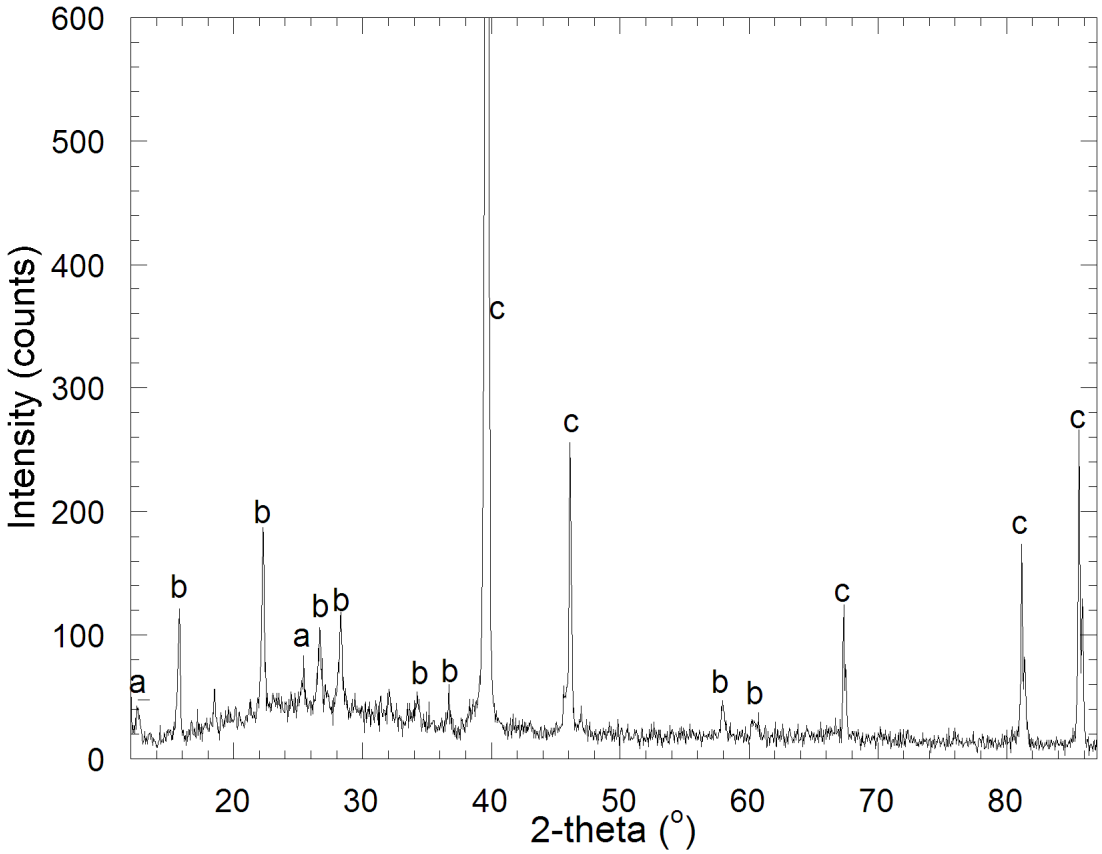


**Figure 3.11** X-ray diffraction pattern for the 25 nm/ 30 nm Mo/Pt film annealed at 475 $^{o}$C for 1 h. a denotes the peaks assigned to $MoO_3$ (pdf #005-0508), b corresponds to the $Mo_{17}O_{47}$ peaks (pdf #013-0345) and c marks the positions of the Pt diffraction peaks (pdf #004-0802)

## 3.4 Summary

Annealing of the Mo/Pt multilayer films in air at 475 $^{o}$C caused changes in the microstructure of all films, regardless of layer thickness. These changes were more significant when the Pt layers were thin, 20 to 35 nm in this study, where disruption of the layering occurred along with destructive oxidation of Mo, which involved vaporization of the forming oxide. For the 100 nm Pt thicknesses no spheroidization was observed and

although again complete oxidation of all the Mo layers occurred, the Pt layers protected Mo from destructive oxidation. A novel growth mode in the oxidizing layers was demonstrated; despite the increase in the total film thickness the layered structure of the films was maintained indicative of a uniform oxidation process. These differences in microstructure between thinner and thicker layers were reflected in the strength loss after annealing of the various films. For the thicker Pt layers a significant amount of the as deposited strength was maintained, with the softening likely due to an increase of the in-plane grain size from 10-30 nm to 20-50 nm. Films with thinner Pt layers exhibited a larger decrease in strength. The loss of the continuous interface between the Mo and the Pt layers, followed by the substantial oxidation and evaporation of the solid $MoO_3$, is proposed as being responsible for the larger losses in strength. These results show that although thinner layers led to stronger films at room temperature, thicker layers with the subsequent sacrifice in initial strength should be used for high temperature applications in order to maintain a substantial fraction of the strength and integrity of the film.

## 3.5 References

**[1]** Misra A, Hirth JP, Kung H (2002) Philos Mag A 82: 2935-2951

**[2]** Was GS, Foecke T (1996) Thin Solid Films 286: 1-31

**[3]** Misra A, Kung H (2001) Advd Engng Mater 3**:** 217-222

**[4]** Misra A, Hirth JP, Hoagland RG (2005) Acta Mater 53: 4817-4824

**[5]** Lee HJ, Kwon KW, Ryu C, Sinclair R (1999) Acta Mater 47: 3965-3975

**[6]** Misra A, Hoagland RG (2005) J Mater Res 20: 2046-2054

**[7]** Misra A, Verdier M, Lu YC, Kung H, Mitchell TE, Nastasi M, Embury JD (1998) Scripta Mater 39: 555-560

**[8]** McKeown J, Misra A, Kung H, Hoagland RG, Nastasi M (2002) Scripta Mater 46: 593-598

**[9]** Huang H, Spaepen F (2000) Acta Mater 48: 3261-3269

**[10]** Eakins LMR, Olson BW, Richards CD, Richards RF, Bahr DF (2003) Thin Solid Films 441: 180-186

**[11]** Morris DJ, Bahr DF, Anderson MJ (2008) Sens. Actuators A 141: 262-265

**[12]** Bonnotte E, Delobelle P, Bornier L, Trolard B, Tribillon G, (1997) J Mater Res 12: 2234-2248

**[13]** Vlassak JJ, Nix WD (1992) J Mater Res 7: 3242-3249

**[14]** Massalski, TB (1986) Binary Alloy Phase Diagrams, American Society for Metals, Metals Park, OH

**[15]** Underwood JH, Gullikson EM, Nguyen K (1993) Appl Opt 32: 6985-6990

**[16]** Werfel F, Minni E (1983) J Phys C: Solid State Phys 16: 6091-6100

**[17]** Barr TL (1978) J Phys Chem 82: 1801-1810

**[18]** Brox B, Olefjord L(1988) Surf Interf Anal 13: 3-6

**[19]** Jaksic JM, Vracar Lj , Neophytides SG, Zafeiratos S, Papakonstantinou G, Krstajic NV, Jaksic MM (2005) Surf. Sci. 598: 156–173

**[20]** Natesan K, Deevi SC (2000) Intermetallics 8: 1147-1158

**[21]** Geng DY, Zhang ZD , Zhang M , Li D, Song XP, Hu KY (2004) Scripta Mater 50: 983-986

**[22]** Gulbransen EA, Andrew KF, Brassart FA (1963) J. Electrochem. Soc.110: 952-959

**[23]** Misra A, Verdier M, Kung H, Embury JD, Hirth JP (1999) Scripta Mater 41: 973-979

# Chapter 4: Conclusions and Recommendations for the Mo/Pt system

## 4.1 Conclusions

The mechanical properties of the Mo/Pt multilayered system were studied using two techniques, nanoindentation and bulge testing. Multilayers with different bilayer periods were studied and the hardening behavior was similar to that reported for other fcc-bcc systems which form incoherent interfaces. For the layer thicknesses used in this study the confined layer slip model (CLS) seems to describe well the strengthening behavior of the nanocomposites. It was also shown that when the thickness of the Pt layer, the soft layer for this system, was kept the same (at approximately 100 nm) the hardness did not change significantly despite the different thicknesses of the Mo layer. This result indicates the importance of the soft layer, at the length scales investigated here, in determining the overall strengthening behavior of the nanostructure. Another observation of this study was the increase in the hardness of the films after aging in ambient conditions. The combination of the results of X-ray Photoelectron Spectroscopy with the evolution of residual stresses in the nanolayered films, acquired using the bulge testing technique, pointed to O incorporation as responsible for the aging behavior. Mo oxides that form at the Mo/Pt interface act as obstacles to dislocation glide, in the manner described by the Orowan strengthening mechanism, increasing the strength of the aged samples. The fact that no increase in strength was observed after the aging of annealed samples, where complete

oxidation of all the Mo layers occurred upon annealing, further verified the assumption that post sputtering deposition is responsible for the aging behavior.

Annealing of the Mo/Pt multilayer films in air at 475 $^{o}$C caused changes in the microstructure of all films, regardless of layer thickness. These changes were more significant when the Pt layers were thin, 20 to 35 nm in this study, where disruption of the layering occurred along with destructive oxidation of Mo, which involved vaporization of the forming oxide. For the 100 nm Pt thicknesses no spheroidization was observed and although again complete oxidation of all the Mo layers occurred, the Pt layers protected Mo from destructive oxidation. A novel growth mode in the oxidizing layers was demonstrated; despite the increase in the total film thickness the layered structure of the films was maintained indicative of a uniform oxidation process. These differences in microstructure between thinner and thicker layers were reflected in the strength loss after annealing of the various films. For the thicker Pt layers a significant amount of the as deposited strength was maintained, with the softening likely due to an increase of the in-plane grain size from 10-30 nm to 20-50 nm. Films with thinner Pt layers exhibited a larger decrease in strength. The loss of the continuous interface between the Mo and the Pt layers, followed by the substantial oxidation and evaporation of the solid $MoO_3$, is proposed as being responsible for the larger losses in strength. These results show that although thinner layers led to stronger films at room temperature, thicker layers with the subsequent sacrifice in initial strength should be used for high temperature applications in order to maintain a substantial fraction of the strength and integrity of the film.

## 4.2 Future work- Recommendations

The goal of this work was to improve the strength of Pt thin films used as bottom electrodes in MEMS devices by layering with another metal and ultimately make these films free standing. The first goal was achieved and the effects of varying bilayer period on the strengthening behavior were studied. However the presence of compressive residual stress in the films, despite their small value, did not allow the formation of free standing membranes. Hence future work includes the choice of a different metal as the second constituent in the layering sequence and investigation of the strengthening behavior in this case. Since high tensile stresses do not also allow the formation of free-standing membranes, the goal would be to have a nanocomposite structure with small tensile residual stresses.

The strain hardening of nanolayered films is an aspect that has not been adequately addressed in literature. A better understanding of strain hardening in multilayered composites is necessary especially if the fatigue behavior of these films is of interest. The effect of strain hardening for the Mo/ Pt system was not significant however it may play a significant role in other multicomponent systems. Investigation of the change in mechanical properties with strain would involve the use of nanoindentation where indenters with different tip geometries would be utilized. This would allow the measurement of hardness, and correspondingly flow stress, at different strains, giving an insight of the strain hardening behavior. These results would be then utilized for the fatigue testing of nanocomposites.

# Chapter Five: Characterization of Second Phase Precipitates in Polycrystalline YAG

## 5.1 Lasers

Lasers are used in numerous applications which include micromachining, welding, drilling and medical applications [1]. The acronym stands for Light Amplification by Stimulated Emission of Radiation; lasers produce a coherent, convergent and monochromatic beam of light [2]. The light production involves three different processes; population inversion, stimulated emission and light amplification. The population inversion which occurs between three or four energy levels in the active medium of the laser (Figure 5.1) is an excited atomic state where the higher energy levels have a larger number of electrons than the lower energy states. For the three level laser shown in Figure 5.1(a) absorption of electromagnetic radiation from a pumping source raises the electrons from the energy level $E_o$ to $E_2$. The lifetime of the electrons at this state is very small and rapid decay occurs to the level of energy $E_1$ with no emission of radiation. The fluorescence lifetime of this energy level is large and with time the desired population inversion between the energy levels $E_1$ and $E_o$ occurs. Similar is the process for 4 level lasers where the population inversion is established between the energy levels $E_1$ and $E_2$ (Figure 5.1 (b)). Once the population inversion is achieved a photon of frequency equal to $\nu=(E_1-E_o)/h$ triggers the emission of a photon with the same frequency by causing an electron transition to the $E_o$ energy level lowering the energy of the excited atom. The incoming and emitted photons have the same frequency, direction of travel and phase and as a result they interfere

constructively increasing the light amplitude. The active crystal is situated in a resonant cavity which allows the photons to pass through it many times causing additional light amplification after each pass. The resonant cavity consists of highly reflective and carefully aligned mirrors which are placed at each side of the crystal perpendicular to the cavity axis. One of the mirrors is almost 100 % reflective and the other allows partial transmission of the amplified beam which is the output of the laser.

Examples of crystals that are used in laser applications are Nd: $YVO_4$ and Nd: $Y_3Al_5O_{12}$ (YAG) with YAG being the one mainly used for industrial solid state lasers [1]. The dopant in the crystals, which for the examples mentioned here is Nd, is the active species of the laser media. Essentially the dopant atoms are the atoms where the three step process of population inversion, stimulated emission and light amplification takes place. Therefore a higher concentration of the active species is necessary for high power lasers [1].

The properties that make a crystal a good candidate as a laser medium and host of the active atoms are high thermal conductivity, chemical stability and the easiness of machining the crystal to the desired dimensions [1]. Crystals used in solid state lasers must also have a large product of the cross section of stimulated emission and the fluorescence lifetime, low lasing threshold and stable operation for both types of oscillation mode, continuous and pulse, as well as high conversion efficiency [1].

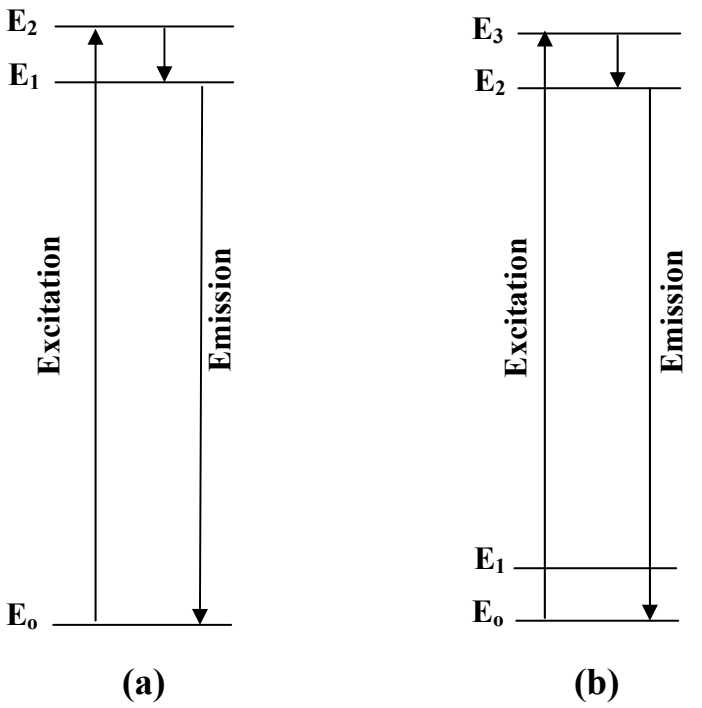


**Figure 5.1** Energy diagrams for three **(a)** and four **(b)** level lasers [1]

## 5.2 Single crystalline and ceramic YAG

Yttrium aluminum garnet crystals (YAG) ($Y_3Al_5O_{12}$) have attracted significant interest as the media in solid state lasers. Their optical and thermo mechanical properties make these crystals suitable for high efficiency laser oscillation [1]. Typically YAG single crystals are grown by the Czochralski method which is a time consuming and costly method. The amount of Nd that can be uniformly incorporated in the grown crystal is small, limited to about 1 at%, due to its low segregation coefficient [1, 3, 4]. This poses a

significant obstacle in the fabrication of compact high power lasers since higher Nd concentrations allow for a more efficient absorbance of light from the excitation source [1]. Due to the low segregation coefficient of Nd, during the growth of YAG crystal from the melt its concentration varies along the axial direction, resulting in a strained core [1]. Facets have also been reported which extend from the center of the boule towards its outer part parallel to the (211) planes [1, 5]. These facets have a non uniform concentration of Nd which results in optical inhomogeneity [1, 3, 5]. In order to avoid these problematic areas of the grown crystals that act as scattering sites and can deteriorate the beam quality, only parts of the ingot are drilled out and used in laser applications, which leads to a significant waste of material. In an attempt to overcome these issues, polycrystalline YAG was introduced as a substitute for single YAG crystals; these polycrystalline solids are commonly referred to as YAG ceramics to distinguish them from single crystals. The first transparent Nd: YAG ceramics were developed by Ikesue et al. [6-8] who reported successful laser oscillation using YAG polycrystals. It has been shown that the efficiency of polycrystalline YAG is at least equivalent to that of single crystals grown by the Czochralski method [9,10].

Ceramic YAG is synthesized using powders with particle sizes in the nanometer scale, which are sintered at high temperatures to form a dense structure. Two methods of forming polycrystalline YAG are documented in literature. The first is conventional sintering which uses single phase YAG powders (with particle dimensions on the 10's to 100's of nm's) obtained through a co- precipitation method [11, 12]. The second approach [7], uses reactive sintering of $Al_2O_3$, $Y_2O_3$ and $Nd_2O_3$ nanopowders with the appropriate

concentrations to form the YAG phase. The sintering process is facilitated by the use of sintering aids like $SiO_2$ decomposed from tetraethyl orthosilicate (TEOS) [8]. The role of Si in this case is dual; it helps in the densification process by making the mass transport during sintering easier [13] and also allows the incorporation of larger amounts of Nd in the lattice [6, 14, 15]. The ability to incorporate higher concentrations of Nd in the polycrystalline lattice than in the single crystalline case makes ceramic YAG very attractive for high power lasers.

Typical production of ceramic YAG, using the reactive sintering method, starts by ball milling the starting powders in water which includes an organic dispersant like methanol [3, 15]. A slurry is formed which is then dried using a spray drier and the resulting powder is pressed into discs. Calcination in air is commonly used to remove any organic residue from the discs [15]. The discs are usually sintered in vacuum at temperatures which range from 1700-1850 $^{o}$C [3, 6-8, 16]. Variations of this method include a presintering process in vacuum at 1600$^{o}$C with the discs being subsequently hot isostatically pressed in an argon atmosphere at temperatures which range from 1500$^{o}$C to 1700$^{o}$C before the final sintering step [8]. After the sintering process the ceramic product is translucent rather than transparent and a heat treatment in air is commonly used to obtain transparent crystals [3]. Examples of translucent as sintered YAG ceramics can be seen in Figure 5.2. This translucency has been attributed for other systems [17] to oxygen vacancies that are introduced during the sintering process in vacuum. It is suggested that annealing in air reintroduces the lost oxygen in the matrix.

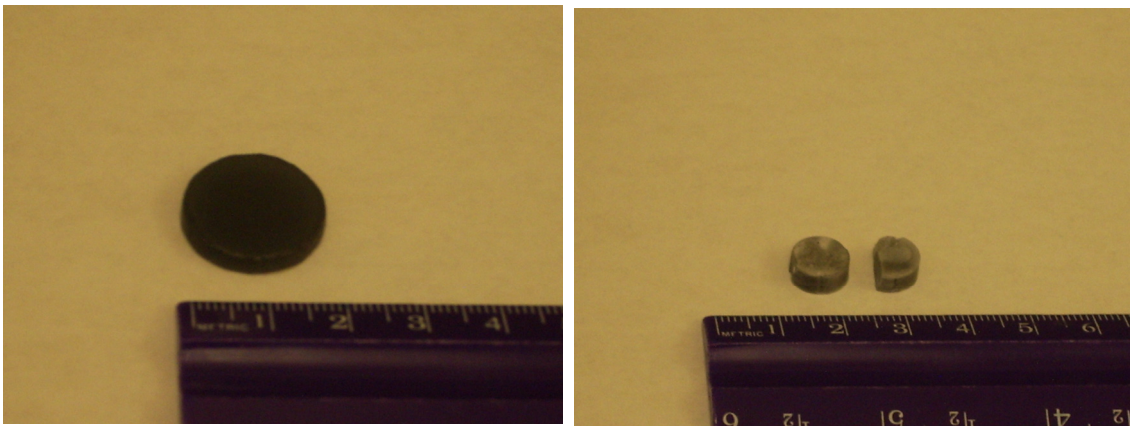

**Figure 5.2** Translucent specimens after sintering at temperatures typically used for the production of ceramic YAG. Annealing in air will make these specimens transparent

The major problem when using YAG as the laser media is the scattering of light which deteriorates the beam quality. In ceramic YAG, grain boundaries, residual pores, second phases and precipitates can act as scattering centers [1]. It has been reported that scattering from grain boundaries is minimal [6, 16] when no second phases are present along the interface. The presence of second phases, in the form of a thin film along the grain boundary, has been linked to the use of silica as a sintering aid [16]. Previous work has focused on some of the sources of scattering, mainly second phases along the grain boundaries and porosity [8,16]. In [15] the effect of silica on the reactive sintering of the ceramic YAG was investigated and second phases were identified in as sintered samples. However little attention was given on other types of precipitates that can be present in the transparent ceramics or how different heat treatments of as-sintered samples affect the precipitation behavior. In this work a systematic study of precipitation in as sintered and subsequently annealed samples is presented. This allows a correlation between the different

growth conditions and the observed microstructure. The final structure will affect the performance of the material as a laser active medium so a better understanding of the conditions under which each microstructure occurs is necessary in minimizing or even eliminating the presence of scattering in the final products. In addition to the precipitation behavior, issues related to the reactive sintering approach for ceramic YAG growth will be presented in this chapter.

## 5.3 Experimental details

In order to examine the solid state precipitation behavior of ceramic YAG, a number of different samples were used; samples were provided from a commercial source of YAG materials. Specimens with slightly different concentrations of the starting powders were investigated in order to evaluate the effect of stoichiometry on the observed microstructure and more specifically the formation of precipitates. In Table 5.1 the different off stoichiometry samples used in this study are presented. The growth process of the ceramic YAG specimens involved sintering at a temperature of 1800 $^{o}$C followed by a heat treatment in air at 1400 $^{o}$C, unless otherwise specified, after which all samples were optically transparent. The temperatures used for both steps were typical growth conditions presented in literature [3, 8, 15]. Thermal etching at 1550 $^{o}$C was utilized in some cases to reveal the grain size distribution.

For specimens where precipitation did occur, the effects of post sintering annealing on the precipitate evolution were further investigated. Sintered specimens with the same composition were annealed for different amounts of time and at different

temperatures. In this case the surface of the samples was mechanically polished before any thermal treatment took place and no further surface treatment was used once the annealing was complete. All heat treatments in air were performed with a Lindberg 1800 $^{o}$C box furnace. All samples were heated at a rate of 8 $^{o}$C/ min up to 800 $^{o}$C and then at a rate of 4 $^{o}$C/ min up to the target temperature and held for the desired time. After the completion of the heat treatment the samples were furnace cooled to room temperature.

All microstructures were investigated using a Sirion 200 Field Emission Scanning Electron Microscope equipped with an Energy Dispersive X-ray Spectrometer. Quantitative information about the precipitates was obtained using a Cameca Camebax electron microprobe with a Wavelegth Dispersive X-ray Spectrometer. A Siemens D-500 X-ray powder diffractometer was also used to acquire X-ray diffraction patterns from samples where precipitation occurred.

## 5.4 Results – Discussion

### 5.4.1 Typical problems associated with reactive sintering

When reactive sintering is used for the production of YAG, ceramic nanopowders of a-$Al_2O_3$, $Y_2O_3$ and $Nd_2O_3$ are weighted and sintered such that after the chemical reaction YAG with the desired concentration of the Nd dopant is acquired [15]. Residual pores, second phases and precipitates that are present in the final product can act as scattering centers and affect the performance of the laser. In this section examples of different problems that have been observed for YAG specimens grown by the reactive sintering

approach will be presented, whereas a more detailed investigation of the second phases and precipitates will follow.

In Figure 5.3 the SEM micrograph of a YAG fracture surface is shown where some porosity is still present after the sintering process.

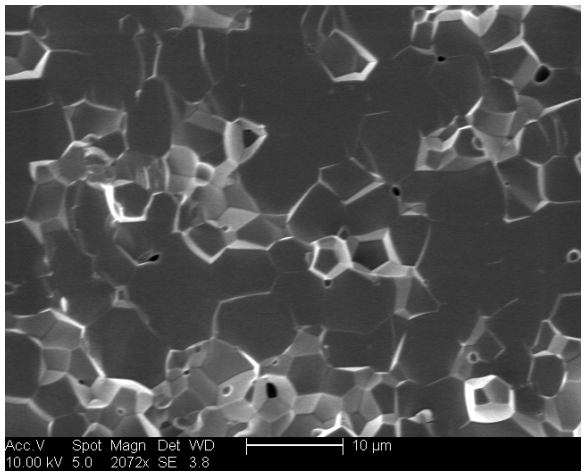


**Figure 5.3** Residual pores at the grain boundaries of sintered YAG sample as seen on a fracture surface taken from one of the specimens

The micrographs in Figures 5.4 (a) and 5.5(a) present cases where it seems that incomplete reaction during sintering leaves spheres of pure alumina behind. The nature of these areas is confirmed by using EDS in the SEM (Figures 5.4(b),(c),(d) and 5.5(b)). At high sintering temperatures (1700 $^{o}$C) even for samples with the stoichiometric composition the presence of alumina areas has also been reported in literature [15]. Similar areas with those reported in [15] were found in YAG specimens used in the present study and can be seen in Figure 5.6 appearing dark compared to the surrounding YAG matrix.

The use of sintering aids and the deviation of the starting composition from the YAG stoichiometry result in the presence of second phases in the ceramic product. An

example of Si rich precipitates that have formed along grain boundaries in a YAG specimen can be seen in Figure 5.7. The precipitation behavior as a function of composition and processing conditions will be investigated in more detail in the next sections.

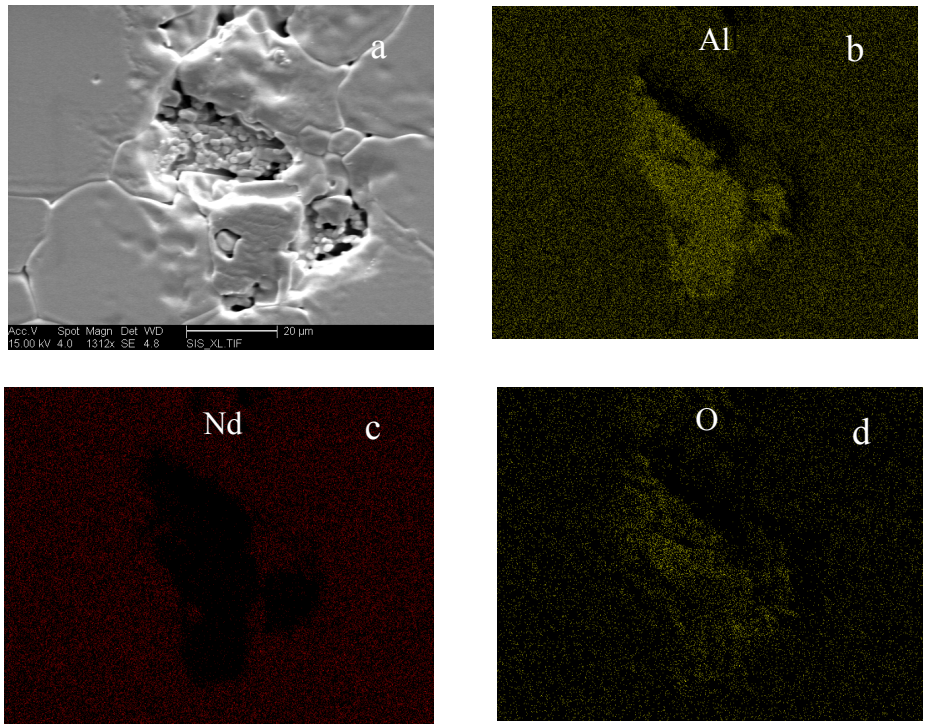


**Figure 5.4 (a)** Secondary Electron Micrograph of an area where incomplete reaction of the starting powders has occurred. The area in the center of the micrograph where small spheres are present is pure alumina as confirmed by the elemental maps acquired using EDS (**b, c, d**)

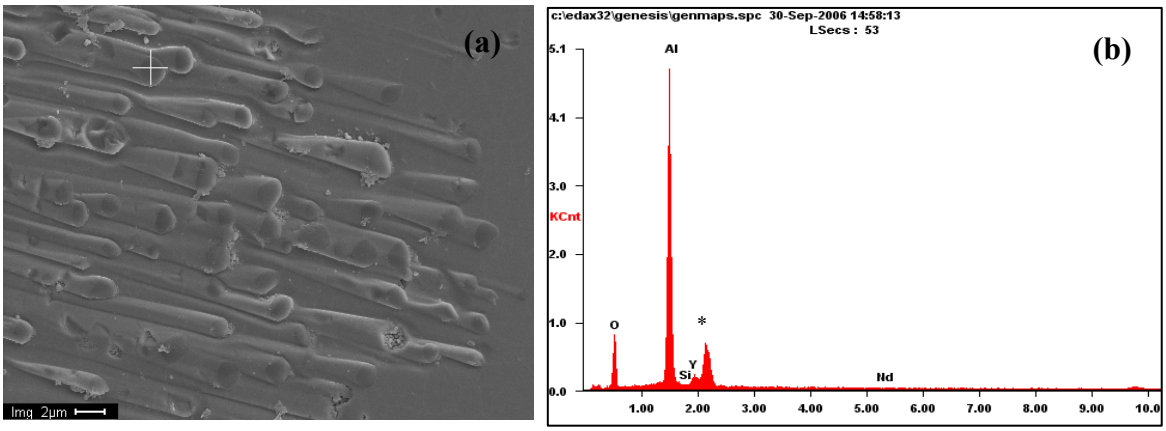


**Figure 5.5 (a)** Spherical alumina inclusions on the surface of ceramic YAG as confirmed by EDS **(b)** EDS spectrum of the spherical areas seen in (a), * marks the position of the Au peak

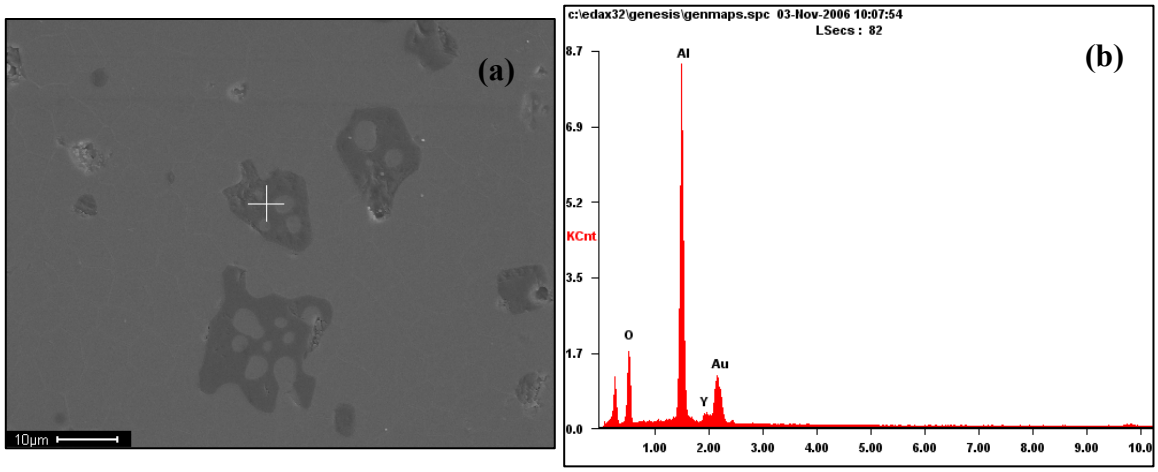


**Figure 5.6 (a)** $Al_2O_3$ (dark areas) in the YAG matrix (lighter contrast) **(b)** EDS spectrum from the dark areas of (a) showing that they are pure alumina

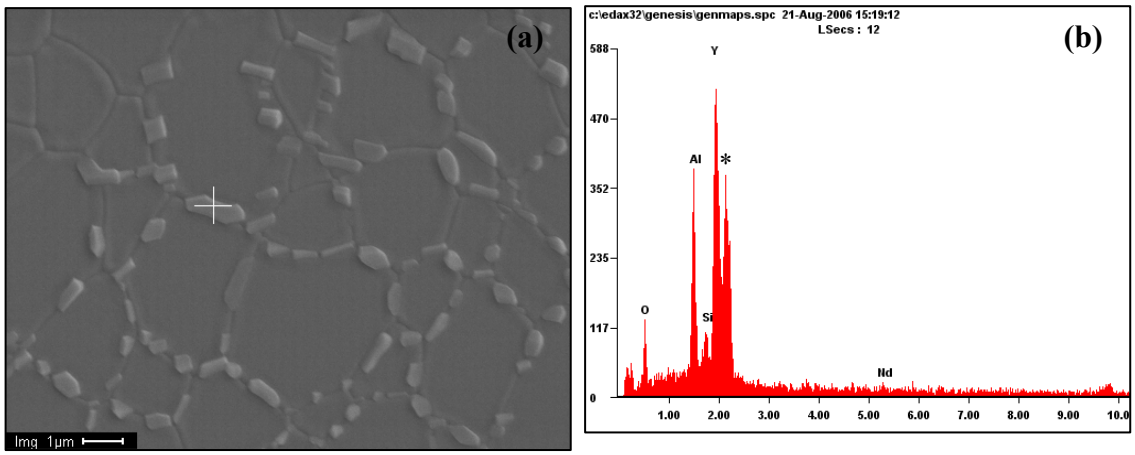


**Figure 5.7 (a)** Si- rich second phases precipitating along the YAG grain boundaries **(b)** Spectrum taken from the precipitates shown in (a)the * marks the position of the Au peak

### 5.4.2 Second phases and stoichiometry

As it has been already mentioned when reactive sintering is used for the production of ceramic YAG, nanopowders of the starting materials, namely a-$Al_2O_3$, $Y_2O_3$ and $Nd_2O_3$, are mixed in specific concentrations so that after sintering the ceramic with the desired Nd concentration is produced. Silica is also commonly added as a sintering aid to assist in the densification process of the ceramic. From the phase diagram of the $Al_2O_3$-$Y_2O_3$ system [18], where YAG appears as a line compound, it is apparent that small deviations from stoichiometry can cause significant differences in the resulting microstructure. In order to investigate the effect of these deviations on the YAG microstructure three samples with slightly different off stoichiometry compositions were investigated. The compositions used are shown in Table 5.1. All samples had approximately 1% TEOS as a sintering aid. The specimens were sintered and post annealed at typical temperatures used in the processing of

YAG ceramics [3, 8, 15]. For samples 1 and 2 the deviation from the stoichiometric composition showed no precipitation on the surface of the ceramic when examined using the SEM. However as the concentration of Yttria increased for specimen 3, precipitates formed on the surface and were observed using secondary electron imaging in the SEM (Figure 5.8). The precipitates mainly appeared along grain boundaries or at triple points between the grains with less precipitation present within the grains. The areas where second phases appear in the volume of the grains could correspond to the position of the initial grain boundaries before grain growth took place during the sintering process. Electron Dispersive Spectroscopy showed that the precipitates are Si and Y rich compared to the composition of the YAG matrix (Fig. 5.9). However due to the small size of the precipitates the interaction volume of the X-rays is comparable or larger than their size hence only qualitative conclusions could be drawn from this analysis.

**Table 5.1** Off stoichiometry compositions used to study second phase precipitation in YAG ceramic

| **Sample** | **Off stoichiometry composition** |
|---|---|
| 1 | 1% Alumina rich sample |
| 2 | <<1% slightly Yttria rich sample |
| 3 | 1% Yttria rich sample |

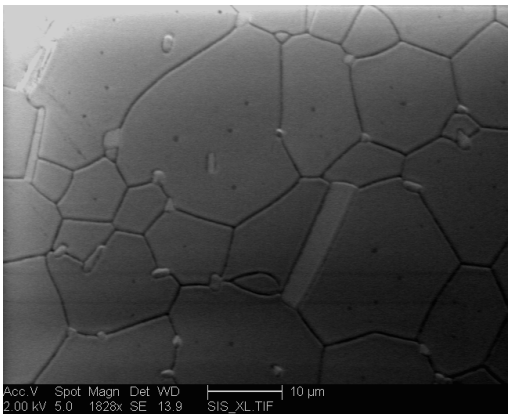


**Figure 5.8** Precipitates are present on the surface of the yttria rich sample (sample 3). Most of the precipitation occurs along grain boundaries and at triple points. Some precipitates can be seen within the body of the grains

Other features seen on the surface of sample 3 are round formations where material is missing in the center and precipitation occurred in a circular pattern around it (Figure 5.10 (a). EDS analysis indicated that the second phases had a very high concentration in Si (Figure 5.10 (b)). These formations are not likely the result of the deviation from stoichiometry since they have been observed on a number of samples with varying initial compositions. The common factor in all these different specimens was the use of $SiO_2$ as the sintering aid.

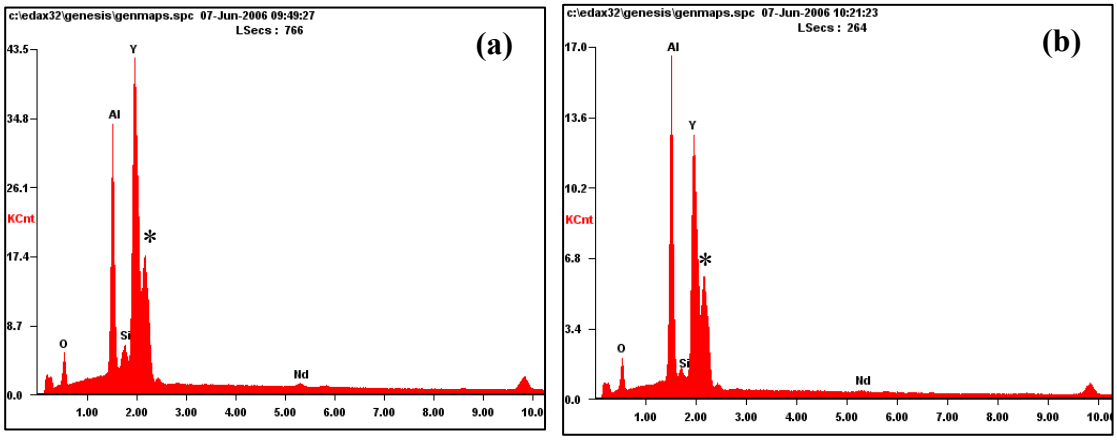


**Figure 5.9 (a)** EDS spectrum as taken from one of the precipitates seen in Fig. 5.8. The peak marked with * corresponds to Au which was used to prevent charging of the sample surface in the Scanning Electron Microscope. **(b)** EDS spectrum taken from the YAG matrix of the Yttria rich sample (sample 3). Again * marks the position of the Au peak

An example of this circular formation on a specimen with different initial composition than sample 3 can be seen in Figure 5.11 (a). TEOS was used in this case as the sintering aid. The surface of the specimen was studied after the sample was sintered and subsequently annealed at 1400 $^{o}$C for 6 hours. The similarity of this formation to the circular ones seen on the surface of sample 3 (Figure 5.10) is apparent. The only difference between the two formations is that for the precipitation seen in the micrograph of Figure 5.11 a second phase was present in the center. Electron Dispersive Spectra collected from this central region showed high concentration in Si. Upon further annealing for 1 hour at 1550 $^{o}$C the center of the formation was completely depleted of the second phase and precipitation was present at larger distances from the center (Figure 5.11(b)). The wetting of the ceramic free surface by this second phase, the high concentration of Si and the lack of a strong crystalline facet structure suggests its amorphous nature. Orientation Imaging Microscopy was carried out on these samples and no clear diffraction could be achieved

from these features. While this result is not unequivocal proof of the phase being amorphous, when coupled with the known chemistry it does suggest it is a glass phase, rather than a crystalline structure. This area is probably the result of insufficient mixing of the sintering aids in the initial nanopowders which results in their accumulation in one area. During sintering a liquid phase forms which, upon cooling to room temperature, solidifies and wets the ceramic surface. Post sintering annealing at high temperatures (> 1400 $^{o}$C) causes remelting of the silicate phase, which then moves along the grain boundaries. The mass transport along the YAG interfaces can be attributed to capillary forces that act as a result of surface tension. Upon cooling to room temperature the silicate phase solidifies forming the precipitates seen at the grain boundaries. Whether the second phase will completely wet the grain boundary or will mainly appear at triple junctions depends on the solid YAG-solid YAG and solid YAG- liquid phase surface energies [19]. Even if complete wetting at high temperatures occurs, slow cooling to room temperature will cause partial dewetting [19]. Although Transmission Electron Microscopy which can discern the presence of very thin films along the grain boundaries hasn't been used, SEM micrographs taken from the periphery of round formations at higher magnifications (Figures 5.7 and 5.12) show that a considerable amount of the silicate phase appears at the interfaces between YAG grains and it hasn't completely retracted at triple junctions.

To further prove that the glass phase is very mobile and readily diffuses along grain boundaries at temperatures typically used for post sintering annealing of YAG ceramics, an experiment was conducted. A fused sample (pure $SiO_2$) was placed on a piece of polycrystalline YAG that did not contain silica additives (Figure 5.13). The two pieces

were placed in the furnace and were heat treated at 1400 $^{o}$C for 6 hours. Since no glass was present in the ceramic prior to the heat treatment, any silicate phase detected at the grain boundaries of the specimen after annealing would have originated from the quartz piece. After the thermal treatment a cross section of the specimen was prepared by mechanically polishing down to 1 μm diamond lapping film. The cross section was investigated in the SEM and it was found that the quartz had indeed diffused along the grain boundaries forming an intergranular film (Figure 5.14). Compositional maps obtained by EDS confirmed that grain boundaries were wetted by the quartz and that the amorphous phase had penetrated at a considerable depth inside the ceramic (Figures 5.15 and 5.16). In Figure 5.17 the similarity between the Si compositional map obtained from the cross section of the YAG sample with the quartz piece on top and the same map corresponding to the surface of a YAG ceramic, where silica has been used as a sintering aid, is apparent.

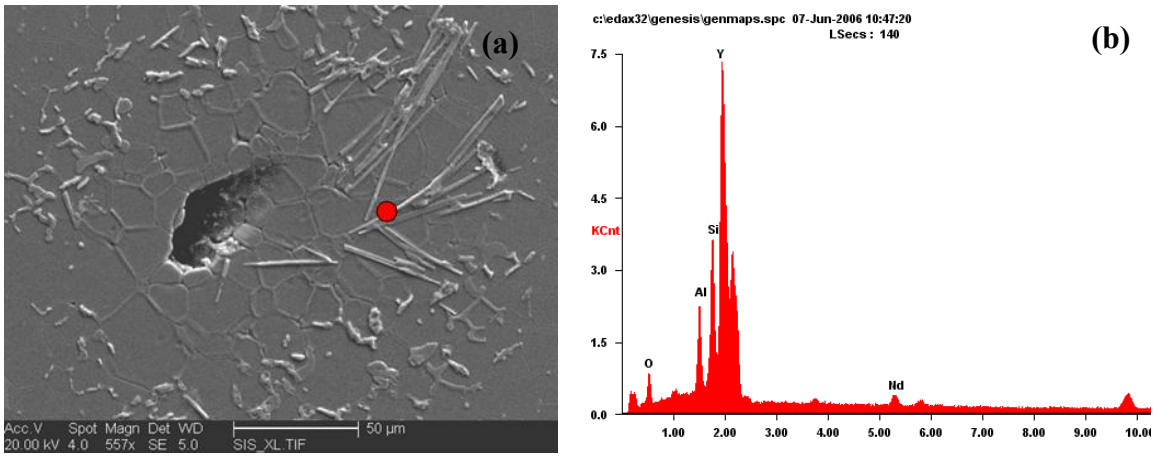


**Figure 5.10 (a)** Example of a round formation as observed on the surface of a sample after sintering and thermal annealing were complete **(b)** High concentration in Si is detected using EDS

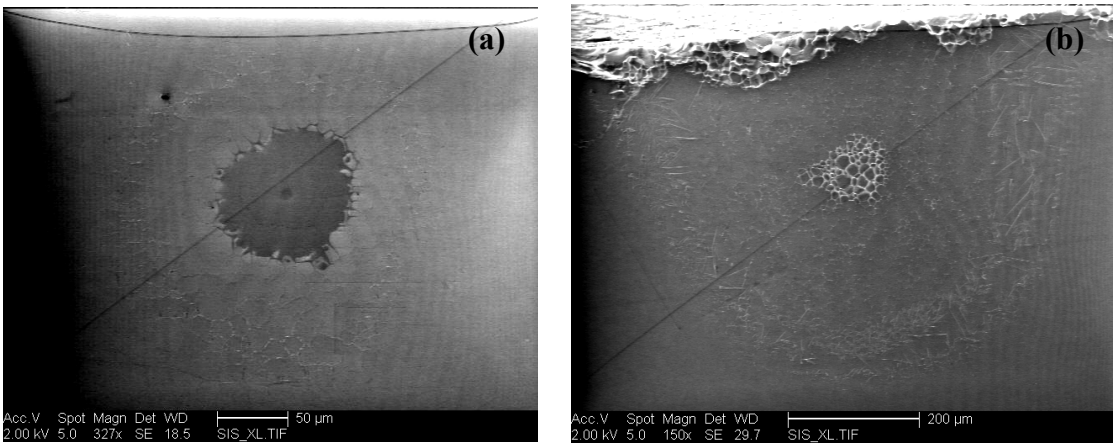


**Figure 5.11 (a)** Surface of a YAG sample after processing is complete (sintering and annealing at 1400 $^{o}$C for 6 hours). The dark area in the center of the micrograph is a second phase rich in Si. Precipitation is present around this second phase area. **(b)** Further annealing at 1550 $^{o}$C for 1 hr completely depletes the center from the second phase. Precipitation is now present at a larger distance from the center of the formation indicative of a diffusive process

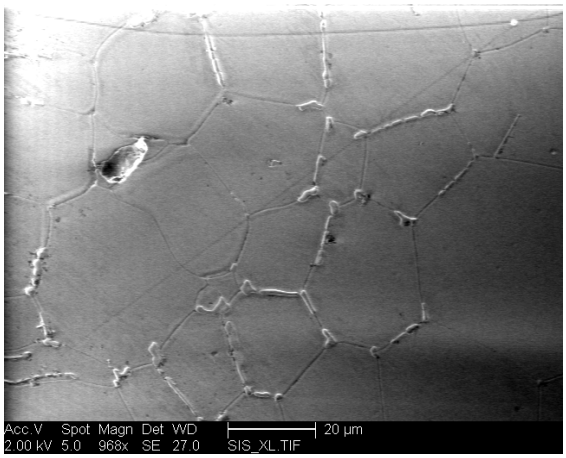


**Figure 5.12** The silicate phase appears at the interfaces between the YAG grains

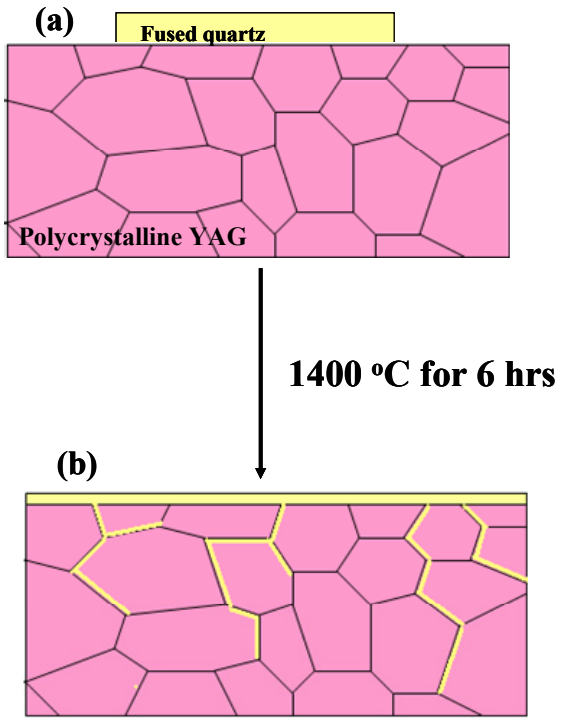


**Figure 5.13** A schematic view of the specimen used to study the penetration of glass in ceramic YAG. Quartz was placed on the surface of the ceramic **(a)** and annealing at 1400 $^{o}$C for 6 h followed. After the thermal treatment the presence of glass along grain boundaries was evident **(b)**

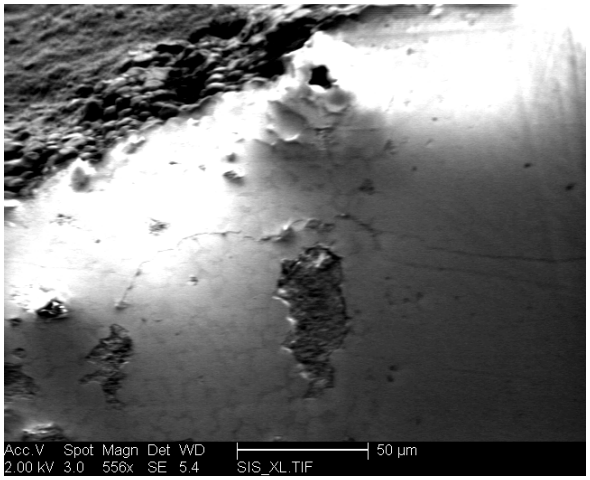


**Figure 5.14** Cross section of the specimen described in Figure 5.13. The darker contrast areas along the grain boundaries are the glass phase.

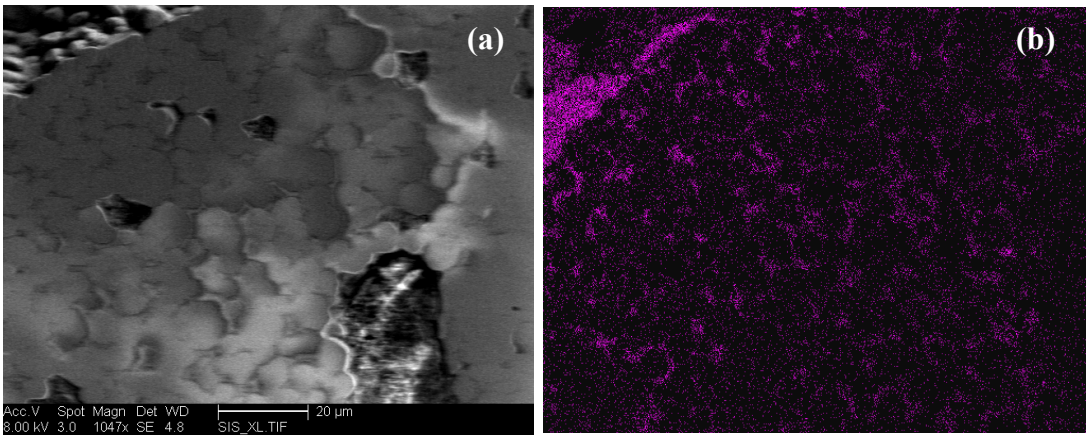


**Figure 5.15 (a)** Area of the specimen shown in Figure 5.13 where the penetration of glass along the grain boundaries can be seen as a darker contrast area. **(b)** Si compositional map of the area shown in **(a)** verifying the presence of quartz along the grain boundaries

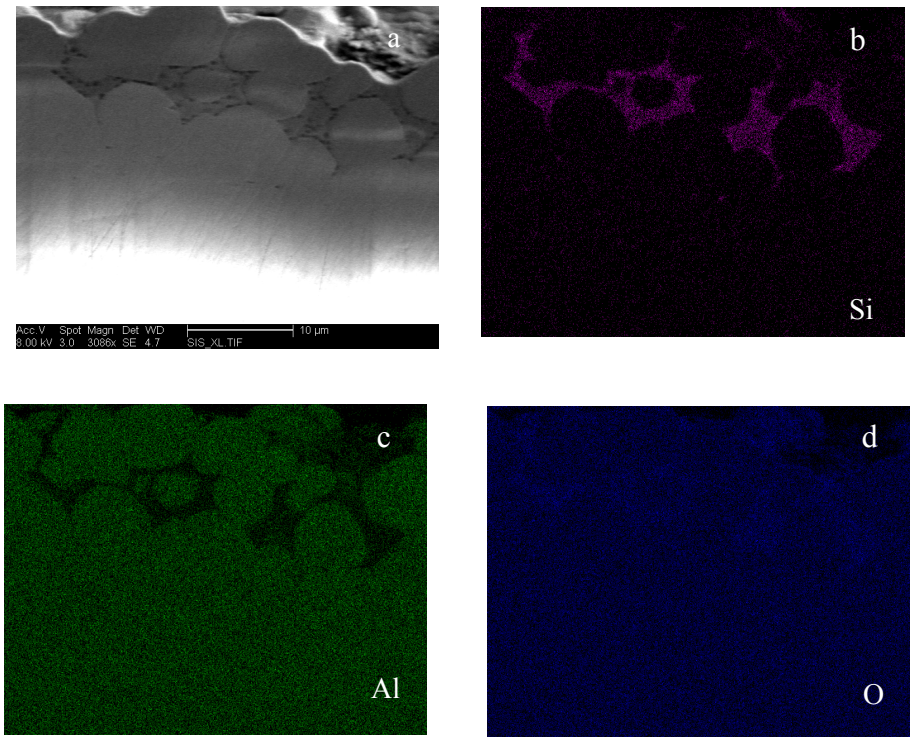

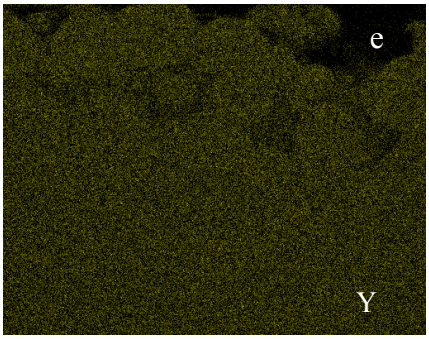


**Figure 5.16** Compositional maps for Si **(b)**, Al **(c)**, O **(d)** and Y **(e)** from the area of the specimen shown in **(a)** (SEM micrograph) acquired using EDS

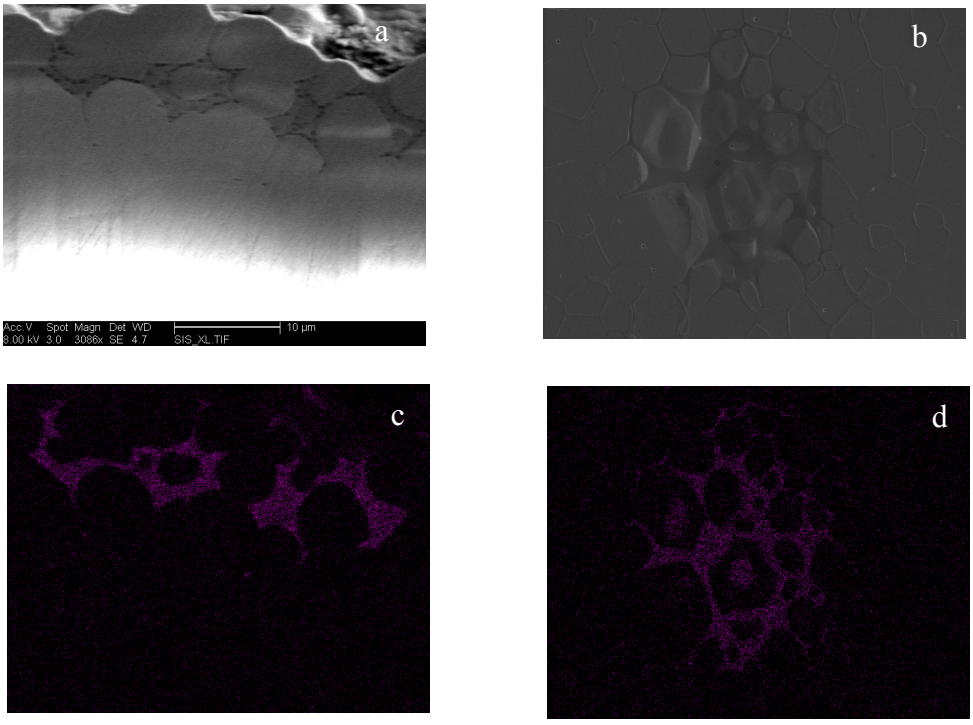


**Figure 5.17 (a)** and **(c)** silicate second phase along the grain boundaries for the specimen with the quartz piece on top after annealing at 1400 $^{o}$C. **(b)** and **(d)** surface of a ceramic YAG specimen where silica was used as a sintering aid. The appearance of the Si rich second phase at the grain boundaries in **(d)** is very similar to that in **(c)**

### 5.4.3 Evolution of microstructure with time

It is apparent that there are two instances when second phases appear in ceramic YAG. The first is when there is a deviation from YAG stoichiometry where the composition of the starting powders lays either within the Yttria or the Alumina rich area of the phase diagram and the second is when $SiO_2$ is used as a sintering aid. For some of the samples used in this study both these conditions were present. In this section the evolution of the second phase precipitates as a function of temperature and time used for the post-sintering annealing process was investigated.

In order to carry out this study a YAG specimen with $Y_2O_3$ – excess was chosen. Pieces were cut from the sample and each one was subjected to a different heat treatment. The first samples taken from the as sintered disc were annealed at 1400 $^oC$, which is a typical temperature used during YAG processing, for 2.5, 6, 36 and 216 h. Representative micrographs from the sample surface after each cycle can be seen in Figure 5.18. Even after 2.5 h precipitates can be seen on the sample surface although their size makes the quantitative elemental identification using EDS analysis impossible. These micrographs show that as the precipitate size increases with time their number decreases [20].

At 36 h the precipitates were large enough that a semi-quantitative analysis was possible. EDS didn't detect Si in the second phases however a difference in the relative concentrations of Al, Y and O between the precipitates and the matrix was found. This qualitative analysis showed that the concentration of Y in the matrix was higher than the corresponding concentration at the sites of precipitate formation. X-ray diffraction was chosen to investigate the nature of the precipitation and help determine whether the

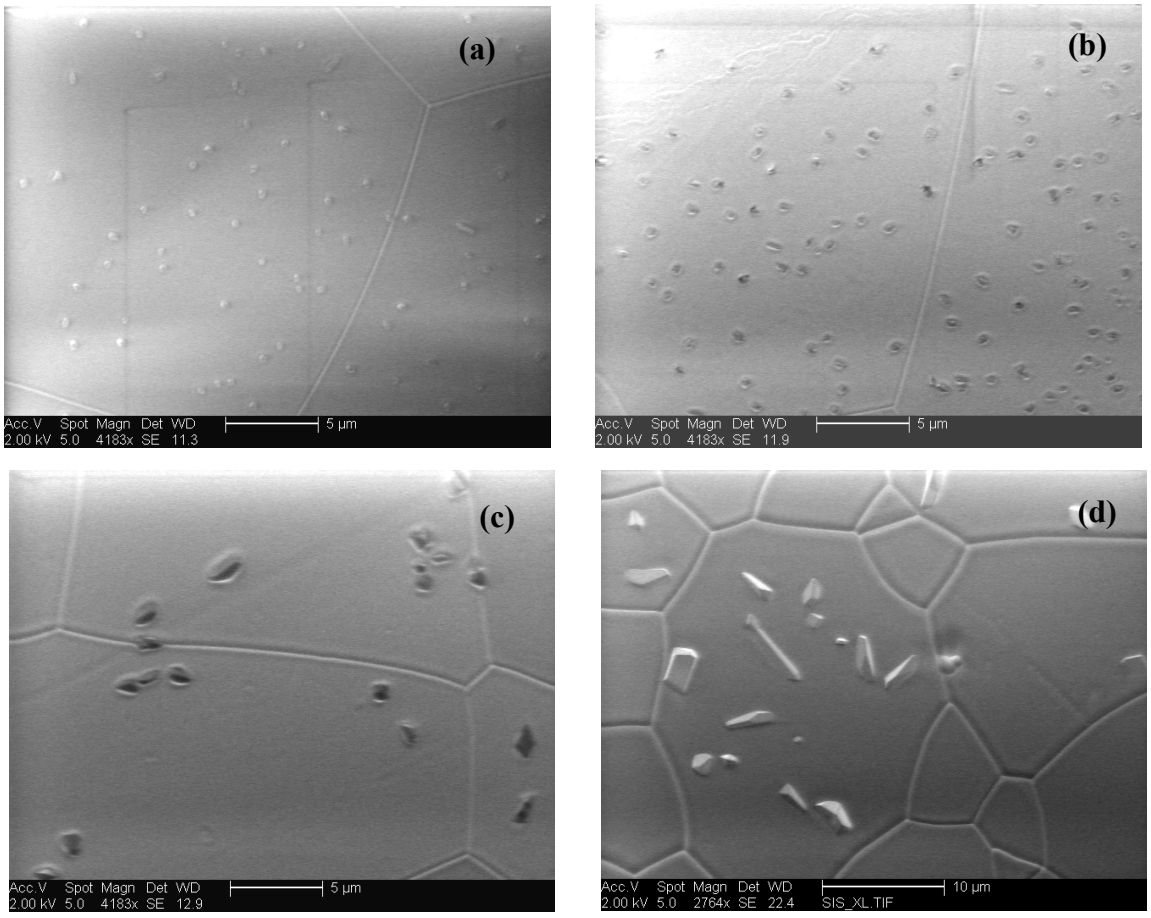


**Figure 5.18** Evolution of precipitation with time for post sintering annealing of the yttria rich sample at a temperature of 1400 $^{o}$C **(a)** 2.5hrs, **(b)** 6hrs, **(c)** 36hrs and **(d)** 216 hrs

precipitates are crystalline or amorphous. The X-ray diffraction pattern was collected from the sample annealed for 216 h and is shown in Figure 5.19. In addition to peaks corresponding to the YAG phase, which is the dominant contributor to the pattern, a few low intensity peaks were also present. These peaks were identified as $Al_2Y_4O_9$ (YAM) peaks by comparing them to the available pdf cards. In Table 5.2 the measured d-spacings are compared to the theoretical d-spacings for the two phases. The above results are

consistent with an yttria rich YAG matrix. Annealing of the samples at 1400 $^{o}$C allows the precipitation of the yttria rich second phase (YAM) from the saturated matrix. An average precipitate size was measured for all annealing times by using 10 fields of view in each case. Plotting the precipitate size as a function of post sintering annealing time at 1400 $^{o}$C (Figure 5.20) and fitting the data points reveals a square root type of dependency. The parabolic kinetics for precipitate growth indicates a diffusion controlled process.

EDS revealed the presence of Si in precipitates after 216 h of annealing at 1400 $^{o}$C (Figure 5.21). This indicates that the Si impurity from the sintering aid can dissolve in the YAM phase. Similar results have been reported in [21] where 2% $Y_2O_3$-excess YAG specimens were studied. In that case YAP containing Si was found at intragranular sites while no Si segregation was detected at the grain boundaries. It was assumed that the second phase precipitated during sintering and that the YAP particles attracted the Si from the grain boundaries effectively cleaning them. Since the YAP precipitates were found in the body of the grains it was assumed that they formed at the initial grain boundaries before grain growth occurred. In a similar manner $Al_2O_3$ particles in $Y_2O_3$/$Yb_2O_3$ stabilized zirconia reportedly attracted $SiO_2$ removing it from the grain boundaries [22]. For the specimen studied here no Si was detected after 36 h of post sintering annealing indicating that the incorporation of Si in the YAM phase was not done during the sintering process or that the Si concentration was not in appreciable amounts for EDS detection. However with increasing annealing time the amount of Si present in the precipitates increased to detectable amounts indicating that Si diffusion did occur. The temperature of 1400 $^{o}$C used for the annealing process is close to the temperature of 1660 K (1387 $^{o}$C) where it is

reported that liquid phases appear for the $Al_2O_3/Y_2O_3/Nd_2O_3/SiO_2$ system [15] making the presence of a liquid phase along the grain boundaries probable. The liquid phase would enhance the mass transport and allow the diffusion of Si to the YAM phase. If this is the mechanism by which Si is removed from the grain and incorporated in the YAM precipitates, it is expected that the properties of the grain boundaries would change with increasing annealing time. An indirect verification of this change was offered by studying the fracture surfaces of the specimens.

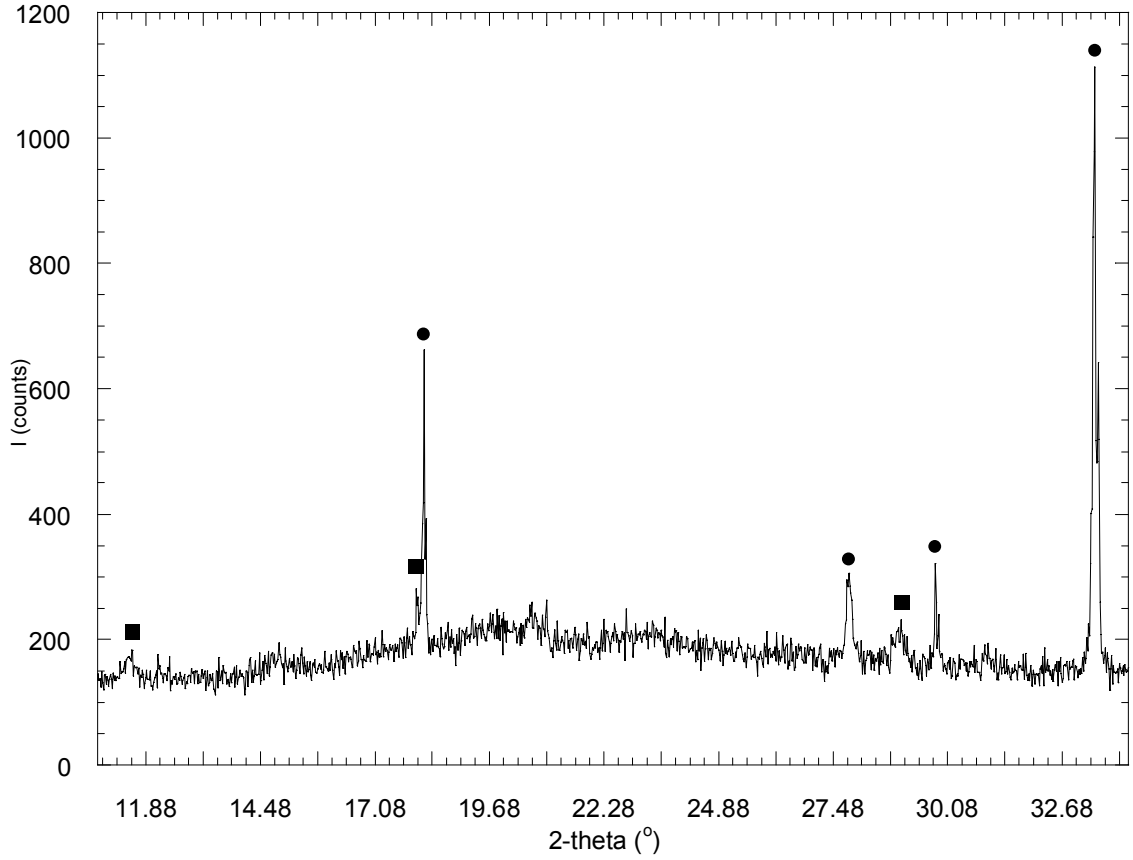


**Figure 5.19** X-ray diffraction pattern of the YAG sample annealed at 1400 °C for 216hrs after sintering. The peaks marked with (●) correspond to YAG whereas those marked with (■) correspond to YAM. Only part of the collected pattern is shown for clarity

**Table 5.2** Phase identification using the X-ray diffraction pattern shown in Figure 5.19

| $d_{obs}$ | $d_{theor}$ | phase |
|---|---|---|
| 7.6518 | 7.4390 | YAM |
| 4.9149 | 4.7084 | YAM |
| 4.8706 | 4.8990 | YAG |
| 4.2312 | 4.2426 | YAG |
| 3.2021 | 3.2071 | YAG |
| 3.0740 | 3.0180 | YAM |
| 2.9952 | 3.0000 | YAG |
| 2.6796 | 2.6833 | YAG |
| 2.4441 | 2.4495 | YAG |
| 2.3479 | 2.3534 | YAG |
| 2.1871 | 2.1909 | YAG |

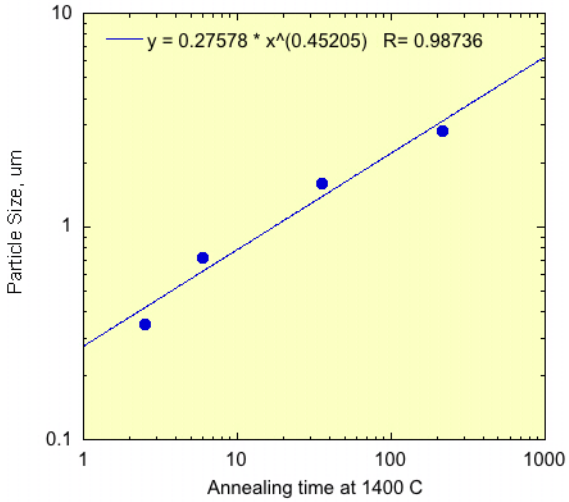


**Figure 5.20** Particle size as a function of time for sample 4 annealed at 1400 $^{o}$C. The data show a parabolic dependency described by an equation of the form $d=a*t^{b}$, where a=0.27578 and b=0.45205.

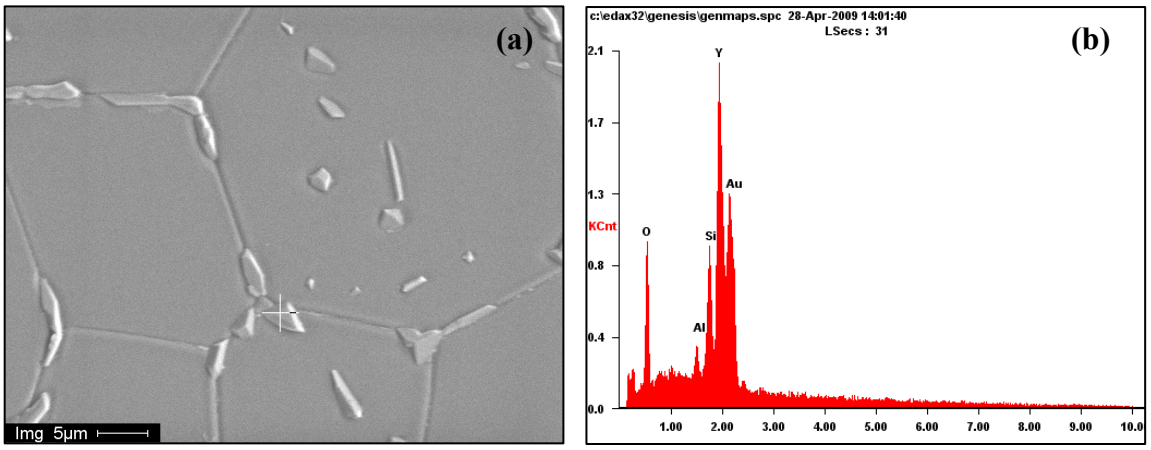


**Figure 5.21 (a)** EDS shows that after annealing for 216 h the precipitates shown in **(b)** are Si rich

Fracture surfaces were obtained from all the samples annealed at 1400 $^{o}$C post sintering. This was done by introducing a small notch on the surface of each specimen using the preloading function of a Rockwell hardness tester followed by the application of a larger load which resulted in fracture. The fracture surfaces that were obtained from each specimen, showed a change of the fracture mode from mainly intergranular (Fig. 5.22 (a)) at small annealing times to mainly transgranular (Fig. 5.22 (b)) at the longest annealing time. Hence as the annealing time increased the grain boundaries became stronger. The presence of a glassy phase along the grain boundaries could definitely weaken them, so this observation suggests the removal of the silicate phase with annealing time. This would agree with the assumption that Si is incorporated in the YAM precipitates with time. The YAG specimens with the best lasing properties, where grain boundaries are assumed free of intergranular second phases, show exclusively transgranular fracture further emphasizing the correlation between the absence of second phases and the increased strength of the grain boundaries.

In order to examine whether different processing conditions affect the precipitation behavior of samples with the same composition a second temperature was chosen for the post sintering annealing. Specimens taken from the same Yttria rich sample as above were annealed at 1250 $^{o}$C. A representative micrograph of the surface after 36 hours is shown in Figure 5.23. Comparison of this micrograph to the one presented in Figure 5.18 (c) (same annealing time but different temperature) reveals significant differences. The precipitates in this case are larger in size and have irregular boundaries in contrast to the faceted boundaries seen after heat treating the samples at 1400 $^{o}$C. These differences indicate the different nature of the precipitates. WDS was used to determine the wt% composition of areas marked A (precipitate) and B (matrix) in Figure 5.24 (a). The corresponding values can be seen in Table 5.3. Carbon is detected because it is used to coat the surface of the sample in order to prevent electron charging on the surface. These results show that the second phase contains a high percentage of Si whereas no Si was detected in the matrix.

Once the quantitative analysis of the specimen annealed at 1250 $^{o}$C was complete 100 μm of material were cut off the sample surface. The material was removed using an Ar plasma cutter and the cut was done parallel to the sample surface. This allowed an investigation of whether the extensive surface precipitation could also be seen in the bulk of the ceramic. From the micrograph shown in Figure 5.24 (b) it is apparent that the presence of second phases is extremely limited, only appearing at a few triple junctions. This finding in conjunction with the Si rich composition of the precipitates leads to the conclusion that what is seen on the sample surface is intergranular glass, remnant of the liquid phase sintering, that is expelled to the surface during annealing. If the second phase

was YAM, as was the case for the samples annealed at 1400 $^{o}$C, precipitation would be present throughout the specimen and not only on the surface.

According to the literature when liquid phase sintering is used post sintering processes can either cause crystallization of the glassy film present at the boundary [23, 24] or expulsion of the glass to the surface [25-27]. The expulsion of glass depends on the surface energies of the grain boundaries and the free surface. If it is energetically favorable for the liquid to wet the free surface then the glassy film will be expelled to the surface. Upon cooling from the annealing temperature the glass wetting the free surface will form droplets. The expansion of the glassy phase with heating could also be responsible for the mass transfer to the free surface. However it has been shown in [27] that when Alumina bicrystals of different orientations were used there were instances where the second phase appeared on only one of the two free surfaces, pointing to differences in surface energy and not volume expansion as the driving force for the expulsion.

The results for the two different annealing temperatures used for the post sintering processing show that at 1400 $^{o}$C precipitation of an Yttria rich crystalline phase is possible whereas at 1250 $^{o}$C silicates are expelled to the free surface.

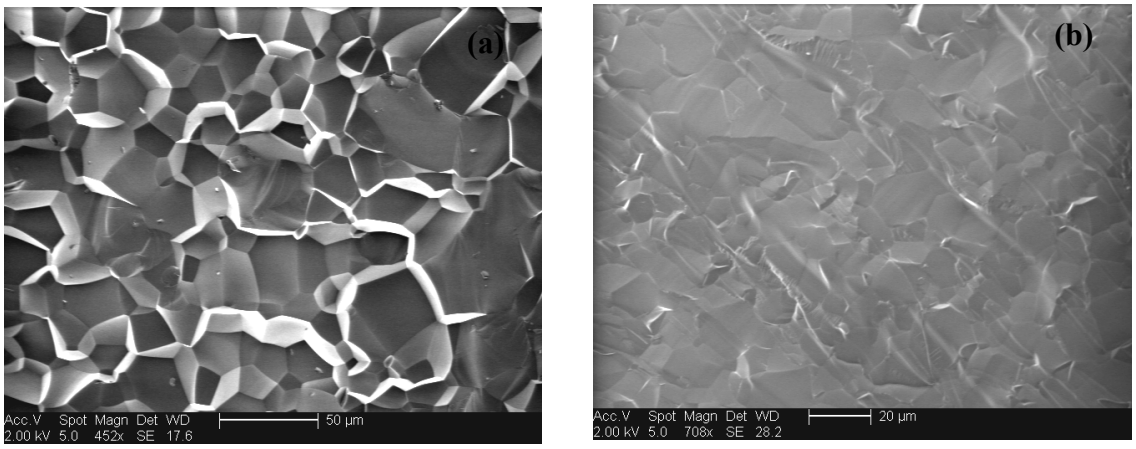


**Figure 5.22 (a)** Sample 4 at 2.5 h of post sintering annealing shows intergranular fracture. **(b)** The same YAG sample at 216 h of post sintering annealing, shows transgranular fracture.

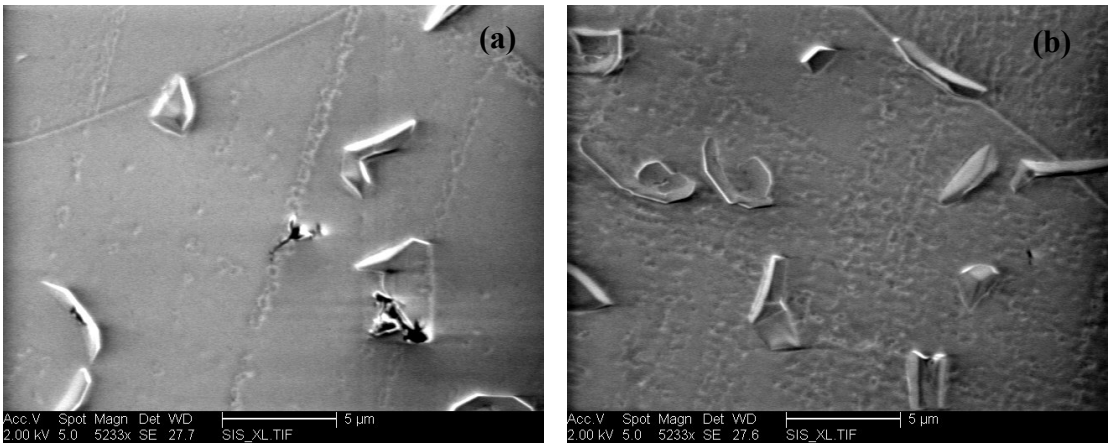


**Figure 5.23 (a)** and **(b)** Precipitation seen on the surface of the yttria rich sample after annealing at 1250 $^{o}$C for 36 h. Differences in the size and appearance of these precipitates can be seen when they are compared to the ones that formed after annealing of the same sample at 1400 $^{o}$C

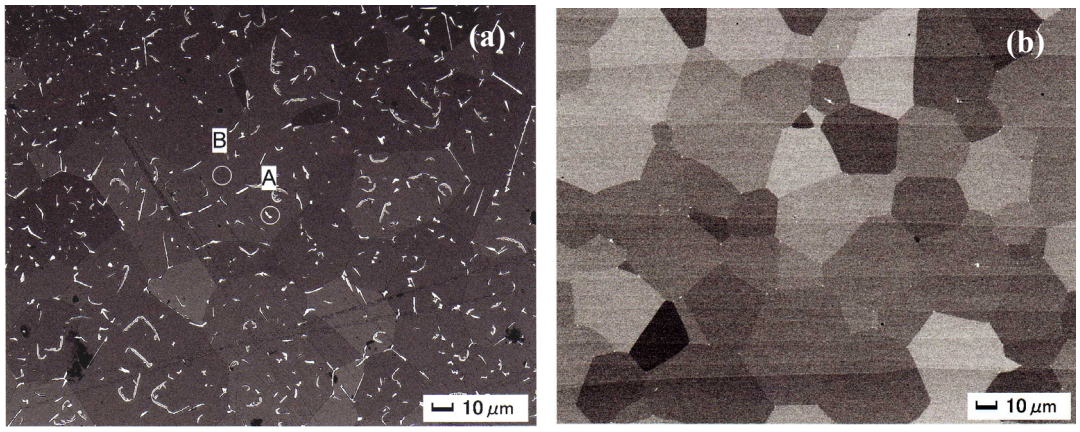


**Figure 5.24 (a)** Electron backscatter image of the yttria rich sample annealed at 1250 $^{o}$C for 36hrs. The composition of the areas marked A (precipitate) and B (matrix) were determined using WDS and are presented in Table **(b)** Appearance of the sample after 100 μm of material was removed using an Ar plasma cutter. The large amounts of precipitates seen on the surface are no longer present. Only very few areas of the second phase can be seen mainly at triple junctions between grains (white colored in the image

**Table 5.3** wt% compositions of the areas marked A and B in Figure 5.24 (a)

| | A (precipitate) wt% | B (matrix) wt% |
|---|---|---|
| C | 7.209 | 8.125 |
| O | 30.280 | 31.329 |
| Al | 17.053 | 23.308 |
| Si | 4.474 | - |
| Y | 38.790 | 35.663 |
| Nd | 2.195 | 1.575 |

\

### 5.4.4 Mechanical properties of second phases

Nanoindentation was also used to study the mechanical properties of second phases in YAG ceramics. For the ceramic used in this section, Si rich areas were present on the sample surface after the sintering process (Figure 5.25 (a)). After annealing of the sample at 1300 $^{o}$C for 6 and 36 hours no evolution of these areas was observed (Figure 5.25 (b)). The absence of strong crystalline facets and the Si rich composition of these second phases (Figure 5.26) pointed to their amorphous nature. Nanoindentation data were collected from both the YAG matrix and the second phase regions and the corresponding load displacement curves can be seen in Figure 5.27. In Table 5.4 the hardness and modulus of the YAG matrix and the second phases are presented. The second phases appear more compliant than the crystalline YAG which agrees with the assumption of their amorphous nature.

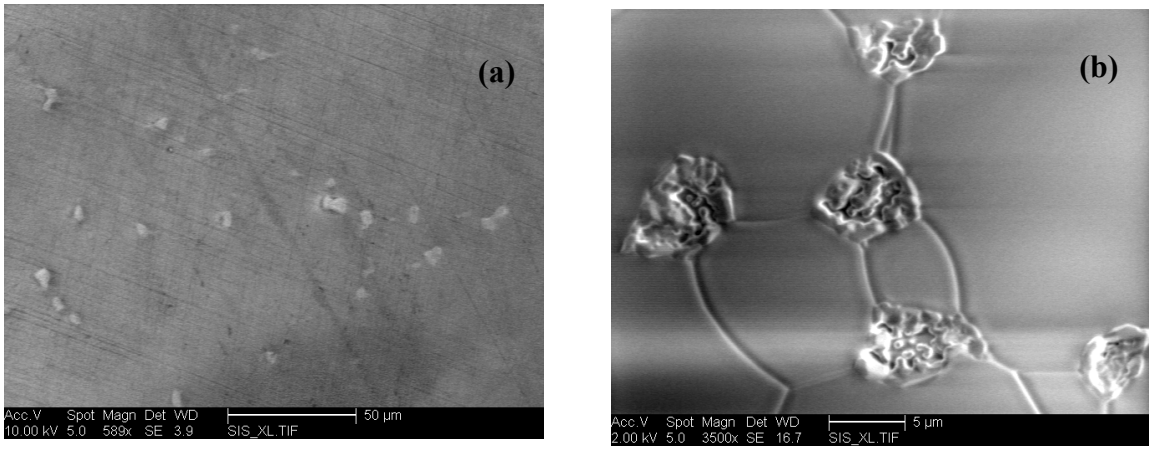


**Figure 5.25 (a)** The white contrast areas seen on the ceramic surface after sintering are Si rich **(b)** Second phases on the surface of the annealed sample.

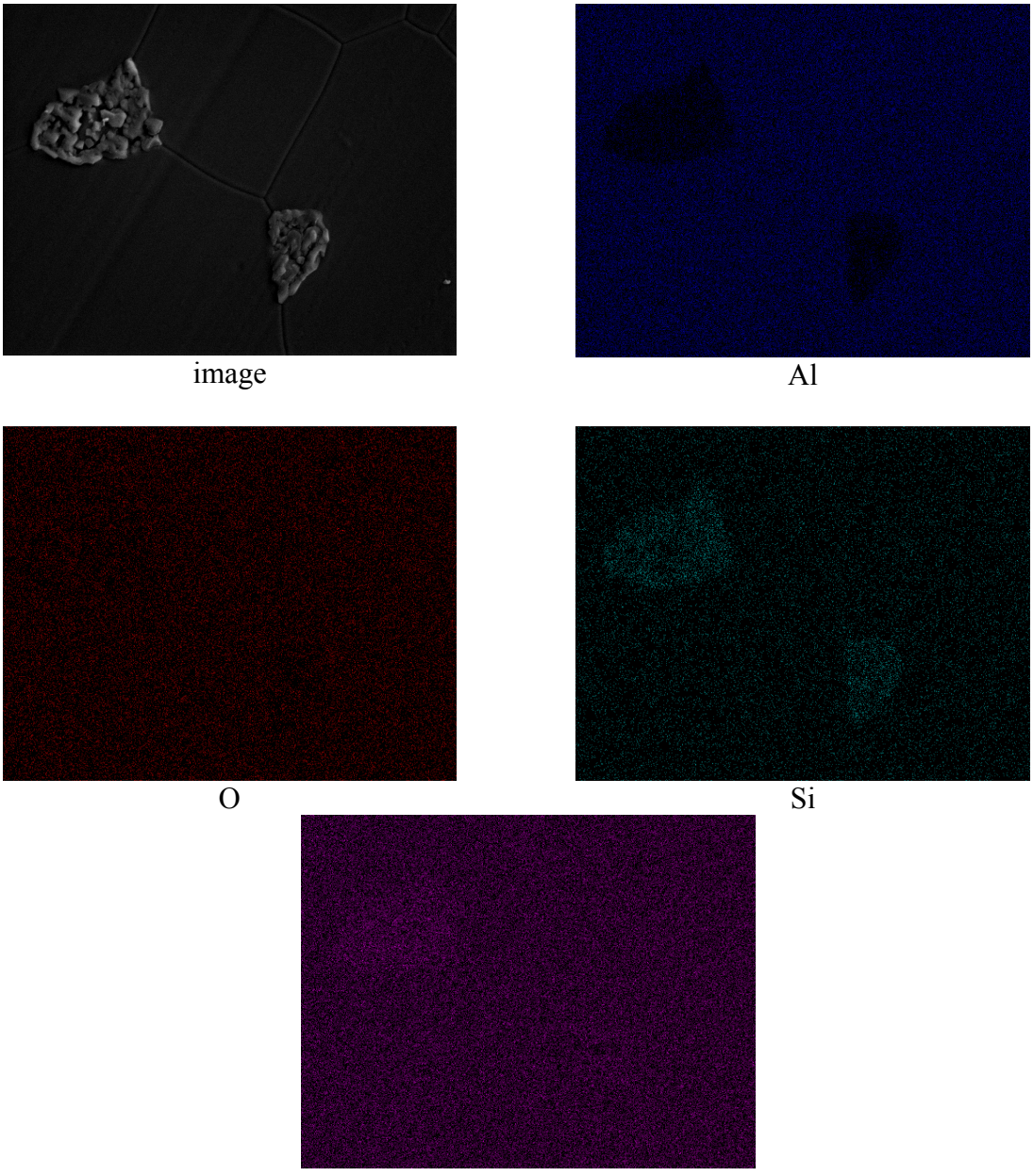


**Figure 5.26** EDS compositional maps reveal that the second phases are Si rich

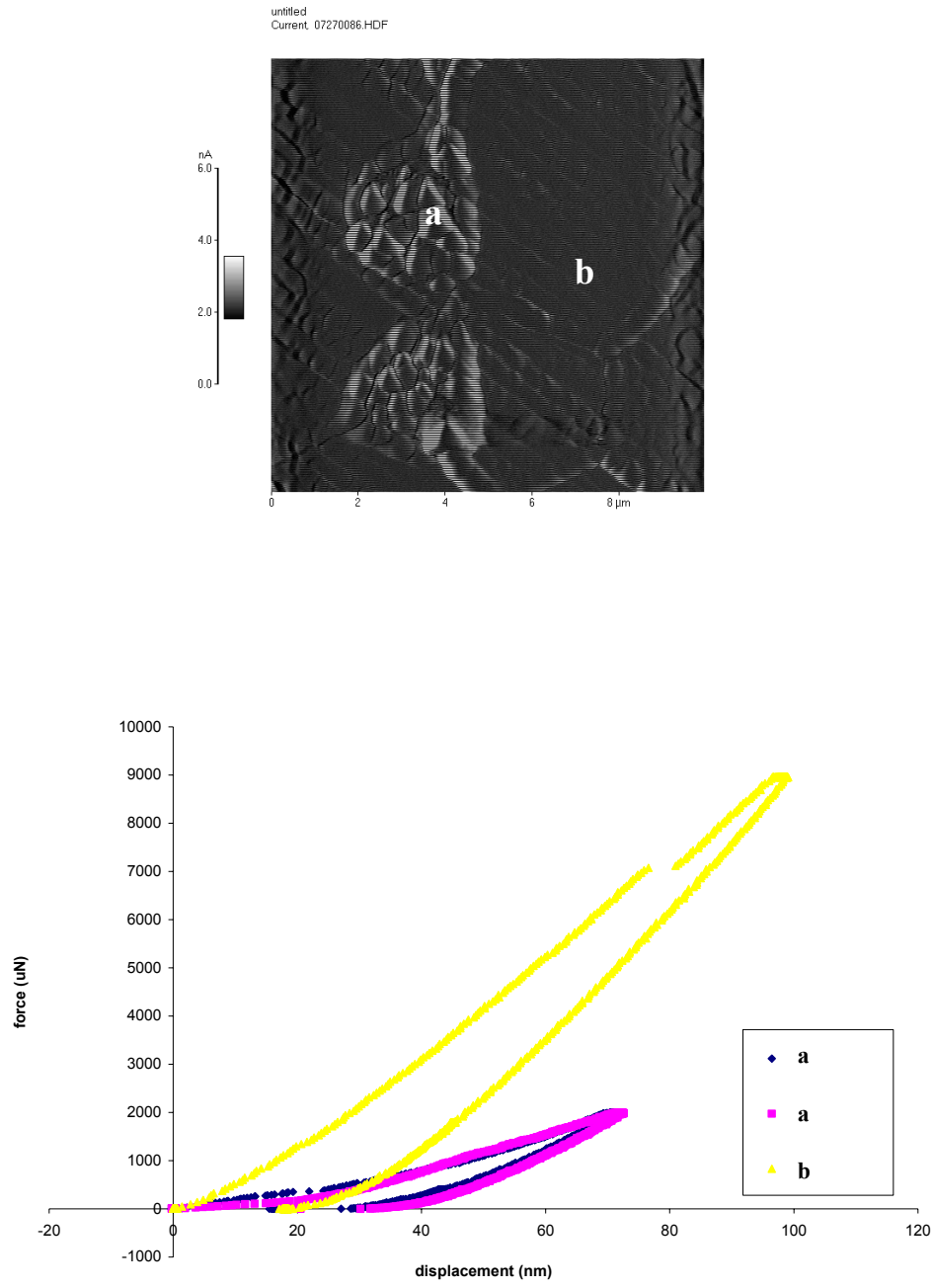


**Figure 5.27** Comparison of the load displacement curves taken from the second phase areas (marked a) and the YAG matrix (marked b)

**Table 5.4** Hardness and Elastic modulus of the YAG matrix and the second phases

| | **Reduced Young Modulus (GPa)** | **Hardness (GPa)** |
|---|---|---|
| Second phase | 200 GPA | 17.23 GPA |
| Second phase | 195 GPA | 17.23 GPA |
| YAG matrix | 376 GPA | 71.36 GPA |

## 5.5 Conclusions

This study has shown the importance of stoichiometry in the resulting microstructure. Small deviations in the concentrations of the initial powders used for the reactive sintering can cause large changes in the precipitation behavior and hence the performance of the ceramic as an active medium in a laser. Glassy phases in the samples were attributed to the use of sintering aids and were mainly located close to the free surface. Crystalline precipitates, on the other hand, were a result of the deviation from the YAG stoichiometry and formed throughout the volume of the samples. For samples where crystalline precipitates formed, longer post sintering annealing times increased their sizes with the growth following a square root type of dependency indicating that the process is diffusion controlled. Also in these cases longer annealing times seemed to mechanically strengthen the grain boundaries by possibly removing the thin glassy films from the interfaces. The precipitation behavior also showed a dependency on the processing temperatures used after sintering, with the same sample having a different microstructure after annealing at two distinct temperatures. The basic conclusion of this study is that the formation of second phases and precipitates which significantly affect the lasing

performance of the ceramics can be minimized by staying on stoichiometry and reducing the amount of sintering aids, namely silica, which are added to the initial powders.

## 5.6 References


**1.** "Progress in ceramic lasers" A. Ikesue, Y. L. Aung, T. Taira, T. Kamimura, K. Yoshida, G. L. Messing, Annu. Rev. Mater. Res. **36** 397 (2006)

**2.** "Laser fabrication and machining of materials" N. B. Dahotre, S. P. Harimkar, Springer Verlag (2007)

**3.** "Solid- state reactive sintering of transparent polycrystalline Nd: YAG ceramics" S.H. Lee, S. Kochawattana, G. L. Messing, J. Q. Dumm, G. Quarles, V. Castillo, J. Am. Ceram. Soc. **89** 1945 (2006)

**4.** "Progress in the YAG crystal growth technique for solid-state laser" T. Sekino, Y. Sogabe, Rev. Laser Eng. **21**(8) 827 (1995)

**5.** "The growth defects in Czochralski-grown Yb: YAG crystal" Y. Peizhi, D. Peizhen, Y. Zhiwen, T. Yulian, J. of Cryst. Growth **218** 87 (2000)

**6.** "Fabrication and optical properties of high- performance polycrystalline Nd: YAG ceramics for solid-state laser" A. Ikesue, T. Kinoshita , K. Kamata , K. Yoshida, J. Am. Ceram. Soc. **78**(4) 1033 (1995)

**7.** "Polycrystalline transparent YAG ceramics by a solid-state reaction method" A. Ikesue , I. Furusato , K. Kamata, J. Am. Ceram. Soc. **78**(1) 225 (1995)

**8.** "Effects of neodymium concentration on optical characteristics of polycrystalline Nd: YAG laser materials" A. Ikesue, K. Kamata, K. Yoshida, J. Am. Ceram. Soc. **79**(7) 1921–26 (1996)

**9.** "Neodymium doped yttrium aluminum garnet ($Y_3Al_5O_{12}$) nanocrystalline ceramics; a new generation of solid state laser and optical materials" J. R. Lu, K. Ueda, H. Yagi, T. Yanagitani, T. Akiyama, A. A. Kaminskii, J. Alloys Compounds **341** (1-2) 220 (2002)

**10.** "Transparent polycrystalline neodymium doped YAG: synthesis parameters, laser efficiency" Y. Rabinovitch, D. Tetard, M. D. Faucher, M. Pham-Thi, Opt. Mater. **24** (1-2) 345 (2003)

**11.** "Translucent $Y_3Al_5O_3$ ceramics" G.D. With, H.J.A. van Dijk, Mater. Res. Bull. **19** 1669 (1984 )

**12.** " Induced emission cross section of Nd: YAG ceramics" M. Sekita , H. Haneda , T. Yanagitani , S. Shirasaki , J. Appl. Phys. **67**(1) 453 (1990)

**13.** "The influence of MgO and $SiO_2$ dopants on the sintering behavior of yttrium aluminium garnet ceramics", W. Vrolijk, S. Van Dem Cruisem, R. Metselaar, Ceram. Trans. **51** 573 (1995)

**14.** "Role of Si on Nd solid-solution of YAG ceramics" A. Ikesue, K. Kamata, J. Jpn. Ceram. Soc. **103** (5) 489 (1995)

**15.** "Effect of silica on the reactive sintering of polycrystalline Nd:YAG ceramics" A. Maıtre, C. Salle, R. Boulesteix, J.-F. Baumard, Y. Rabinovitch, J. Am. Ceram. Soc. **91** (2) 406 (2008)

**16.** "Optical scattering centers in polycrystalline Nd:YAG laser", A. Ikesue, K. Yoshida, T. Yamamoto, I. Yamaga, J. Am. Ceram. Soc. **80** 1517 (1997)

**17.** " Decoloration of yttrium orthovanadate laser host crystals by annealing", Y. Nobe, H. Takashima, T. Katsumata, Optics Letters **19** 1215 (1994)

**18.** "Phase Diagrams for Ceramists", National Bureau of Standards, American Ceramic Society (1964)

**19.** "Grain boundaries in polycrystalline ceramics", D. R. Clarke, Ann. Rev. Mater. Sci. **17** 57 (1987)

**20.** "Phase Transformations in Metals and Alloys", D. Porter and K. Easterling, CRC Press (2000)

**21.** "Effect of composition on the oxygen tracer diffusion in transparent yttrium aluminium garnet (YAG) ceramics", I. Sakaguchi, H. Haneda, J. Tanaka, T. Yanagitani, J. Am. Ceram. Soc. **79** (6) 1627 (1996)

**22.** "Microstructural analysis of sintered high-conductivity zirconia with $Al_2O_3$ additions", E.P. Butler, J. Drennan, J. Am. Ceram. Soc. **65**(10) 474 (1982)

**23.** "$Yb_2O_3$- fluxed sintered silicon nitride", J. S. Vetrano, H.-J. Kleebe, E. Hampp, M. J. Hoffmann, M. Rohle, R. M. Cannon, Journal of Materials Science **28** 3529 (1993)

**24.** "Crystallization of the glassy phase in an $Si_3N_4$ material by post-sintering heat treatments" L. K. L. Falk, G. L. Dunlop, Journal of Materials Science **22** 4369 (1987)

**25.** " Glass/crystal interfaces in liquid-phase sintered materials", N. Ravishankar, C. B. Carter, Interface Science **8** 295 (2000)

**26.** "Exudation of silicate liquid from polycrystalline alumina", N. Ravishankar, J. K. Farrer, C. B. Carter, Mat. Res. Soc. Symp. Proc. **654** (2001)

**27.** "Exuding liquid from grain boundaries in alumina", N. Ravishankar, C. B. Carter, J. Am. Ceram. Soc. **84** (4) 859–62 (2001)

# Chapter Six: Conclusions and Recommendations for ceramic YAG crystals

This study has shown the importance of stoichiometry in the resulting microstructure. Small deviations in the concentrations of the initial nanopowders used for the reactive sintering can cause large changes in the precipitation behavior and hence the performance of the ceramic as an active medium in a laser. Glassy phases in the samples were attributed to the use of sintering aids and were mainly located close to the free surface. Crystalline precipitates on the other hand where a result of the deviation from the YAG stoichiometry and formed throughout the volume of the samples. For samples where crystalline precipitates formed, longer post sintering annealing times increased their sizes with the growth following a square root type of dependency indicating that the process is diffusion controlled. Also in these cases longer annealing times seemed to strengthen the grain boundaries by possibly removing the thin glassy films from the interfaces. The precipitation behavior also showed a dependency on the processing temperatures used after sintering, with the same sample having a different microstructure after annealing at two distinct temperatures. The basic conclusion of this investigation is that the formation of second phases and precipitates, which significantly affect the lasing performance of the ceramics, can be minimized by staying on stoichiometry and reducing the amount of sintering aids, namely silica, which are added to the initial powders.

# Appendix

# Complementary characterization techniques for identification of ferroelectric domains in $KNbO_3$ single crystals

*A. Bellou, D.F. Bahr**

*School of Mechanical and Materials Engineering, Washington State University, Pullman, WA, 99164, United States*

ARTICLE DATA

*Article history:*
Received 16 May 2007
Accepted 30 May 2007

*Keywords:*
Ferroelectric domains
$KNbO_3$
Optical crystals

ABSTRACT

$KNbO_3$ single crystals are often utilized for their piezoelectric and optical properties. In this study the domain configurations in as-grown single crystals were investigated using reflected light microscopy, scanning electron microscopy and atomic force microscopy. Using atomic force microscopy it was possible to image the distortion induced on the crystal surface by the domain walls and to quantify the predicted angle between $(001)_{pc}$ planes across these walls for the cases of both 90° domain walls and S walls. These features can also be imaged using the other two techniques. This direct measurement of surface distortion verifies the geometrical model of domain structures, and suggests that any possible strain energy considerations are minor in predicting the surface topography in the material after phase changes from the growth temperature.



## 1. Introduction

The properties of potassium niobate $KNbO_3$ make this ferroelectric crystal a very attractive material for nonlinear optical and electro-optical devices [1]. When $KNbO_3$ crystals are cooled from high temperatures to room temperature during crystal growth, they undergo the following phase transformations: from cubic (Pm3m) to tetragonal (P4mm2) at a temperature of 438 °C and from tetragonal to orthorhombic (Bmm2) at a temperature of 234 °C [2]. At the cubic-to-tetragonal transition the atoms are displaced from their initial positions in the cubic cell, generating a spontaneous polarization along one of the cube edges [3]. When the temperature is further lowered the second transition (to the orthorhombic structure) occurs and again the atoms in the unit cell are displaced. This displacement causes a change in the spontaneous polarization, which will now lie along one of the face diagonals of the original cube [4]. Since there are a number of possible directions for the spontaneous polarization, different domains appear in the crystal. The existence of these domains affects the quality of the grown crystals and their removal, by a poling process, is necessary if the crystal is to be used for optical applications [5]. On the other hand, the piezoelectric properties of the crystals can be improved by the presence of domains [6]. In either case, the domain configurations influence the properties of the material; therefore the investigation of these domains is necessary for a better understanding of the material's performance.

The low temperature orthorhombic unit cell of $KNbO_3$ can be described as a distortion of the cubic cell and commonly the directions and planes in the orthorhombic phase refer to the axes of the original cube [4,5]. In the orthorhombic phase the polarization vector lies along one of the face diagonals of the original cube so a number of domains can exist with the angles between polarization vectors of adjacent domains being 60°, 90°, 120° and 180° [5]. The boundaries between adjacent domains are called domain walls and their possible orientations have been determined theoretically by taking into account the condition for mechanical compatibility between adjacent domains [5,7]. The domains can be described as twinned areas in the crystal with the domain walls being the twinning planes. For the case of 90° domains the domain walls are oriented parallel to the $\{001\}_{pc}$ planes, whereas in the case of 60° domains their orientation is parallel

* *Corresponding author*. Tel.: +1 509 335 8523; fax: +1 509 335 4662.
*E-mail address:* dbahr@wsu.edu (D.F. Bahr).

1044-5803/$ – see front matter © 2007 Elsevier Inc. All rights reserved.
doi:10.1016/j.matchar.2007.05.024

to the $\{110\}_{pc}$ planes [4]. The subscript pc indicates that the orientations refer to the original (prior) cubic cell. In addition to these commonly observed walls an S wall can appear [5,7]. S walls can form in the case of 60° and 120° domains instead of $\{110\}_{pc}$ walls. Among the reported indices for S walls are $(1,1,0.31)_{pc}$ $(1,–1,0.31)_{pc}$ and $(1,–0.3,1)_{pc}$ $(1,0.3,1)_{pc}$ [5,7], respectively. S walls appear in configurations that involve two types of 90° domains with polarization vectors lying in perpendicular planes.

Deshmukh and Ingle [4] have studied surface deformations in $KNbO_3$ on the pseudocubic (001) planes, which are caused by the domain structures, using interferometry, in the same manner that Bhide and Bapat had done previously for single crystals of barium titanate ($BaTiO_3$) [8]. These surface distortions are generated by the lattice matching of the adjacent domains. In the case of 90° domains they measured an angle of approximately 0.5° between pseudocubic (001) planes across the domain wall, which was in agreement with the theoretically calculated value. For the case of 60° domains this angle was found to be approximately 0.95°, also in agreement with that calculated from the lattice parameters. For complex domain structures, involving 60° domain walls, this value was found to be twice the 0.95° value. Wiessendanger [7] has reported an angle of 0.97° between $(001)_{pc}$ planes of adjacent domains across S walls. However, with any optical technique in $KNbO_3$ the possible differences in refractive index suggest it is prudent to compare the inferred to direct measurements when possible.

In this paper the domains present in the stable room temperature orthorhombic phase of potassium niobate were investigated using three complementary characterization techniques: optical microscopy, scanning electron microscopy and atomic force microscopy. Using the atomic force microscope we were able to measure the values of the angles between surfaces of adjacent domains which were found to be in agreement with the theoretical values as well as with values measured using interferometric techniques.

## 2. Experimental Details

The three samples that were investigated were cut from a commercially acquired $KNbO_3$ single crystal in such a way that their surfaces were parallel to the pseudocubic (001) planes. The surface of one of the three samples was mechanically ground with SiC papers and polished with alumina and finally polished to a 50 nm finish with colloidal silica, while the surfaces of the two other samples were not further treated.

Characterization of the samples used three primary techniques. First, optical microscopy was carried out using an Olympus MG optical microscope. Scanning electron microscopy micrographs were acquired by a Sirion Field Emission Scanning Electron Microscope (FEI Corp.) using secondary electron imaging. Attempts at using orientation imaging microscopy were not successful because of the extremely small (<1°) orientation differences at the domain boundaries. The surface topography was investigated using atomic force microscopy with a Park Autoprobe CP scanning probe microscope. The scans were performed at room temperature and the contact mode was used with a NP-S tip.

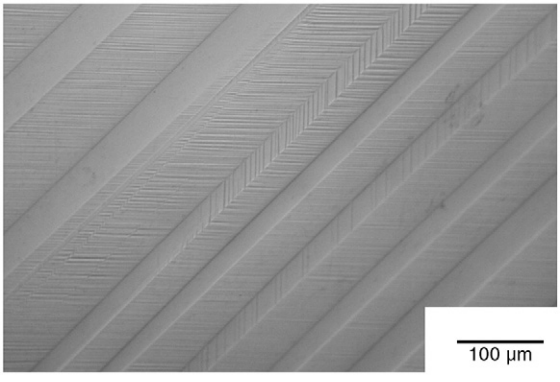


**Fig. 1 – Domain configurations on a mechanically polished $KNbO_3$ sample viewed under ordinary light.**

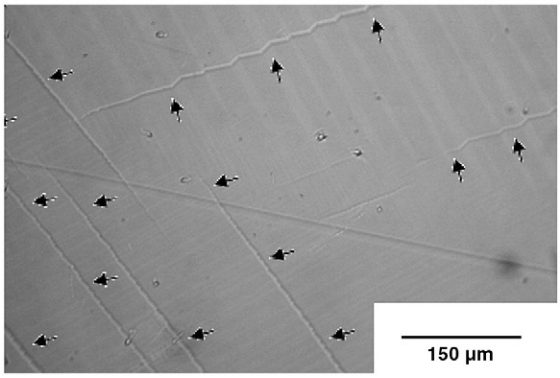


**Fig. 2 – Domain configurations observed with ordinary light, including the S wall structures which run diagonally across this image (noted with arrows). This sample was not mechanically polished.**

## 3. Experimental Results and Discussion

All types of domain walls can be observed optically, with the exception of 180° domain walls, because there is a change of refractive index at the walls [5]. Figs. 1 and 2 show micrographs obtained using a light microscope, where complex domain configurations can be observed. The micrograph in Fig. 1 shows the surface of the mechanically polished sample, whereas that in Fig. 2 shows part of the surface of an unpolished sample. In Fig. 2, S walls can be seen running diagonally on the surface of the sample.

The sample whose surface was mechanically polished was also examined using SEM. This allowed the observation of domain configurations with a higher resolution than that achieved with the light microscope. The micrograph in Fig. 3 shows a complex domain configuration, whereas in Fig. 4 a domain configuration that involves 90° domain walls and S walls can be seen. Even after mechanical polishing, the topographical features on the surface can be clearly identified. With optical microscopy it is possible to resolve the domains

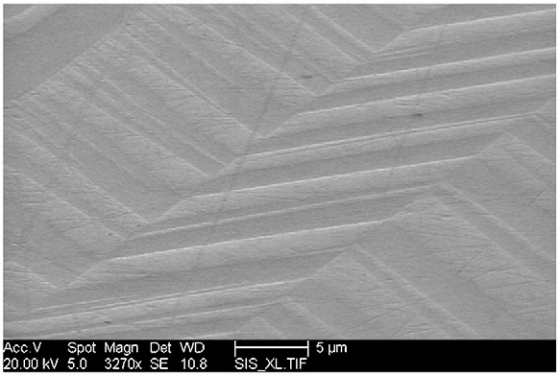


**Fig. 3 – Complex domain patterns on the surface of a mechanically polished sample observed with the SEM.**

due to differences in refractive index, but this is not a viable contrast mechanism for SEM. Therefore it is clear that, even after polishing, the single crystal surfaces are deformed either to relieve elastic strain via surface topography changes, or that the domain structures polish at a different rate, and that surface topography may play a role in the structure of finished optical devices.

Because the topography is obviously influenced by the domain structure, quantifying this would aid in further characterization. Atomic force microscopy can be used to study the surface morphology of materials with high topographical resolution. It has been reported that the appearance of domains causes distortions on the as-grown surfaces of potassium niobate [4]. Atomic force microscopy has been used to investigate surface distortions caused by the presence of domain configurations in other ferroelectric materials like $BaTiO_3$ and $PbTiO_3$ [9–12]. For this investigation the samples with the as-grown surface that did not undergo any mechanical treatment were used to examine the topography induced on the pseudocubic (001) planes after the phase transformations and the resultant generation of ferroelectric domains. Surface distortions and topography were present on the polished sample, but the exact topographic features were less distinct, and therefore for this paper we present only the

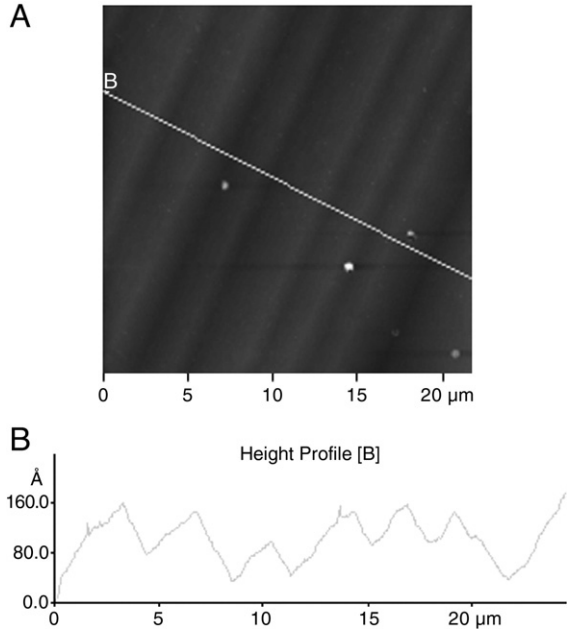


**Fig. 5 – (A) Topography of 90° domains. (B) Cross sectional profile along the line marked in (A).**

quantified angles on the as-grown surfaces. Other researchers have noted similar surface distortions after etching lead titanate crystals, where the cross-sectional profiles exhibit rounded areas [10]. Therefore, polishing with colloidal silica clearly alters but does not remove the original surface topography of the sample.

Fig. 5(A) is an atomic force microscopy image that shows the topography of an area where parallel stripes of 90° domains appear. The cross sectional profile along the line drawn in Fig. 5(A) reveals a zig-zag surface distortion (Fig. 5(B)), with an average angle, $\theta$, of 0.53° between the planes of adjacent domains. This correlates well with the theoretically calculated value of 0.5° as well as the angle measured by Deshmukh and Ingle [4]. It should be noted here that the angles between planes of adjacent domains appear exaggerated in the cross-sectional profiles due to the different scales used for the horizontal and perpendicular axes.

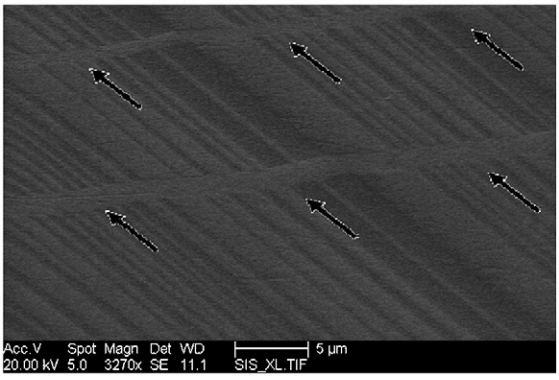


**Fig. 4 – Scanning electron microscopy micrograph of a mechanically polished sample, showing both 90° domains and the S wall structures (S walls are denoted with arrows).**

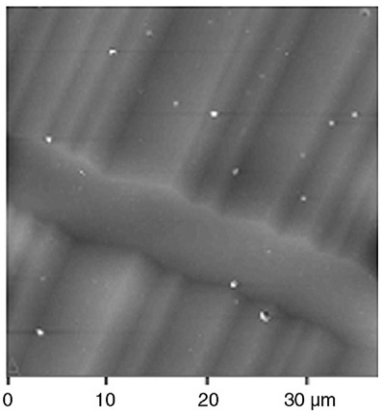


**Fig. 6 – Simple arrangement involving S walls.**

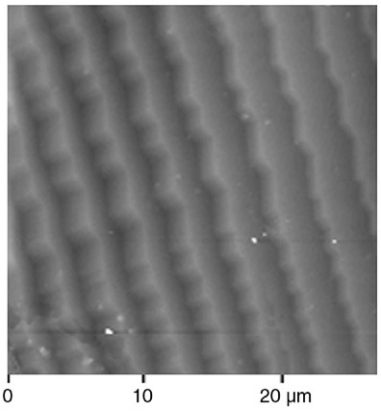


**Fig. 7 – Domain configuration involving regularly spaced S walls.**

Two distinct configurations involving S walls were observed in the as-grown crystals. The first was a simple arrangement involving S walls, as the one shown in Fig. 6. The second configuration involved regularly space S walls as seen in Fig. 7.

Fig. 8 shows an atomic force microscopy image obtained by scanning a smaller portion of the area presented in Fig. 7. The 90° domains involved in this configuration can have their polarization vectors lying either on the $(001)_{pc}$ plane, which is the plane of observation, or on the $(100)_{pc}$ plane, which is perpendicular to the plane of observation. Both sets of 90° domains share essentially the same 90° domain walls, which are parallel to the $(010)_{pc}$ planes. However, in the first case no surface distortion is observed across the domain walls, since the plane of observation is the shear plane [4], whereas a surface distortion is observed for the latter case. Two adjacent 90° domains that belong to different sets have their polarization vectors lying in perpendicular planes and the angle between these vectors is 60°. S walls are the boundaries between these domains and appear as zig-zag lines on the plane of observation.

In Fig. 9(A) the topography of the area containing regularly spaced S walls is presented. The cross sectional profile along line A, shown in Fig. 9(B), reveals the zig-zag surface distortion across S walls. Similarly, in Fig. 9(C) the cross sectional profile along line C, reveals the zig-zag surface distortion caused by the 90° domains, with polarization vectors lying on the $(100)_{pc}$ plane which is perpendicular to the plane of observation. By measuring the angle $\theta$ between $(001)_{pc}$ planes of adjacent domains across S walls, an average angle of 0.933° was found, in very good agreement with the theoretical value of 0.95° and the value of 0.97° previously reported [4,7]. The average angle between the $(001)_{pc}$ planes across 90° walls, for this configuration, was 0.516°, again in very good agreement with the

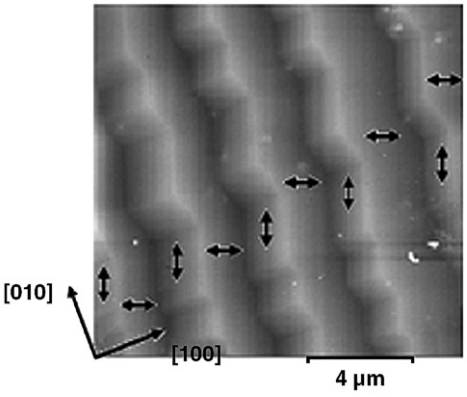


**Fig. 8 – Atomic force microscopy image where S walls and 90° domains can be seen on the $(001)_{pc}$ plane (plane of observation). The zig-zag lines are the projection of S walls on the $(001)_{pc}$ plane. The areas situated between these zig-zag lines are the 90° domains. The lines parallel to the $[100]_{pc}$ direction are the projection of 90° domain walls, which are parallel to the $(010)_{pc}$ planes, on the plane of observation. For both types of 90° domains, polarization vectors of adjacent domains are at right angles. The ↕ symbol denotes the 90° domains for which these vectors lie on the $(100)_{pc}$ planes, whereas the ↔ symbol denotes the 90° domains for which the polarization vectors lie on the $(001)_{pc}$ planes. For the latter case no distortion is generated on the surface and hence these areas show no topography.**

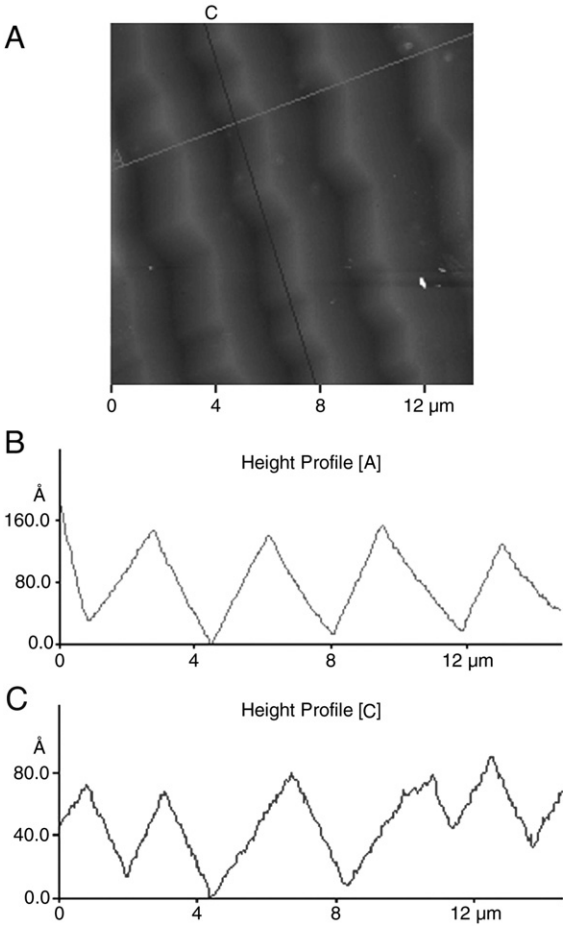


**Fig. 9 – (A) Topography of an area containing regularly spaced S walls. (B) Cross sectional profile along line A. (C) Cross sectional profile along line C.**

theoretical value of 0.5° and values previously measured [4]. The domain thicknesses in all the above cases were on the order of $10^{-6}$ m, in accordance with previously reported values for 60° and 90° domains [13,14].

The previous predictions [4] of domain structures are based solely on geometric analysis, and ignore the contribution of strain energy which may occur during polarization. Based on the similarity between the precise atomic force microscopy measurements of domain structures and the theoretical predictions, it appears that strain energy due to domain formation provides a minimal contribution to the resulting structures.

## 4. Conclusions

In this study the domain configurations that appear in $KNbO_3$ were investigated with three complementary characterization techniques: reflective optical microscopy, atomic force microscopy, and scanning electron microscopy. All three are able to distinguish domain structures, and can be used in both as-grown samples as well as for materials which have been subsequently processed using mechanical polishing. The domain features persist after polishing through a 50 nm colloidal silica finish. Using atomic force microscopy the angles between $(001)_{pc}$ planes across domain walls were measured. The angles found for the cases of 90° walls and S walls were in good accordance with the theoretical values, which have been calculated using geometrical considerations ignoring the contribution of strain energy to the final domain configurations. Based on the similarity between the precise atomic force microscopy measurements of domain structures and the theoretical predictions, it appears that strain energy due to domain formation provides a minimal contribution to the resulting structures.

The use of complementary techniques allows for flexibility for characterizing domain densities in this material with subsequent processing or device fabrication.

## Acknowledgements

We wish to thank VLOC Inc., a subsidiary of II–VI Inc., for providing the samples used in this study.

## REFERENCES

[1] Zgonik M, Schlesser R, Biaggio I, Voit E, Tscherry J, Gunter P. Materials constants of $KNbO_3$ relevant for electro- and acousto-optics. J Appl Phys 1993;74:1287–97.
[2] Popoola OO, Kriven WM. In-situ transmission electron microscopy study of phase transformations in $KNbO_3$ perovskite. Philos Mag Lett 1997;75:1–5.
[3] Hewat AW. Cubic-tetragonal-orthorhombic-rhombohedral ferroelectric transitions in perovskite potassium niobate: neutron powder profile refinement of the structures. J Phys C Solid State Phys 1973;6:2559–72.
[4] Deshmukh KG, Ingle SG. Interferometric studies of domain structures in potassium niobate single crystals. J Phys D Appl Phys 1971;4:124–32.
[5] Jarman RH, Johnson BC. Characteristics of domain formation and poling in potassium niobate. Proc SPIE Int Soc Opt Eng 1991;1561:33–42.
[6] Wada S, Murakoa K, Kakemoto H, Tsurumi T, Kumagai H. Enhanced piezoelectric properties of potassium niobate single crystals with fine engineered domain configurations. Mater Sci Eng B Solid-State Mater Adv Technol 2005;120:186–9.
[7] Wiessendanger E. Domain structures in orthorhombic $KNbO_3$ and characterization of single domain crystals. Czech J Phys 1973;B 23:91–9.
[8] Bhide VG, Bapat NJ. Interferometric study of the microtopography arising out of 90° domain walls in single crystals of barium titanate. J Appl Phys 1963;34:181–8.
[9] Balakumar S, Xu JB, Ma JX, Ganesamoorthy S, Wilson IH. Surface morphology of ferroelectric domains in $BaTiO_3$ single crystals: an atomic force microscopy study. Jpn J Appl Phys 1997;36:5566–9.
[10] Wang YG, Dec J, Kleemann W. Study on surface and domain structures of $PbTiO_3$ crystals by atomic force microscopy. J Appl Phys 1998;84:6795–9.
[11] Takashige M, Hamazaki S, Fukurai N, Shimizu F, Kojima S. Atomic force microscope observation of ferroelectrics: barium titanate and Rochelle salt. Jpn J Appl Phys 1996;35:5181–4.
[12] Pang GKH, Bada-Kishi KZ. Characterization of butterfly single crystals of $BaTiO_3$ by atomic force, optical and scanning electron microscopy techniques. J Phys D Appl Phys 1998;31:2846–53.
[13] Ingle SG, Dutta HS, David AP. Domain wall nucleation by impurity ions in $KNbO_3$ single crystals. J Appl Phys 1988;64:4640–5.
[14] Lian L, Chong TC, Kumagai H, Hirano M, Taijing L, Ng SC. Temperature evolution of domains in potassium niobate single crystals. J Appl Phys 1996;80:376–81.

Journal of Crystal Growth 311 (2009) 1496–1500

Contents lists available at ScienceDirect

Journal of Crystal Growth

journal homepage: www.elsevier.com/locate/jcrysgro

# Microstructure and grain growth of polycrystalline silicon grown in fluidized bed reactors

M.M. Dahl [a], A. Bellou [a], D.F. Bahr [a,*], M.G. Norton [a], E.W. Osborne [b]

[a] School of Mechanical and Materials Engineering, Washington State University, Pullman, WA 99164, United States
[b] REC Silicon, Moses Lake, WA 98837, United States

ARTICLE INFO

*Article history:*
Received 6 January 2009
Accepted 16 January 2009
Communicated by R. Kern
Available online 25 January 2009

*PACS:*
61.66.Bi
61.72.uf
61.72.Qq

*Keywords:*
A1. Characterization
B1. Polysilicon
B3. Solar cells

ABSTRACT

Fluidized bed technology is being implemented commercially to produce polycrystalline silicon that is used as a precursor for silicon ingot growth for the photovoltaic industry. The fluidized bed reactor produces polysilicon in a granular form, usually at lower temperatures than the traditional Siemens process. This current study documents for the first time grain growth and mechanical properties of polysilicon grown via a fluidized bed. In the as-grown state the granules produced by the fluidized bed reactor consist of equiaxed grains that are approximately 30 nm in diameter. Annealing at temperatures above 1000 °C causes significant grain growth to occur resulting in grains up to 300 nm. The hardness of the granular material was 10% less than that of single crystal silicon, which can be attributed to grain boundary sliding. Understanding the effect of annealing on microstructure, grain growth, and mechanical properties of the granules is critical for establishing appropriate techniques for handling the material.



## 1. Introduction

Polycrystalline silicon is the base material used in the production of single crystal silicon for the semiconductor industry and for the rapidly growing photovoltaic (PV) market. The most common source of polycrystalline silicon (polysilicon) has traditionally been via chemical vapor deposition (CVD) in Siemens-style reactors [1], in which silane or trichlorosilane is decomposed on the surface of a seed rod in which the surface temperature is controlled by internal resistance heating of the rod. This technique requires expensive capital equipment, may have high operating costs, often produces low silicon yield (up to 60% from the gas in theory, but only 15–30% in practice), and generates the release of highly corrosive hydrogen chloride, further adding to capital expense [1].

The rapid increase in demand for silicon for PV use has surpassed the demand in the microelectronic industry in recent years and has stimulated the need for a more cost-effective method to produce larger quantities of polysilicon [2,3]. One method that is gaining popularity is the fluidized bed reactor (FBR) that produces silicon in the form of granules instead of the traditional rods. The purity level of the granular material may be lower than that grown by the Siemens process, but this appears to be acceptable for the PV market. Fluidized bed technology for silicon production has been noted experimentally since the 1980s, but has not been commercially utilized until much more recently.

Fluidized bed reactors produce granular silicon by pyrolytic decomposition of silane-containing gases. The process has been described in detail elsewhere e.g., [2,3] and begins with silicon seed particles ranging from 100 to 2000 μm in diameter [1,4] that are fluidized with a carrier gas such as hydrogen. An important and significant aspect of the FBR is the lower temperature range that is used to produce silicon. Gas decomposition can be achieved at temperatures as low as 600 °C, as opposed to temperatures of up to 1200 °C that are used in the Siemens process [5]. Once a certain size range is achieved within the reactor, the granules fall to the bottom, where they are collected, without disrupting the growth of the rest of the material. The advantages of the FBR are the lower energy requirements and, because it is a continuous process with the ability to recycle the feed gasses, very high yields are possible.

Due to the increase in use of FBRs, a better understanding of the granule growth mechanisms and the microstructure and properties of the resulting material is required. These data are available in the literature for bulk polysilicon and thin films [6–8], but there is currently no available information on the microstructure, properties, and subsequent grain growth mechanisms of silicon granules fabricated in the FBR.

* Corresponding author.
*E-mail address:* dbahr@wsu.edu (D.F. Bahr).

0022-0248/$ - see front matter © 2009 Elsevier B.V. All rights reserved.
doi:10.1016/j.jcrysgro.2009.01.114

In this current study, granules grown in the FBR from REC Silicon have been analyzed to determine the structure and morphology of the silicon product. Optical and electron microscopy, X-ray diffraction, and nanoindentation were used to determine grain size, structure, and mechanical properties, respectively. Samples were also annealed at temperatures ranging from 800 to 1100 °C to determine the effect of post growth heat treatment on microstructure and mechanical properties of the granules.

## 2. Experimental procedure

The fluidized bed apparatus, as previously described in the literature, consists of a cylindrical reactor constructed of stainless steel with an inner diameter approximately 13 cm and a height of approximately 160 cm. An expansion zone located at the top of the reactor is roughly twice the diameter of the lower half and is used to allow the particles to drop back into the bed [2,9]. The chamber is heated with an external heater to a temperature between 650 and 750 °C; the temperature varies along the column height. Gas inlets are located at the bottom of the reactor and the flow of process gasses, hydrogen and silane, is controlled by controlling the inlet mass flow conditions. The gasses are pre-heated to a temperature below silane pyrolysis before being injected into the reactor [2]. Sub-mm seed particles of silicon to act as nucleation sites are added to the reactor during the growth process. Silane concentrations of the feed gas between 10% and 60% by volume (with the balance $H_2$) have been tested [9]; the samples used in this current study are from intermediate silane concentrations in this range. Additionally, the concentration profile of silane most likely changes in the reactor as a function of column height as silicon is deposited and hydrogen is released. The reactor is kept fluidized by the use of multilayer screens. A mesh screen is supported by a thin stainless steel plate punctured with 0.5 mm holes [9]. Fine particles are collected at the top of the reactor by passing through filters and cyclones, and the feed gas can be recycled in the process. Granular material is grown from the seed material for approximately one day in the reactor before reaching the predetermined size of particles used in this current study.

Specimens of granular polysilicon collected from REC Silicon were prepared for optical microscopy by conventional metallographic grinding and polishing. The polished samples were etched with an isotropic "HNA" solution composed of 8% hydrofluoric acid, 25% nitric acid, and 67% acetic acid by volume. Samples were etched with a cotton swab for roughly 1 min until the surface darkened slightly and the macrostructure became apparent, and then rinsed with deionized water. Optical images were captured and measurements of the macrostructural features were recorded. Unlike bulk polycrystalline material grown via the Siemens process, the etchant does not reveal the fine sub-μm grain structure; therefore X-ray diffraction was used on powdered granules to determine the average grain size using the Hall–Williamson equation [10]

$$B\cos\theta = \frac{k\lambda}{D} + \eta\sin\theta \quad (1)$$

where $B$ is the peak width difference, $k$ is a constant (~1), $\lambda$ is the X-ray wavelength, $\eta$ is the strain, and $D$ is the average grain size.

Samples were prepared for scanning electron microscopy (SEM; FEI Sirion operated at 20 keV) by fracturing the samples with a Rockwell hardness tester. Structures, such as internal pores were strongly influenced by the polishing process; the fractured surface produced more reproducible images of the pores and the peripheral fine grain structure. Samples were prepared for transmission electron microscopy (TEM; JEOL 1200 HR operated at 200 keV) by mechanical diamond polishing to 0.25 μm and dimpling using a VCR 500i Dimpler. Electron transparency was achieved with a VCR ion mill using 5 keV argon ions. Annealing of the samples was carried out in an open platinum crucible that was heated to 800 °C at 8 °C/min and then at a rate of 4 °C/min to the final annealing temperatures of 800–1100 °C. The annealed samples were held at the peak temperature for 6 h and then furnace cooled.

The mechanical properties were measured using a Hysitron Triboscope nanoindentation system in conjunction with a Park Autoprobe CP scanning probe microscope. Indentations were carried out on granular material ground with SiC to a 600 grit finish, and polished to a 0.25 μm finish using diamond polishing compound. The polished surface was imaged using the scanning probe system, and pore-free regions of the surface were selected for indentation. Indentations were carried out using a fixed 10 s loading, 10 s hold, and 10 s unload, with a 5 s hold for drift correction, to maximum loads between 4000 and 9500 mN. The unloading slope was analyzed using the Oliver and Pharr method [11] to determine the elastic modulus and hardness of the material. In addition to the granular material, (0 0 1)-oriented single crystals of silicon were indented for comparison purposes under the same loading conditions.

## 3. Results and discussion

### 3.1. Microstructure and porosity in as-grown material

Macroscopically, the sectioned granules show a series of concentric rings (Fig. 1). The ring structure is evident because of porosity differences within the granule; this suggests multiple growth layers. The darker contrast rings in Fig. 1 represent regions of higher porosity, while dark radial stripes are due to cracks that were either formed during growth or sample preparation. A more detailed examination of many of these images reveals that each layer has approximately the same radial distance and that all specimens examined share comparable ring dimensions (Fig. 2A). There is a roughly linear relationship between the numbers of rings found in a granule versus the granule diameter (Fig. 2B)

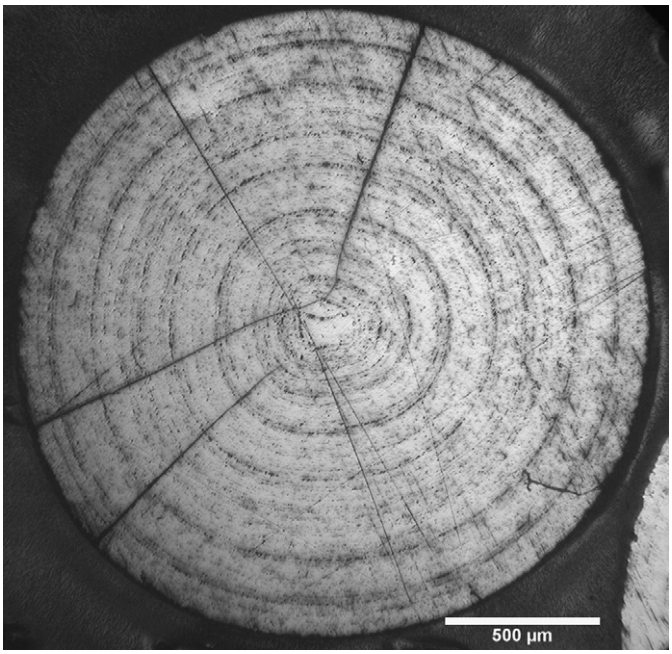


**Fig. 1.** Optical micrograph of etched silicon granule.

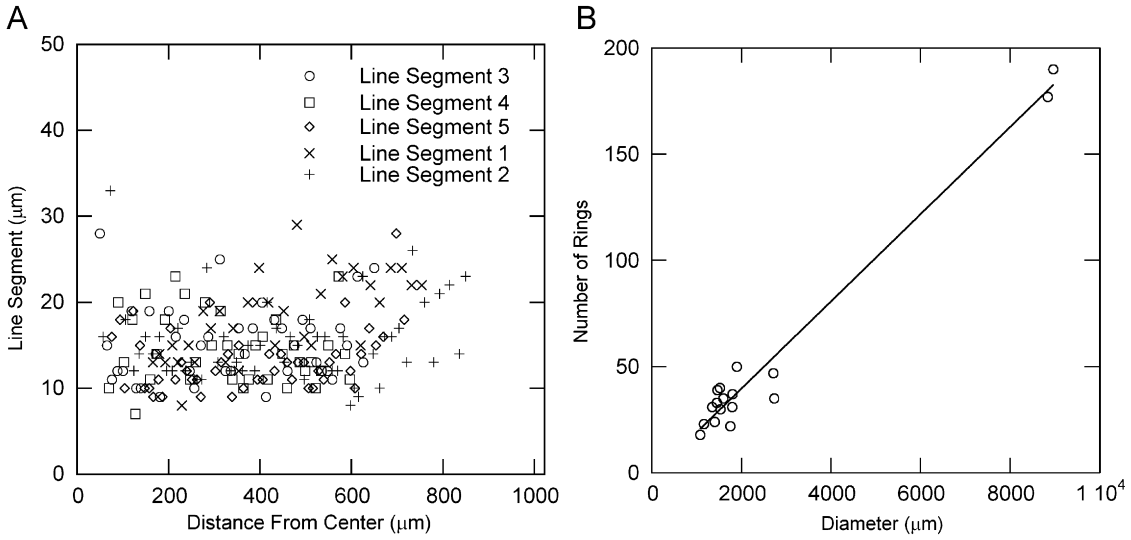


**Fig. 2.** (A) Layer thickness versus distance from the center of the granule. Each layer is approximately the same thickness. (B) Number of rings versus diameter of granule. Linear trend signifies similar growth rates for all granules.

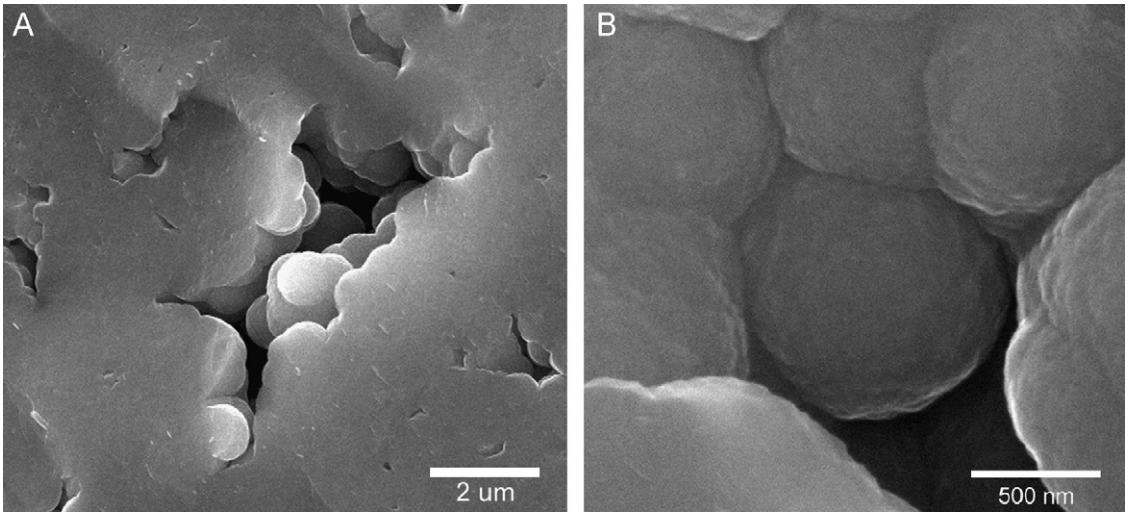


**Fig. 3.** (A) Pore in an as grown sample. Average pore size is approximately 5 μm. (B) Higher magnification image showing texturing of grains around the pore.

suggesting that the radial growth rate is constant. The similar layer thicknesses indicates that the deposition process is limited by surface area and not by the quantity of silicon-containing gas or time spent during growth of an individual ring; either of these processes would lead to thinner rings around the exterior of the granule to create similar volumes of material per growth period. Samples grown under a wide range of processing conditions exhibited the porous structures, suggesting these morphological structures are likely suggestive of granular silicon grown via the FBR method. As particulate matter in an FBR will cycle through the height of the column during growth, we suspect these rings containing a relatively high density of voids are linked to the cyclic nature of the growth. However, we do not have direct evidence of where in the growth cycle these voids form, as there is an unmeasured temperature and concentration gradient in the growth chamber.

The detail of the pore structure within the rings exhibiting the darker contrast was examined using SEM. In the as-received state, the pores are bounded by spherical particles approximately 0.5 to 1 μm in diameter, as seen in Fig. 3A. At higher magnification, Fig. 3B shows that the spheres are textured on the nanolevel. This is consistent with the average grain size within the granular of 30 nm measured with XRD, as described in the next section.

### 3.2. Grain size and growth

Grain sizes measured for samples annealed up to 1000 °C are shown in Table 1. No significant grain growth is observed until 1000 °C. Beyond 1000 °C, abnormal grain growth leading to a non-Gaussian grain size distribution makes the use of the Hall–Williamson analysis inappropriate for quantifying grain size.

Annealing the granules at 1100 °C caused an obvious change in the appearance of the pores. The grains around the pores became faceted as illustrated in Fig. 4. This observation suggests that atomic mobility is sufficient to lower the overall surface energy of the grains. Grain growth mechanism changes have also been noted to begin in polysilicon thick films at similar temperatures and are theorized to be a result of a shift of driving force to surface energy anisotropy [12].

Figs. 5A and B show the grain structure of samples annealed at 1100 °C. The images are of fine grained silicon and a large, abnormal grain surrounded by fine grains, respectively. It is noted in Fig. 5A that after annealing at 1100 °C there are still very fine grains less than 20 nm in diameter even though there is an overall increase in grain size as the annealing temperature is increased. The abnormal grains ranged from 200 to 500 nm in diameter. The presence of abnormal grains indicates secondary grain growth in samples annealed at the higher temperatures used in this study. It should be noted that both the secondary grains as well as the primary grains are heavily twinned. In appearance, the grain growth seems to be similar to that seen in polycrystalline thin [6] and thick films grown via CVD and plasma-enhanced CVD; however the driving force is most likely related to grain boundary energy reduction as seen in bulk systems and less dependent on surface energy as would be expected in thin film growth. Abnormal grain growth in polysilicon thin films is driven by the surface energy reduction of large columnar grains [7]; however, grain growth in thick films that does not depend upon the columnar grain structure has been investigated to produce abnormal grain growth by other means [12]. For example, other studies at high temperatures (above 1040 °C) and shorter times (approximately 30 min), have shown secondary grain growth and attributed it to coalescence due to dislocation climb in grain boundaries. At longer times, grain growth appears to be attributed to surface energy anisotropy [12] and the newly formed secondary grains continue to grow at a faster rate than the regular sized grains.

**Table 1**
Average grain size after annealing at various temperatures for 6 h.

| Annealing temperature (°C) | Average grain size (nm) |
|---|---|
| As-received | 30 |
| 800 | 22 |
| 900 | 38 |
| 1000 | 77 |

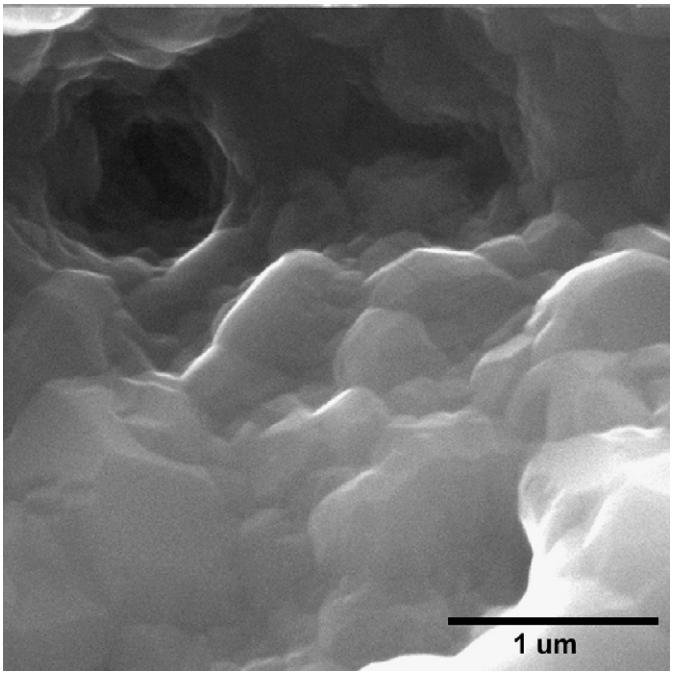


**Fig. 4.** Faceted walls of pore in sample annealed at 1100 °C for 6 h.

The activation energy for primary grain growth (where the grain size distribution remains monomodal, in this case at and below 1000 °C) was determined to be 0.80 eV using an Arrhenius analysis. This value is consistent with literature values of activation energies for grain growth in larger grained polycrystalline silicon [7,13].

Bulk polysilicon grown via conventional CVD methods reported in the literature does not exhibit the same type of as-deposited grains or grain growth found in the FBR granules [7,8]. Bulk polysilicon grown via the Siemens process begins as long acicular grains, which become equiaxed after annealing at temperatures above 1100 °C for 12–24 h. Abnormal grain growth has not been observed in bulk polysilicon grown via the Siemens process at these temperatures, whereas it appears to occur readily in the granules grown by in the FBR.

### 3.3. Hardness

Mechanical contact between granular material during handling may lead to fracture, and the fine grain size identified in this

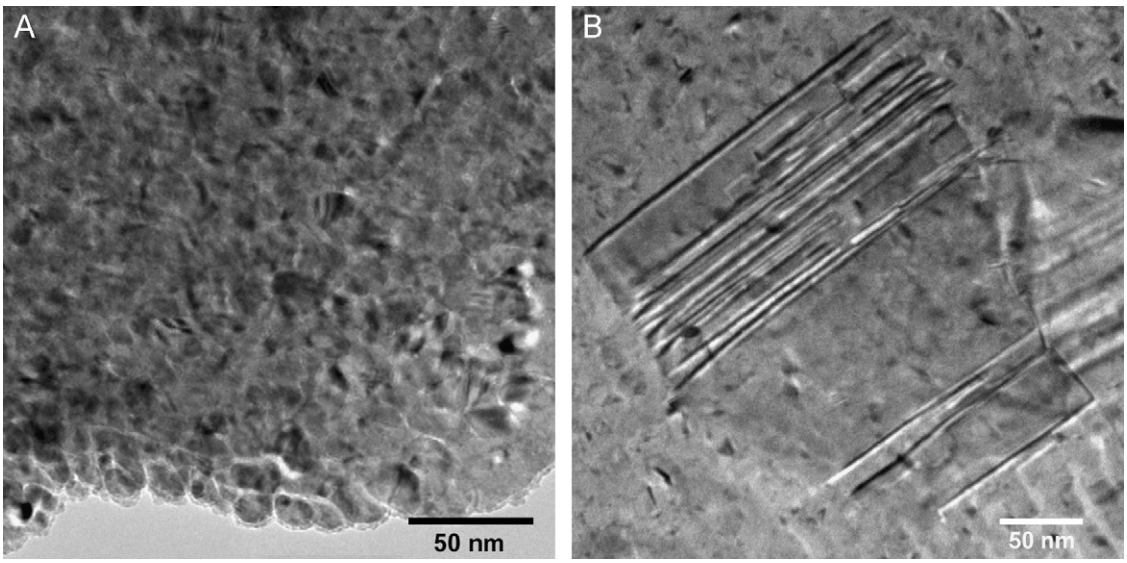


**Fig. 5.** TEM micrograph of (A) grains approximately 30 nm in diameter and (B) secondary grain growth present in annealed sample at 1100 °C.

**Table 2**
Silicon modulus and hardness values.

| | Elastic modulus (GPa) | Hardness (GPa) |
|---|---|---|
| Single crystal | 157.3 | $9.6 \pm 0.13$ |
| Granular material | 155.4 | $8.6 \pm 1.13$ |
| 1100 °C anneal | 157.7 | $8.7 \pm 0.94$ |

paper may lead to more compliant or softer materials in a manner similar to that of other nanocrystalline and ultrafine grained ceramic and semiconductor materials. To inspect the mechanical properties of silicon grown in the FBR independent of the density or morphology of pores the hardness was measured using nanoindentation, as opposed to larger scale Vickers microhardness testing, to ensure no fracture events occurred around the indentation. Due to the porous structure of the material, the hardness and elastic modulus are both a function of the contact depth; sampling larger volumes increases the likelihood of pores being present in the elastic stress field around the indentation, which could lead to lower hardness and modulus measurements [11]. Therefore, the hardness was measured at contact depths of approximately 100 nm, where the volume of material probed is large enough to be beyond tip rounding effects and is well within the range of the tip area function calibration, but small enough to be relatively insensitive to sub-surface porosity that may be present. In order to ensure no influence of porosity, the calculated hardness value for each of the silicon samples was based on a series of indentations with an average elastic modulus that was comparable to the modulus of a single crystal silicon sample; approximately 157 GPa.

The hardness for the granular material both the as-received and annealed states is shown in Table 2. Previously reported hardness values for bulk and thin film polysilicon are between 10 and 12 GPa [7,14]. In general the hardness of the FBR material is about 10% less than that of single crystal silicon, and annealing does not significantly impact the hardness of the material. This lower hardness is likely attributed to the fine grain structure, which may allow for some grain boundary sliding, a mechanism that would not be available in larger grained material. According to a Mann–Whitney–Wilcoxon statistical test [15], the sample data does originate from different populations.

## 4. Conclusions

Silicon granule material grown in FBRs consists of a macrostructure composed of semi-porous material, in which the closed pores are on the order of 5 μm in diameter, separated by segments of relatively pore-free material with thicknesses between 10 and 20 μm. The grain size of the as-grown material is on the order of 30 nm. On the walls of the pores there are spherical nodules with a nanotexture on the order of the grain size inferred by X-ray diffraction. Annealing below 1000 °C appears to follow similar kinetics for grain growth as other polysilicon materials. At an annealing temperature of 1100 °C the inner pore morphology ceases to be spherical and becomes faceted. Also, when the material is annealed at temperatures above 1100 °C, abnormal grain growth is observed for annealing times of 6 h. The as-grown granular material is slightly softer than conventionally grown polysilicon; this is most likely due to the very fine grain structure of the material.

## Acknowledgments

The experimental assistance of J.A. Reid and M.B. Zbib at Washington State University with nanoindentation experiments, and S. Letourneau at Boise State University with TEM observations are greatly appreciated.

## References

[1] V.A. Borodulya, L.M. Vinogradov, O.S. Rabinovich, A.V. Akulich, J. Eng. Phys. Thermophys. 78 (2005) 47.
[2] B. Caussat, M. Hemati, J.P. Couderc, Chem. Eng. Sci. 50 (1995) 3625.
[3] G. Coso, C. Canizo, A. Luque, J. Electrochem. Soc. 155 (2008) D485.
[4] S.K. Iya, R.N. Flagella, F.S. DiPaolo, J. Electrochem. Soc. 129 (1982) 1531.
[5] J. Pina, V. Bucala, N.S. Schbib, P. Ege, H.I. Lasa, Int. J. Chem. React. Eng. 4 (2006) 1.
[6] C.V. Thompson, J. Appl. Phys. 58 (1985) 763.
[7] R.W. Fancher, C.M. Watkins, M.G. Norton, D.F. Bahr, E.W. Osborne, J. Mater. Sci. 36 (2001) 5441.
[8] R.C. Brodie, D.F. Bahr, Mater. Sci. Eng. A 351 (2003) 166.
[9] G. Hsu, R. Hogle, N. Rohatgi, A. Morrison, J. Electrochem. Soc. 131 (1984) 660.
[10] G.K. Williams, W.H. Hall, Acta Mater. 1 (1953) 22.
[11] G.M. Pharr, W.C. Oliver, D.R. Clarke, Scripta Mater. 23 (1989) 1949.
[12] N.G. Nakhodkin, T.V. Rodionova, J. Cryst. Growth 171 (1997) 50.
[13] S. Kalainathan, R. Dhanasekaran, P. Ramasamy, Thin Solid Films 163 (1988) 383.
[14] B. Bhushan, X. Li, J. Mater. Res. 1 (1997) 54.
[15] H.B. Mann, D.R. Whitney, Ann. Math. Stat. 10 (1947) 50.